Characterization and development of high energy density Li-ion batteries

Harks, Peter-Paul

DOI
10.4233/uuid:cab44efd-8a4c-4b4d-8168-bd64738adb64

Publication date
2019

Document Version
Final published version

Citation (APA)
Harks, P.-P. (2019). *Characterization and development of high energy density Li-ion batteries*. [Dissertation (TU Delft), Delft University of Technology]. https://doi.org/10.4233/uuid:cab44efd-8a4c-4b4d-8168-bd64738adb64

Characterization and development of high energy density Li-ion batteries

Proefschrift

ter verkrijging van de graad van doctor
aan de Technische Universiteit Delft,
op gezag van de Rector Magnificus
Prof. dr. ir. T.H.J.J van der Hagen,
voorzitter van het College voor Promoties,
in het openbaar te verdedigen op
maandag, 14 oktober 2019 om 12:30 uur

door

Petrus Paulus Roelof Martina Leonardus HARKS

Master of Science in de natuurkunde
Universiteit Utrecht, Nederland
geboren te Leiderdorp, Nederland

Dit proefschrift is goedgekeurd door de promotor.

Samenstelling promotiecommissie bestaat uit:

Rector Magnificus	voorzitter
Prof. dr. F.M. Mulder	TU Delft, promotor
Onafhankelijke leden:	
Prof. dr. H. Geerlings	Technische Universiteit Delft
Prof. dr. S.J. Picken	Technische Universiteit Delft
Prof. dr. Ir. M. Huijben	Technische Universiteit Twente
Dr. E.M. Kelder	Technische Universiteit Delft
Dr. P. Ngene	Universiteit Utrecht
Overige leden:	
Prof. dr. Ir. M. Wagemaker	Technische Universiteit Delft

Keywords: lithium batteries, in situ techniques, immersion precipitation, neutron depth profiling

Printed by: Ipskamp printing

ISBN 978-94-028-1759-1

An electronic version of this dissertation is available at
http://repository.tudelft.nl/

Contents

1

Introduction

Introduction

The concerns about climate change and the mitigation measures to decrease greenhouse gas emissions, have brought about the need to implement renewable energies at a large scale. However, due to the intermittent nature of renewable sources, this can only be achieved with the ability to efficiently store energy. Among the various energy conversion/storage systems at hand, electrochemical storage and more specifically batteries are well-positioned to satisfy these needs, but research to meet the application needs is still urgently required. The crucial role of batteries in a society based on renewable energy further includes the global electric mobility, in which batteries determine the driving range of an electric vehicle. On top of these recent developments, batteries have become a critical component in mobile electronics e.g. mobile phones, laptops and drones, which itself is an ever - growing market. This stresses the importance of battery research and development.[1, 2]

Li-ion batteries

Batteries are electrochemical devices able to convert chemical energy into electrical energy and *vice versa*. A battery consists of a positive and a negative electrode, electrolyte and connectors/current collectors. Batteries operate via redox reactions taking place at the electrodes causing an internal flow of ions, and supplying an external flow of electrons (electric current). **Fig. 1.1** shows a schematic of a Li-ion battery. A conventional Li-ion battery consists of a lithium metal oxide or phosphate as a positive electrode, and a negative electrode consisting of graphite. The electrodes are physically separated by a porous polymer membrane which is soaked with electrolyte. The electrolyte, a lithium salt dissolved in an organic solvent, allows Li-ions to shuttle between the two electrodes but is a poor electrical conductor, and thus does not provide a pathway for electrons. The current collectors are metal foils that facilitate the electron transport and do not store Li themselves.

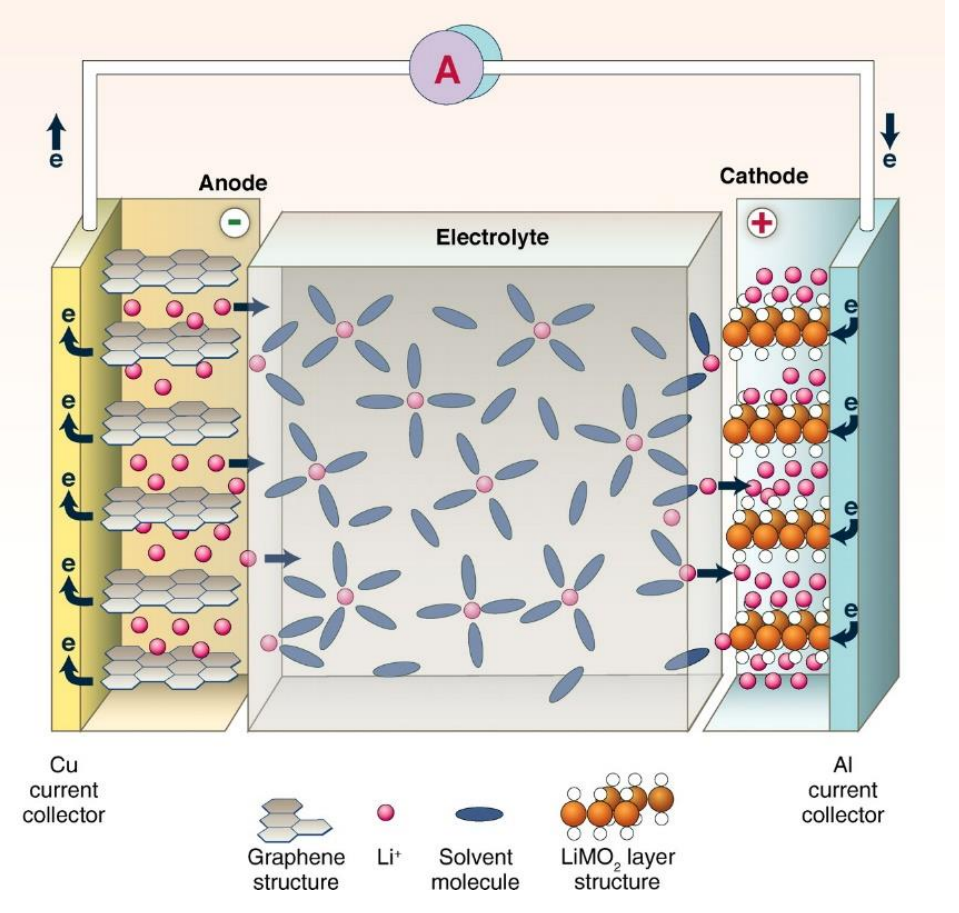

Figure 1.1 Schematic of a Li-ion battery. The negative electrode is a graphitic carbon that stores Li between its layers, whereas the positive electrode is a lithium transition metal oxide with a layered structure. Both electrodes are able to reversibly insert and remove Li-ions from their respective structures. On discharge, Li-ions are extracted or deintercalated from the graphite and intercalated into the layered oxide compound. The process is reversed on charge. The electrodes are separated by a nonaqueous electrolyte that transports Li-ions between the electrodes. Reprinted from ref. [2], with permission from AAAS.

Theoretical considerations

The driving force enabling discharge is the chemical potential difference between the negative and positive electrode, or equivalently in electrochemical equilibrium their electron fermi level difference. When a battery is fully charged, all Li is stored in the negative electrode at a high chemical potential state relative to the positive electrode. Therefore the Li-ions diffusing from the negative electrode can react at the positive electrode, thereby lowering the systems' energy. However, due to the

presence of electrolyte between the electrodes, only Li-ions are able to travel through while electrons are blocked. By connecting the current collectors of the two sides externally, electrons are now able to follow the Li-ion motion and travel to the positive side, delivering power. Whenever the battery circuit is shorted, this process occurs spontaneous (discharge). This situation is depicted in **Fig. 1.1**, where the negative electrode donates electrons (anode) and the positive electrode accept electrons (cathode). In open circuit and in equilibrium the electric field between positive and negative electrode just compensates the difference in chemical potential and the electrochemical potential is zero. During discharge the reduced electrical potential makes that more Li ions can flow from anode to cathode. During charge, energy is required to force Li-ions back to the energetically less favorable side. Therefore a potential is applied to drive the Li ions from the positive electrode to the negative. In literature the negative and positive electrode are generally referred to as the anode and cathode, respectively, although the opposite will be true during charging the battery,.

Cell potential

When the electronic circuit is open, no current can flow and therefore there cannot be a net force acting on the mobile charged species in the electrolyte. The chemical driving force upon the ionic species that arises from the difference in chemical potential of the electrodes in the cell is balanced by an electrostatic force in the opposite direction. This can be expressed as an energy balance the difference of Gibbs free energy (expressed per mole) associated with the overall reaction in the cell, ΔG, and the electrostatic energy of a mole of electrically charged species, $-zFE$. Here z is the charge number (1 for Li^+), F the faraday constant, i.e. the charge of a mole of species with the elemental charge, and E the cell voltage. The expression for the cell voltage therefore is:[3]

$$E = -\Delta G/zF$$

Although the (open circuit) voltage can be derived from these theoretical considerations, during actual battery operation non-equilibrium conditions apply. Different kinetic mechanisms can limit battery performance and influence the (working) voltage. These processes are associated with e.g. the electronic conductivity, ionic transport through the electrolyte, the charge transfer reaction over the electrolyte/electrode interface, and the solid-state transport process (Li-ion diffusion in the electrode particle). Which of the mechanisms is rate limiting depends on the applied current as well as on morphological properties of the electrodes such as electrode porosity, tortuosity and (particle) size etc.[4]

Improving battery performance

Battery performance is often quantified by the power and energy density and cycle life. Other important parameters include safety, environmental friendliness and cost. Which of these properties is of primary importance depends on the application. For example mobile applications prioritize very light and energy dense batteries (energy density). Energy density quantifies the amount of energy stored per unit of weight (gravimetric), volume (volumetric), or costs. Power density, on the other hand, quantifies how fast this energy can be available and is measured in energy per time (power), per weight unit. It should, however, be noted that in scientific literature often the less practical specific capacity is reported, which gives the amount of charge stored per unit of weight of active material.

Lithium-ion batteries were first commercialized in 1990. The first generation had more than double the energy density of nickel or lead batteries (Li-ion battery predecessors). However, both existing and emerging applications, as discussed in the previous paragraph, demand even better performance metrics in terms of energy/power density, price, safety and environmental impact. As a consequence, though the technology is mature, the pursuit for improved performance has never been so urgent. Over nearly three decades since the deployment of the Li-ion battery, it has witnessed continuous progress in design and electrode materials (alternatives to $LiCoO_2$, such as $LiNiCoMnO_2$), resulting in incremental improvements in performance. Nonetheless, these intercalation materials have intrinsic limitations in terms of capacity, which means that significant further improvement can only be achieved by the development of new electrode materials, or radical changes in electrode design.[1]

Recently several Li battery concepts beyond the current graphite - metal oxides chemistries have received much research attention. For instance, the lithium sulfur battery employs a metallic Li negative electrode, and the low cost and abundant sulfur as positive electrode material. Furthermore the system is interesting from the high energy density point of view, however, it comes with many challenges (materials related) which need to be addressed (Chapter 2).[1, 5]

Another route toward improved energy density focusses on the electrode fabrication and design. Although this approach does not receive even a fraction of the attention given to material research, it is a viable and important route for improvement. This material independent route involves finding new methods for creating thick and mechanical stable electrode layers so that the energy density on cell level is improved by achieving a higher ratio of active over inactive material in a battery.[6]

Outline and goals of this thesis

This thesis revolves around the characterization, understanding and development of high energy density Li-ion batteries. This is done by investigating a possible successor of current Li-ion technology, the Li-S battery, and through the development of a method for electrode fabrication to achieve higher energy density on the cell level.

The goal in chapter 2 is to elucidate the working principle behind the Li-S battery, particularly regarding the extremely poor electronic conductivity of sulfur. Lithiation of an electrode traditionally requires both Li-ions and electrons to diffuse into the material and therefore moderate to good ionic and electronic conductivity is considered a prerequisite for active materials. This requirement in this case is not met, which seems to conflict with the high level of performance of Li-S batteries.

The next two chapters cover the characterization of Li-ion batteries in general, and the Li-S battery in particular. In chapter 3 an overview of the various in situ characterization methods available to study Li-ion batteries is provided, along with the recent developments in this field. In situ methods are critical in the field of battery research as they allow measurements on fully assembled cells. However, this often means that standard lab/commercial cells require modifications to become compatible with the technique. These modification are reviewed, and the relevance that the data obtained from specially designed cells have for conventional batteries is critically discussed.

In chapter 4 an advanced method for battery diagnosis, neutron depth profiling, was applied to perform operando measurements on Li-S batteries. This technique was selected as it is able to probe lithium in the working electrode as well as (part of) the electrolyte in a cell. This is a unique feature and especially relevant to Li-S cells because of their 'liquid' character, i.e. many electrochemical processes during operation are thought to take place in the electrolyte. Investigating the processes at different length scales starting from battery current collector, active layer to electrolyte interface has never been possible to date, which impedes further progress in Li-S batteries. In this chapter the NDP technique was brought forward to do this and was applied to visualize and validate the working principle of a novel strategy based on a chemical adsorption route which has been recently discovered as an effective way to enhance Li-S cell performance.

The last part of this thesis (chapter 5) covers the development of high energy density batteries from a device-level approach. The goal is to fabricate electrodes with high storage capacity per electrode surface area that are mechanically robust, with high ionic and electronic conduction throughout the electrodes, resulting in high performing electrodes. This allows the electrode thickness in batteries to be increased, which reduces the amount of inactive

material in the cell, thus improving the energy density. A method based on mature technology from the membrane industry is presented for electrode fabrication, and the origins of the enhanced mechanical integrity and performance of the obtained electrodes were investigated.

References

1. J. Cabana, L. Monconduit, D. Larcher and M. R. Palacin, *Advanced Materials*, 2010, **22**, E170-E192.
2. B. Dunn, H. Kamath and J. M. Tarascon, *Science*, 2011, **334**, 928-935.
3. R. Huggins, *Advanced Batteries: Materials Science Aspects*, Springer US, 2008.
4. C. F. Liu, Z. G. Neale and G. Z. Cao, *Materials Today*, 2016, **19**, 109-123.
5. M. M. Thackeray, C. Wolverton and E. D. Isaacs, *Energy & Environmental Science*, 2012, **5**, 7854-7863.
6. K. G. Gallagher, S. E. Trask, C. Bauer, T. Woehrle, S. F. Lux, M. Tschech, P. Lamp, B. J. Polzin, S. Ha, B. Long, Q. Wu, W. Lu, D. W. Dees and A. N. Jansen, *Journal of the Electrochemical Society*, 2016, **163**, A138-A149.

2

The Significance of Elemental Sulfur Dissolution in Liquid Electrolyte Lithium Sulfur Batteries

This chapter has been published as PPRML Harks, CB Robledo, TW Verhallen, PHL Notten, FM Mulder, Advanced Energy Materials 7 (3), 1601635 (2017)

There is a growing demand for high energy density batteries due to the increasing use of portable electronics, the necessity to cope with the fluctuating output of renewable energy sources, and to power electric vehicles.[1] As Li-ion batteries approach the limit of their performance, much attention is focused on battery systems beyond current Li-ion insertion technology. Among the next-generation battery systems, many consider lithium-sulfur (Li-S) batteries closest to succeeding Li-ion technology.[2] Due to sulfur's high theoretical uptake capacity of lithium and its abundancy, Li-S batteries offer the potential of higher energy densities and lower cost. However, the system is still hampered by issues that are mainly ascribed to the high solubility of the intermediate lithium polysulfide species, to side-reactions at the lithium anode, and to the low conductivity of both S and Li_2S.[3] To tackle the problems associated with Li-S batteries it is key to have a profound understanding of the underlying mechanisms during battery operation. The (de)lithiation process in a Li-S battery involves a complicated series of electrochemical steps, and also includes (purely chemical) polysulfide disproportionation reactions and the presence of radicals.[4]

Although much is known about the general reactions taking place during battery operation, many questions still exist regarding the processes at the microscopic particle level. Those questions are especially related to the initial step, which is the reduction of electronically insulating sulfur into (soluble) polysulfides (PS). The electrical conductivity of sulfur is about $5*10^{-18}$ S cm^{-1} [5] (this is unlike the often reported 10^{-30} S cm^{-1}, but still highly insulating. See supporting information). The intrinsically non-conducting property of sulfur for both Li-ions and electrons is often presented as a major drawback for its use in a battery, which implies that the initial reduction of sulfur into PS is primarily considered a solid-state reaction. This is consistent with the general approach for making sulfur cathodes, which has been to reduce the size of the sulfur structures (at least in one dimension) and to create intimate contact with a porous conductive host, often carbon, to increase both the electronic and ionic conductivity of the electrode.[6] However it has been shown that Li-S batteries based on micron-sized sulfur particles, or on non-mixed C/S electrodes, can be readily cycled.[7] Actually several studies have shown that the particle morphology of sulfur and the mixing degree of carbon and sulfur has little influence on the electrochemical performance of the electrodes.[8] This seems to be in fundamental conflict with the extremely insulating nature of sulfur, as it would hinder diffusion of both electrons and ions over the associated relatively long distances, and therefore should be reflected in the battery performance.

Apart from the large resistance associated with solid-state reduction, another effect seems to impede this process. It can be reasoned that the lithiation will commence at the interface of sulfur, carbon, and the electrolyte, as the diffusion

paths for the charged species through the sulfur itself are virtually zero. However, it is generally accepted that the reaction products are highly soluble in organic solvents, and therefore the result will be that the contact points of the (big) sulfur particles with the carbon matrix will effectively dissolve during this process (**Fig. 2.1**). This would be detrimental to the required electronic connection in the electrode, and makes further solid-state reduction of sulfur hardly imaginable. To the authors' best knowledge, this phenomenon or the possible ways in which the sulfur particles and carbon host remain in proper contact despite this effect, are not addressed in literature.

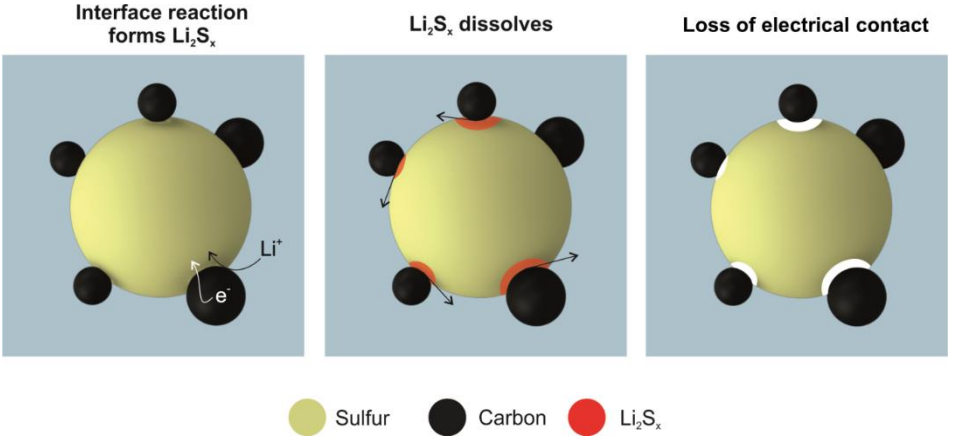

Figure 2.1. Schematic representation of a sulfur particle as part of a composite electrode (binder and electrolyte not shown) during the early stage of lithiation, with the supposed deterioration of the contact of the particle with the conducting matrix.

Given the aforementioned considerations, it seems justified to speculate that simple dissolution of elemental sulfur ($S_8^0{}_{(sol)}$) plays a fundamental role in the lithiation process in Li-S batteries. Surprisingly, the dissolution of sulfur into the electrolyte is only rarely considered as a relevant phenomenon in the cycling of Li-S batteries. Although several modeling papers hypothesize the dissolution of sulfur as the initial step in the lithiation process,[9] most of the recent review articles on Li-S batteries do not explicitly mention the dissolution of sulfur with regards to the cycling mechanism.[3, 10] Only Xu et al.[11] stated that dissolved sulfur facilitates the reduction process to some degree. The limited consideration given to this process in literature is probably because it is generally known that sulfur only poorly dissolves in organic solvents and therefore it is neglected. However, a low solubility does not automatically mean a low dissolution rate, which leaves the possibility that the dissolution rate is high enough to keep up with the electrochemical reactions, at least to some degree.

In this study several unconventional Li-S battery configurations are used to investigate whether sulfur dissolution can play an important role in the operation of liquid electrolyte Li-S cells. We furthermore speculate on other processes that enable the relative efficient use of sulfur in Li-S batteries, despite of its non-conductive characteristics. The electrochemical cells featured in this study intend to illustrate and elucidate specific Li-S battery mechanistic concepts.

Remarkably, little information is available on the solubility of sulfur in organic solvents, especially in the context of Li-S batteries. It is known that the solubility of S_8 in typical electrolyte solvents is in the millimolar range, and the presence of lithium salts generally lowers the solubility.[12] The relevant data from literature are listed in **Table 2.1**. As there is no specific data available, we started with measuring the solubility of sulfur in the most commonly used electrolyte for Li-S batteries. At room temperature 0.13 wt.% S (~5mM S_8) could be dissolved in a 1:1 vol.% mixture of 1,3-dioxolane (DOL)/1,2-dimethoxyethane (DME) containing 1M lithium bis(trifluoromethane)sulfonimide (LiTFSI) and 2 wt.% $LiNO_3$ additive. Although this is indeed a relatively low solubility, it should be realized that it still can cause a significant fraction of the active sulfur mass to dissolve into the electrolyte in a laboratory scale Li-S cell, depending on the ratio between the amount of electrolyte and the active material. For instance, in a cell that contains 40 µL electrolyte and a mass loading of 1 mg sulfur, approximately 5 wt.% of the total active material will be able to dissolve before the electrolyte is saturated.

Table 2.1. Experimental solubility limit of sulfur in organic solvents/electrolytes at room temperature

Solvent	S_8 solubility (wt.%)	S_8 solubility (mM)	Ref.
TEGDME	0.19	~7.5[a)]	[12a]
DME		9.957	[12b]
DME, 1M LiTFSI		3.994	[12b]
DOL/DME 1:1 v/v, 1M LiTFSI, 2wt.% $LiNO_3$	0.13	~5[a)]	This work

[a)]estimated solubility based on the reported value in wt.% and the density of the solvent

To investigate the role of sulfur dissolution under realistic conditions but at the same time excluding solid-state reduction (in the first cycle), a special configuration was used. In this battery sulfur powder was electrically insulated from the conducting carbon current collector by the application of an additional separator, placed between the sulfur powder and the current collector (see **Fig. 2.2a**). Both separators were wetted with electrolyte. Indeed it was found that such cells can be cycled. Obviously, as there is no electrical connection between the sulfur and the

current collector, the sulfur must have dissolved into the electrolyte and diffused through the (25μm thick) separator to the current collector where it can react. **Fig. 2.2b** shows the voltage output during the first lithiation for different current rates. An apparent voltage dip at the beginning of discharge can be observed, which becomes larger with increasing C-rate. Batteries tested at a rate of C/10 and higher, rapidly reached the lower cut off voltage and therefore couldn't be cycled (not shown). It was decided to keep the 1.8V cut off in place to rule out any reduction of the $LiNO_3$ additive.[13] Based on the 'normal' voltage output during the subsequent discharge cycles, without voltage dip (**Fig. 2.2c**), sulfur has formed on the carbon current collector after the first charge. This statement is further supported by the observation that no sulfur residue was present between the separators in charged cells that were opened after long term cycling. Remarkably, despite this large displacement of sulfur across the separator in the first cycle(s), the batteries typically become stable and show significant capacities. For instance, a cell cycled at C/20 reaches a capacity of 500 mAh g^{-1}, with a very high coulombic efficiency (**Fig. 2.2d**) although starting from a configuration with completely electronically insulated S.

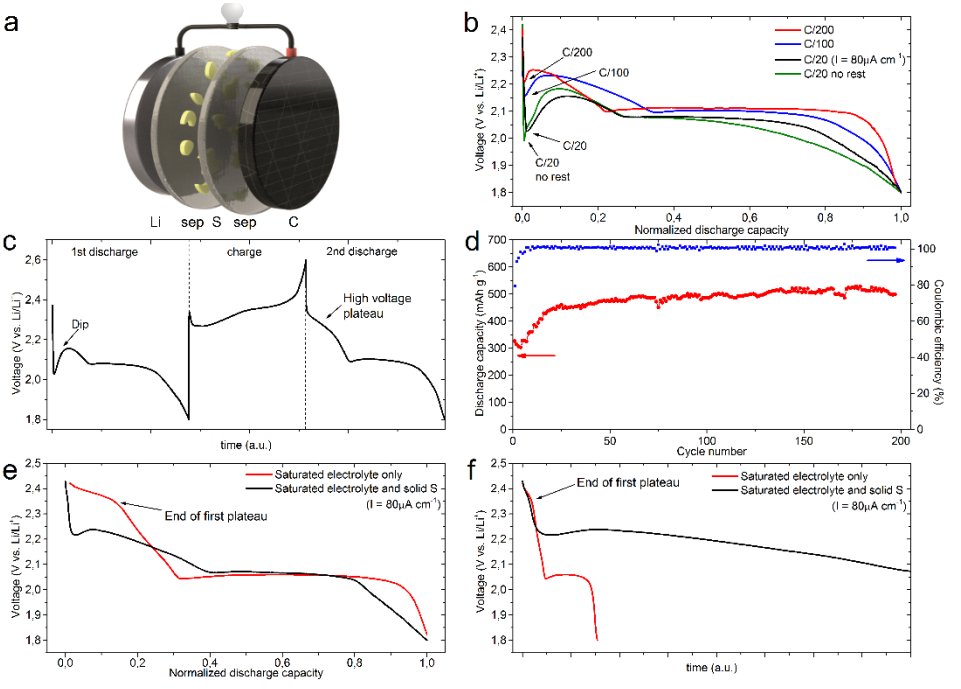

Figure 2.2. a) Schematic presentation of the tested cell. b) Voltage response during the first lithiation as a function of normalized capacity for different C-rates, the arrow indicate the lowest point of the voltage dip. c) First 1.5 cycle of a cell cycled at C/20. d) Discharge capacity and coulombic efficiency as a function of cycle number tested at C/20. e,f) First discharge of cells containing electrolyte which is saturated with sulfur. The red and black line correspond to a battery with no additional solid sulfur, and with additional solid sulfur between the separators, respectively. The voltage is plotted e) as a function of normalized discharge capacity, and f) as a function of time. Both cells were discharged with the same absolute current. The arrows indicate the same point during the measurement.

To investigate whether the aberrant output voltage during the first lithiation is a fundamental effect of S_8 reacting as a dissolved species, or has to do with the deviant location of solid sulfur in the battery, a battery based solely on dissolved sulfur was tested. The voltage characteristic of that cell, of which the electrolyte was pre-saturated with elemental sulfur while no solid sulfur was present in the cell, is shown in **Fig. 2.2e** and **2.2f** (red line). The voltage output is consistent with the voltage profile of a conventional Li-S battery, and shows a plateau around 2.4V which corresponds to the reduction of S_8 into high order PS (Li_2S_x, $x \geq 4$).[11] Electrolyte saturated with sulfur was also applied to a cell with solid sulfur present between the separators and not connected to the C current collector. Both batteries were discharged with the same absolute current and current density, and can therefore be plotted together as a function of time (**Fig. 2.2f**). It can be observed

that their voltage output overlaps in the first minutes. Interestingly, for the cell with solid sulfur available, the replenishment of S_8 species into the electrolyte is not high enough to maintain the high voltage plateau longer than the cells with only S saturated electrolyte (indicated by an arrow). However, contrary to the cell solely based on saturated electrolyte the discharge is continued at ~2.2V, utilizing, directly or indirectly, the sulfur that is located between the separators.

When we compare the first cycle's dip position of this cell to the cells tested earlier based on non-saturated electrolyte, it can be concluded that the sulfur concentration in the electrolyte in those cells was lower than saturation level. Actually both the non-rested and rested cell show their minimum voltage around 2V (**Fig. 2.2b**). On the one hand this means that sulfur immediately dissolves as soon as the battery is assembled, and thus that a significant amount S_8 is always present in the electrolyte of Li-S batteries. However, on the other hand, it can be concluded that the subsequent rise in concentration of dissolved sulfur to its saturation level is relatively slow.

The difference in voltage response in the first cycle of the special cells in this study compared to conventional Li-S batteries does not prove that solid-state reactions in conventional cells therefore must be dominant, to the contrary. The replenishment of dissolved sulfur species is a function of both the dissolution rate into, and diffusion speed through, the electrolyte. The degree to which the sulfur species in solution are replenished should therefore be related to the rate at which the dissolved sulfur is consumed (i.e. current rate) at the current collector, and the distance between the solid sulfur and the current collector (i.e. diffusion path length). A lower current rate as well as a smaller diffusion path length for the dissolved S species should thus result in a higher degree of replenishment. The former is indeed observed in our current-dependent experiments (**Fig. 2.2b**), where lower current rates resulted in smaller voltage drops. The latter is consistent with the fact that in a conventional Li-S battery the separation of the sulfur source and the reaction site is orders of magnitude smaller than in our test batteries. The difference is schematically illustrated in **Fig. 2.3**: step 1: establishing equilibrium between solid S and dissolved molecular S_8 in the electrolyte, step 2: diffusion of dissolved S_8 to reduction site at current collector, step 3: reduction to a highly soluble polysulfide. It is therefore very plausible that dissolution of elemental sulfur plays a significant role in the overall working mechanism of liquid electrolyte Li-S cells. Which reaction mechanism (reduction of dissolved or solid sulfur) will dominate is determined by their associated kinetics. Due to the low conductivity of sulfur, poor kinetics can be expected for solid state reduction, however reactions over small (nanoscale) lengths cannot be fully excluded. This is evident from nanoparticle based solid Li-S cells, for which considerable capacities can be

achieved when cycled at moderate current rates.[14] As a side note we want to remark that the obtained capacities for these systems should be regarded with some reserve since the applied sulfide solid electrolytes are only stable in a small voltage window and can contribute to the capacity.[15] We think that lithiation of dissolved sulfur undoubtedly is the dominant phenomenon in Li-S cells based on relatively large sulfur particles, as solid-state reactions in this case would give rise to large overpotentials and effectively the dissolution of the electrical contacts in the electrode, as described in the introduction.

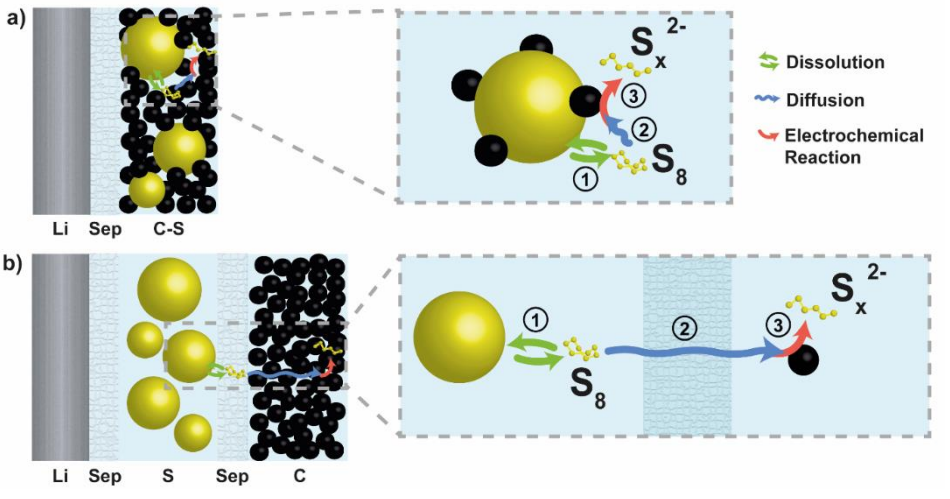

Figure 2.3. Schematic representation of the dissolution of sulfur in the electrolyte and its subsequent diffusion to, and reduction at, the carbon current collector, in a) a conventional Li-S battery with a mixed C/S electrode and in b) the battery designed for this research.

Although the voltage dips that are present at the beginning of the first discharge are very specific to the special battery configuration applied in this study, their origin can still reveal processes that facilitate the relative efficient consumption of non-conducting sulfur in conventional Li-S batteries. Even though further study of this behavior is not in the scope of this communication, we can speculate on the reason(s) behind the voltage drop and subsequent rise. As soon as current is drawn from the battery, the dissolved sulfur species are consumed. This will lead to a drop in concentration of S_8 species in solution, which in turn causes a bigger driving force for dissolution of sulfur into the electrolyte at the source between the separators. However, due to the finite dissolution rate and diffusion speed, and the 25 micrometer minimal diffusion distance (thickness of the separator), it will take time before a dynamic equilibrium of the S_8 concentration is formed. To maintain the current during this delay, the PS will be further reduced, which temporarily

corresponds to lower voltages. The higher the currents, the bigger these effect will be, leading to complete depletion of reducible species in the vicinity of the carbon current collector for current rates of C/10 and higher. However, it may also be that interaction between PS and the sulfur between the separators should be taken into account. For instance, during the drop in voltage in the initial moments of the discharge highly soluble PS, including Li_2S_x ($x < 8$), are formed. These lower order ($x < 8$) PS can react chemically with the solid S to Li_2S_8, increasing the level of Li_2S_8 species in solution, which results in a rise of cell potential. In this shuttle mechanism sulfur is transported to the current collector through its chemical conversion by a low order PS into a high order PS which is soluble, while pure S is much less soluble. This mechanism is plausible as the standard approach to make lithium PS is to let S and Li_2S react in solution. Even though generally this is done at an elevated temperature to speed up the process, these reactions occur spontaneously at room temperature.[16] Such reactions, between unreacted solid sulfur and already formed lower order PS, can therefore be expected in a Li-S battery. The higher order PS that are created can in turn further participate in electrochemical reactions in solution. If so, the (low order) PS, and possibly radicals,[17] that are formed during cycling effectively fulfil the role of natural redox mediators in this system.

This study clearly shows that the dissolution of elemental sulfur and the subsequent reduction of the dissolved S_8 species cannot be ignored in liquid electrolyte Li-S cells. The process allows even batteries of which the active material is not in electrical contact with the current collector to be discharged. It indicates that, despite the low solubility of S_8 in organic solvents, the replenishment of sulfur species in solution is fast enough to enable the electrochemical reactions at the (carbon) current collector. The obtained results provide a rationale why Li-S batteries in general, and cells based on macroscopic S particles in particular, can be efficiently cycled, despite the extremely insulating nature of S. Chemical reactions between PS and sulfur may further enable the utilization of active material. Identifying the key processes and chemical reactions in Li-S batteries is essential for their further optimization. This study experimentally shows the significance of elemental sulfur dissolution into the electrolyte in liquid Li-S cells.

Experimental Section

Solubility measurements: To determine the solubility of sulfur in the electrolyte at room temperature (25°C), 0.5 mg sulfur powder (sulfur flakes, Sigma Aldrich) was added to 2.5 ml electrolyte and rigorously stirred for 2 hours. When no sulfur residue was observed this procedure was repeated. The weight of the residue was determined and subtracted from the total amount of added sulfur powder during

the procedure to calculate the solubility. The obtained solubility was electrochemically verified, see supporting information.

Electrochemical measurements: The employed electrochemical cells were lab-made prototypes consisting of two stainless steel vacuum flanges, with one acting as current collector and the opposite having a separate current collector held by a spring to provide mechanical pressure and compaction, a standard O-ring in between the flanges, and a plastic vacuum clamp that holds the stainless steel flanges together. The tested cells were fabricated by placing a Li-foil on the stainless steel current collector, followed by a separator. The separator was wetted with 25 µL electrolyte, after which sulfur powder was manually distributed on it. Subsequently another separator was placed on top of the layer of sulfur particles and also wetted with 25 µL electrolyte, followed by a C-membrane. The mass loading of S was 1 mg cm^{-2}. The applied separators were 25 µm thick Celgard® 3401 membranes, and the applied electrolyte in this study was 1M LiTFSI in DME/DOL 1:1 v/v with 2 wt.% $LiNO_3$ additive. The carbon membranes were prepared by the inversion method, see supporting information. **Fig. S2.1**, in the supporting information shows photos of the set-up. The cells were assembled inside an Ar filled glovebox with oxygen and water content less than 1 ppm. The galvanostatic cycling experiments were performed with a programmable Maccor 4000 series galvanostat. Before cycling all cells were rested for 12h to enable full wetting of electrolyte throughout the cell, unless otherwise stated. The cells were discharged to 1.8 V and charged to 2.6 V vs. Li/Li^+ at various C-rates (1C = 1675 mA g^{-1}). In this report discharging and charging the Li-S batteries corresponds to lithiation and delithiation of the sulfur, respectively. The specific capacities reported in this study are based on the mass of sulfur in the cell.

References

[1] a) F. M. Mulder, *J. Renewable Sustainable Energy* **2014**, *6*, 033105; b) F. Cheng, J. Liang, Z. Tao, J. Chen, *Adv. Mater.* **2011**, *23*, 1695.

[2] R. Van Noorden, *Nature* **2014**, *507*, 26.

[3] Y.-X. Yin, S. Xin, Y.-G. Guo, L.-J. Wan, *Angew. Chem. Int. Ed.* **2013**, *52*, 13186.

[4] M. Wild, L. O'Neill, T. Zhang, R. Purkayastha, G. Minton, M. Marinescu, G. J. Offer, *Energy Environ. Sci.* **2015**, *8*, 3477.

[5] J. A. Dean, N. A. Lange, *Lange's handbook of chemistry*, McGraw-Hill, New York **1985**.

[6] Z. Li, Y. Huang, L. Yuan, Z. Hao, Y. Huang, *Carbon* **2015**, *92*, 41.

[7] a) S. S. Zhang, D. T. Tran, *J. Power Sources* **2012**, *211*, 169; b) C. Barchasz, J.-C. Lepretre, F. Alloin, S. Patoux, *J. Power Sources* **2012**, *199*, 322; c) L. Qie, A. Manthiram, *ACS Energy Lett.* **2016**, *1*, 46.

[8] a) S. Urbonaite, T. Poux, P. Novak, *Adv. Energy Mater.* **2015**, *5*, 1500118; b) S. S. Zhang, *Electrochem. Commun.* **2013**, *31*, 10; c) S. Urbonaite, P. Novak, *J. Power Sources* **2014**, *249*, 497.

[9] a) K. Kumaresan, Y. Mikhaylik, R. E. White, *J. Electrochem. Soc.* **2008**, *155*, A576; b) M. Marinescu, T. Zhang, G. J. Offer, *Phys. Chem. Chem. Phys.* **2016**, *18*, 584; c) A. F. Hofmann, D. N. Fronczek, W. G. Bessler, *J. Power Sources* **2014**, *259*, 300; d) T. Danner, G. Zhu, A. F. Hofmann, A. Latz, *Electrochim. Acta* **2015**, *184*, 124.

[10] a) A. Manthiram, Y. Fu, S.-H. Chung, C. Zu, Y.-S. Su, *Chem. Rev.* **2014**, *114*, 11751; b) A. Rosenman, E. Markevich, G. Salitra, D. Aurbach, A. Garsuch, F. F. Chesneau, *Adv. Energy Mater.* **2015**, *5*, 1500212; c) S. S. Zhang, *J. Power Sources* **2013**, *231*, 153.

[11] R. Xu, J. Lu, K. Amine, *Adv. Energy Mater.* **2015**, *5*, 1500408.

[12] a) S. F. Sciamanna, S. Lynn, *Ind. Eng. Chem. Res.* **1988**, *27*, 485; b) D. Zheng, X. Zhang, C. Li, M. E. McKinnon, R. G. Sadok, D. Qu, X. Yu, H.-S. Lee, X.-Q. Yang, D. Qu, *J. Electrochem. Soc.* **2015**, *162*, A203.

[13] D. Aurbach, E. Pollak, R. Elazari, G. Salitra, C. S. Kelley, J. Affinito, *J. Electrochem. Soc.* **2009**, *156*, A694.

[14] a) T. Yamada, S. Ito, R. Omoda, T. Watanabe, Y. Aihara, M. Agostini, U. Ulissi, J. Hassoun, B. Scrosati, *J. Electrochem. Soc.* **2015**, *162*, A646; b) M. Chen, S. Adams, *J. Solid State Electrochem.* **2015**, *19*, 697; c) F. Han, J. Yue, X. Fan, T. Gao, C. Luo, Z. Ma, L. Suo, C. Wang, *Nano Lett.* **2016**, *16*, 4521.

[15] F. Han, T. Gao, Y. Zhu, K. J. Gaskell, C. Wang, *Adv. Mater.* **2015**, *27*, 3473; F. Han, Y. Zhu, X. He, Y. Mo, C. Wang, *Adv. Energy Mater.* **2016**, *6*, 1501590.

[16] a) Y. Yang, G. Zheng, Y. Cui, *Energy Environ. Sci.* **2013**, *6*, 1552; b) D. Zheng, X. Zhang, J. Wang, D. Qu, X. Yang, D. Qu, *J. Power Sources* **2016**, *301*, 312.

[17] M. Cuisinier, C. Hart, M. Balasubramanian, A. Garsuch, L. F. Nazar, *Adv. Energy Mater.* **2015**, *5*, 1401801.

Chapter 2. Supporting Information

Sulfur conductivity

The reference, when given, for the electrical conductivity of sulfur is mostly: Lange's handbook of chemistry, J.A. Dean (3rd ed.) McGraw-Hill, New York (1985) pp. 3–5. The reported electrical resistivity of sulfur in this book[1], and other textbooks (e.g. Ref [2]), is $\rho = 2 \cdot 10^{23}\ \mu\Omega \cdot cm$. When we convert this to conductivity we obtain

$$\sigma = \frac{1}{\rho} = \frac{1}{2 \cdot 10^{23}\mu\Omega \cdot cm} = \frac{1}{2 \cdot 10^{17}\Omega \cdot cm} = 5 \cdot 10^{-18}\ S \cdot cm^{-1}$$

Furthermore

$$\sigma = \frac{1}{\rho} = \frac{1}{2 \cdot 10^{23}\mu\Omega \cdot cm} \neq 5 \cdot 10^{-24}\ \mu S \cdot cm^{-1} = 5 \cdot 10^{-30}\ S \cdot cm^{-1}$$

The latter, $5 \cdot 10^{-30}\ S \cdot cm^{-1}$, is the generally accepted, but erroneous, value for the conductivity of sulfur in battery literature.

Battery set up

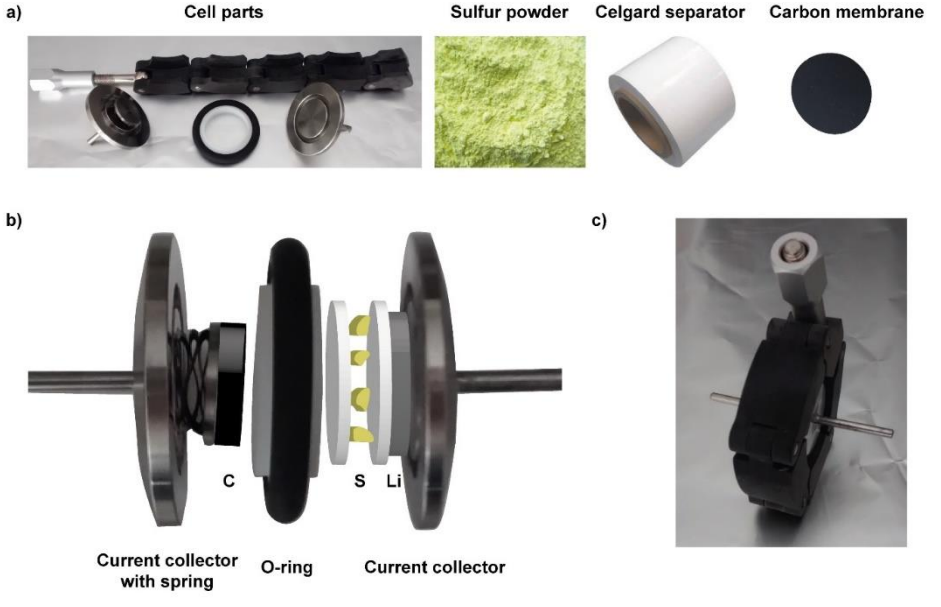

Figure S2.1. Electrochemical cell used in this study. a) All the components, b) open cell with the components in place and c) closed cell.

Carbon membranes

Carbon membranes were prepared by the inversion method[3]. In the first step, PVDF (Kynar Flex) was dissolved in N-methyl-2-pyrrolidone (NMP, Sigma Aldrich) by magnetic stirring to obtain a homogeneous 10 wt.% PVDF/NMP solution. Subsequently, 50 wt.% (based on the PVDF mass) of Super P carbon (Timcal) was added to the mixture and stirred overnight. Then the solution was casted onto a flat glass plate and immersed in distilled water. After a couple of minutes the membrane peeled off automatically from the glass plate. Afterwards it was washed with distilled water and dried under vacuum at 60°C overnight.

Electrochemical verification of S solubility limit

To verify the solubility of sulfur in the electrolyte electrochemically, a Li-S battery was created containing a Li anode, two Celgard® 3401 separators and a carbon membrane as cathode current collector. The applied electrolyte was saturated with sulfur, and served as the only active material source. **Fig. S2.2** shows the first discharge of such a battery, which was used immediately after fabrication (no rest). Approximately half of the theoretical capacity based on the amount of dissolved sulfur (known from the solubility experiments) was obtained. This discrepancy is easily accounted for as part of the sulfur will have reacted with the Li anode. Furthermore the theoretical capacity is seldom obtained in practical batteries and therefore part of the difference results from a general effect, rather than a phenomenon specific to this system. The test therefore shows that the solubility reported in the paper can at most be overestimated by a factor 2, in the unlikely case that only electrochemical reduction at the cathode takes place and no chemical reduction at the Li anode.

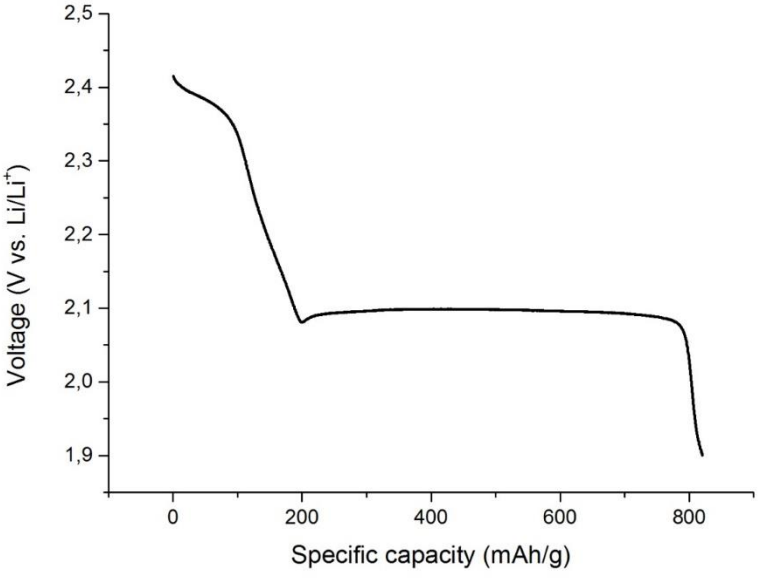

Figure S2.2. First discharge of a Li-S battery based on electrolyte saturated with elemental sulfur, which is the only source of active material.

References

[1] J.A. Dean, N.A. Lange, Lange's handbook of chemistry, 13th ed., McGraw-Hill, New York, 1985.
[2] R.C. Weast, M.J. Astle, CRC handbook of chemistry and physics : a ready-reference book of chemical and physical data, 60th ed., CRC Press, Boca Raton, 1979.
[3] F. Liu, N.A. Hashim, Y. Liu, M.R.M. Abed, K. Li, Journal of Membrane Science, 375 (2011) 1-27.

3

In situ methods for Li-ion battery research: A review of recent developments

This chapter has been published as PPRML Harks, FM Mulder, PHL Notten, Journal of power sources 288, 92-105 (2015)

Abstract

A considerable amount of research is being directed towards improving lithium-ion batteries in order to meet today's market demands. In particular *in situ* investigations of Li-ion batteries have proven extremely insightful, but require the electrochemical cell to be fully compatible with the conditions of the testing method and are therefore often challenging to execute. Advantageously, in the past few years significant progress has been made with new, more advanced, *in situ* techniques. Herein, a comprehensive overview of *in situ* methods for studying Li-ion batteries is given, with the emphasis on new developments and reported experimental highlights.

3.1. Introduction

Society's increasing use of portable electronics, the need to balance the fluctuating output of renewable energy sources, and the rise of electric vehicles, put tremendous pressure on the further improvement of Li-ion batteries. As a result Li-ion batteries are studied extensively to optimize the existing technology and to discover new, more advanced, battery materials. In recent years a significant part of the investigations consisted of *in situ* studies. While in a state of operation batteries are complicated systems in which a variety of chemical and physical processes take place, such as volume changes, phase transitions, side reactions, *etc*. *In situ*, and in particular *operando* measurements, allow direct monitoring of these phenomena and thus offer the ability to directly link these processes to the electrochemical response of the battery. The Latin expression "*in situ*" literally means "in position", and in battery research this refers to measurements that are performed on materials in their original position inside the device, *i.e.* without dissembling the battery. This allows characterization to take place under more realistic conditions, contrary to *ex situ* measurements. *Ex situ* measurements can furthermore be disturbed as a result of contamination during sample preparation and handling between battery use and characterization. *Operando* characterization represents a special case of *in situ* research, where the battery is in operation, *i.e.* is being (dis)charged during characterization, allowing measurements of non-equilibrated states that cannot be disclosed with *ex situ* characterization.

However, in order to conduct *in situ* experiments, batteries must be fully operational under the circumstances imposed by the diagnostic tool, which often demands specially designed devices and measurement setups, thereby hindering straightforward application of *in situ* techniques. Fortunately *in situ* methods to characterize Li-ion batteries recently experienced a rapid development, which is evident from the increasing amount of publications on this topic. All recent studies known to the authors, relevant to this topic, are listed in **table 3.1**.

At present one review article which focusses on microscopic techniques [1], and a few brief overviews [2, 3] of methods for *in situ* Li-ion battery research exist. In this review a comprehensive overview is given of recent *in situ* Li-ion battery research, in which techniques, cell design, as well as scientific results are described. The focus will be on recent developments and the challenges and requirements regarding the specially designed electrochemical cells.

Table 3.1
In situ research on Li-ion batteries from 2009 onwards

In situ technique	Investigated material
X-ray techniques	
X-ray diffraction	$Ag_2VO_2PO_4$ [4] Ag_2VPO_8 [108, 109] C [13] CuF_2 [110] Ge [111] $LiFePO_4$ [5, 112, 113] Li_2FeSiO_4/C [8] $Li[Li_{0.2}Ni_{0.2}Mn_{0.6}]O_2$ [6] $Li_{1.2}Co_{0.1}Mn_{0.55}Ni_{0.15}O_2$ [114] $LiCoPO_4$ [115] Li_2FeSiO_4 [16] $LiMn_2O_4$ [116] $0.5Li_2MnO_3{\cdot}0.5LiNi_{0.292}Co_{0.375}Mn_{0.333}O_2$ [117] $LiNi_{0.5}Mn_{1.5}O_4$ [118, 119] $Li_xMn_{1.5}Ni_{0.5}O_4$ [120, 121] $LiNi_{0.8}Co_{0.2}O_2$ [122] $Li_{1.23}Ni_{0.09}Co_{0.12}Mn_{0.56}O_2$ [123] $LiNi_{0.5}Mn_{1.5}O_4$ [124] Li_2RuO_3 [125] $K_{0.25}Mn_2O_4$ [126] Si [12, 127] Sn [128] Sn-C [129] $Sn_{30}Co_{30}C_{40}$ [130] $Sn_{27}Cu_{31}C_{42}$ [7] TiO_2 [131, 132] V_2O_5 [133]
Coherent X-ray diffraction imaging	$LiNi_{0.5}Mn_{1.5}O_4$ [134]
X-ray absorption spectroscopy	CuF_2 [110] Ge [135] FeF_3 [136] $LiCoO_2$ [22, 137, 138] $LiFePO_4$ [22, 23, 86, 112] Li_2FeSiO_4 [16, 19] $Li_{1-x}Mn_{0.5}Fe_{0.5}PO_4$ [139] $Li_{1.2}Mn_{0.525}Ni_{0.175}Co_{0.1}O_2$ [140] Li_2MnSiO_4 [19] $Li_{1.2}Ni_{0.15}Co_{0.1}Mn_{0.55}O_2$ [141] $Li[Ni_{0.17}Li_{0.2}Co_{0.07}Mn_{0.56}]O_2$ [18] $LiNi_{0.5}Mn_{1.5}O_4$ [124, 142] Li_2RuO_3 [125] $Li_3V_2(PO_4)_3$/C [143] Mn_3O_4 [15] RuO_2 [21] TiO_2 [132, 144] V_2O_5 [133]
Transmission X-ray microscopy	CuO [17] $LiFePO_4$ [27] Sn [26, 145] SnO [146] SnSb [145]
X-ray tomographic microscopy	Cu_6Sn_5 [147] Li [148] Ge [30] $Li_{1.2}Mn_{0.525}Ni_{0.175}Co_{0.1}O_2$ [140] Mn_2O_4 [149] Si [150] Sn [29] SnO [28]
X-ray photoelectron spectroscopy	$Li_xV_2O_5$ [151]
X-ray fluorescence	$Sr_2MnO_2Cu_{3.5}S_3$ [152]
X-ray scattering	Reduction of $LiPF_6$ electrolyte [153] SEI on graphene [154]
Scanning probe microscopy	
Atomic force microscopy	C [155] $LiCoO_2$ [35] $LiFePO_4$ [2, 34] Si [31, 156, 157] Sn [158] Sn–Co–C [159] TiO_2 [32, 33] SEI on C [160] SEI on $LiNi_{0.5}Mn_{1.5}O_4$ [161]
Scanning electrochemical microscopy[a]	C [162] $LiFePO_4$ [163] MnO/Al_2O_3 [53] Si [36, 37, 164, 165] Sn [37]
Electron Microscopy	
Scanning electron microscopy	$Li(Ni_{0.8}Co_{0.15}Al_{0.05})O_2$ [40] Si [38, 166, 167] SiO [166] SnO_2 [39] lithium plating and stripping reactions [168-170]
Transmission electron microscopy[b]	CeO_2/graphene [171] Co_3O_4/graphene [172, 173] CoS_2 [174] Co_9S_8/Co-filled carbon nanotubes [175] CuO [176] FeF_2 [177] Fe_2O_3/graphene [178] Ga [179] Ge [180] graphene [181] LiCl [182] $LiFePO_4$ [51, 183-185] $LiMn_2O_4$ [186] Li_2O_2 [187] LiV_2O_4 [188] $MnFe_2O_4$/graphene [189] MoS_2 [190] NiO/graphene [191] Si [48, 54, 192-197] Si/C [198, 199] Si/graphene [200] Si/polymer [201] SiO_2/SiC [202] Sn [49, 203] SnO_2 [204-206] SnO_2/C [207] PbSe/graphene [208] TiO_2 [209, 210] Ti_3Sn/NiTi [211] RuO_2 [212] ZnO [213] Zn_4Sb_3 [214] all-solid-state nanobattery [55]

Electron holography	all-solid-state thin film battery [58, 60]
Optical techniques	
Raman spectroscopy	Au/SiO_2 [67] C [65, 66, 68, 215-217] $LiCoO_2$ [62] $LiFePO_4$ [64] Li_2MnO_3 [63] $Li_4Ti_5O_{12}$ [218] Si [69] V_2O_5 [219] SEI on Li [220]
Fourier transform infrared spectroscopy	C [65, 68, 72, 221] $LiFePO_4$ [71] $LiMn_2O_4$ [222] $LiNi_{1/2}Mn_{3/2}O_4$ [222] Sn-Co [223] reduction/oxidation products of ionic liquids [70, 224]
Optical microscopy	C [73, 225-229] Li [230-233] Si [234]
Multi-beam optical stress sensor	C [235-237] Si [74, 238-245] Sn [246]
Valence-differential absorption spectroscopy	manganese ferrocyanide [247]
Nonlinear coherent vibrational spectroscopy	SEI on Cu and Au [248]
Magnetic (resonance) techniques	
Nuclear magnetic resonance spectroscopy	C [249, 250] Cu_3P [77] Li [83, 84, 251] $LiCoO_2$ [80] $Li_{1.08}Mn_{1.92}O_4$ [76, 79] Si [252, 253] liquid electrolytes [81, 82]
Magnetic resonance imaging	Li [84] Li||graphite [85] Li||$LiFePO_4$ [85] $LiPF_6$ electrolytes [254]
Mössbauer spectroscopy	$LiFe_{0.75}Mn_{0.25}PO_4$ [255] Li_2FeSiO_4/C [19] $LiMn_yFe_{1-y}PO_4$/C [87] Sn/BPO_4 [88] $Sn_{27}Cu_{31}C_{42}$ [7] $Sn_{30}Co_{30}C_{40}$ [130]
Electron paramagnetic resonance spectroscopy	Li [256]
Electron magnetic measurements	$FeSb_2$ [257]
Neutron techniques	
Neutron diffraction	C [91] $LiCoO_2$ [99] $Li(Co_{0.16}Mn_{1.84})O_4$ [258] $LiFePO_4$ [91, 92, 97] $Li[Li_{0.2}Ni_{0.18}Mn_{0.53}Co_{0.1}]O_2$ [95] $LiMn_2O_4$ [99, 259, 260] $LiNi_{1/3}Mn_{1/3}Co_{1/3}O_2$ [95] $LiNi_{0.5}Mn_{1.5}O_4$||$Li_4Ti_5O_{12}$ [261] $Li_4Ti_5O_{12}$ [98, 262] MoS_2 [263] TiO_2/$Li_4Ti_5O_{12}$ [264] commercial batteries [25, 93, 94, 96, 265-271]
Neutron reflectometry	Si [101, 272] SEI on carbon [100] SEI on copper [273] SEI on $LiMn_{1.5}Ni_{0.5}O_4$ [102] commercial batteries [107, 274]
Neutron radiography	C [275, 276] $LiFePO_4$ pouch cell [277]
Neutron depth profiling	Sn [106, 278] all-solid-state thin film battery [105]

a This includes scanning ion conductance microscopy and electrochemical strain microscopy
b Only studies that have not been reviewed earlier [3, 42, 43] have been included in this table

3.2. X-ray techniques

3.2.1. X-ray diffraction

X-ray diffraction (XRD) is based on the scattering of X-rays by periodically spaced atoms in a crystal, producing a diffraction pattern that yields information about the crystallographic structure. In *in situ* battery research the method is used to monitor the structural evolution in an electrode as the (electro)chemical processes take place. For spatially resolved measurements energy dispersive XRD can be applied [4].

To conduct XRD measurements on an operating battery, an X-ray transparent window needs to be incorporated in the design in order to allow the X-rays to reach the electrode(s) under investigation. This can be done by using a battery with a very thin (~10 μm) current collector, without an additional casing [5]. This design does allow penetration of the incident X-ray beam, but this setup is also relatively vulnerable to air and moisture contamination. Therefore normally only a small part of the electrode is exposed by creating a hole in a much thicker protective casing or current collector, which in turn is sealed by a X-ray transparent material such as a Kapton foil [6] or Beryllium [7]. However Be, more particularly Be-oxide, is highly toxic and for the study of cathodes an additional protective layer is required to prevent corrosion of the beryllium at higher potentials. Recently conductive Kapton foil has also been employed as both the X-ray window and current collector [8]. Furthermore flexible [9], low-cost [10], battery designs for *in situ* XRD measurements are available, for which a proper pressure applied to the cell is essential to obtain reliable results [9, 10]. Standard batteries, without modification, can be investigated by means of synchrotron-based high energy XRD [11-13]. As the high energy photons are able to fully penetrate the cell these measurements are conducted in the transmission mode in order to obtain 2D-diffraction patterns. This also means that the cathode and anode can be investigated simultaneously. A historical overview of *in situ* XRD cell designs can be found elsewhere [14].

An exemplary study of the added value that *in situ* measurements can have is the XRD study of Misra *et al*. [12] on the (de)lithiation mechanisms in Si nanowires. The measurements revealed the formation of the metastable crystalline $Li_{15}Si_4$ phase at low lithiation voltages. Previous *ex situ* studies showed that Si nanowires gradually lose their crystallinity during lithiation and become completely amorphous at the end of the cycle. The development of the transient $Li_{15}Si_4$ phase, which only can be disclosed through *in situ* characterization, reduces the cycle-life performance of Si-nanowire electrodes significantly. The authors show that by either limiting the cycles to a more positive cut-off voltage or adjusting the growth parameters of the nanowires, the formation of $Li_{15}Si_4$ during lithiation can be prevented, resulting in an improved capacity retention.

3.2.2. X-ray absorption spectroscopy

X-ray absorption spectroscopy (XAS) is used to determine the local geometric and electronic structure of a material, associated with the redox reactions that take place in batteries. The absorption spectra feature two main regions, each of which disclose very specific information. The X-ray near-edge spectroscopic (XANES) part of the spectra provides information, among other things, about the oxidation state,

while from the extended X-ray absorption fine structure (EXAFS) region information about the molecular structure can be obtained.

XAS cells for *in situ* measurements are very similar to the cells used for XRD research. However, XAS spectra are mostly obtained in the transmission mode, and the thick casing batteries therefore require two X-ray transparent windows at symmetric positions at the top and bottom of the cell [15, 16]. To allow better penetration of the X-rays, carbon paper can be used as current collector instead of metal foils [17]. Standard pouch [18] and coffee bag [19] batteries can be employed without modification as the high energy photons that are applied for XAS are able to penetrate the entire battery stack. Furthermore the X-ray energy is tuned to the absorption edge of the element of interest and therefore absorption by other elements present in the battery components can be minimalized [20].

Recently several noteworthy *in situ* XAS papers have been published. For example, Hu *et al*. [21] unraveled the origin of the additional storage capacity found for nano-sized metal oxide conversion materials by using a combination of *in situ* XRD, EXAFS and XANES, together with *ex situ* NMR. Conversion materials, such as a metal oxide (M_xO_y), can reversibly react with lithium forming metal particles embedded in a metal oxide matrix, according to

$$M_xO_y + 2yLi^+ + 2ye^- \rightleftarrows xM^0 + yLi_2O \quad (1)$$

The metal oxides, in this study RuO_2, show more reversible capacity than estimated based on the reduction of the metal oxide to M^0. The reason of this extra storage capacity is often thought to originate from the development of a so-called space-charge layer at the interface of the metal and lithium oxide particles. In this layer Li^+ ions can accumulate, charge compensated by electrons in the metal. However, the authors show that the additional storage capacity arises from the reversible reaction of LiOH with Li to form LiH and LiO_2. The LiOH is formed from the reaction of Li and surface OH^--groups naturally present on the RuO_2 nanoparticles. Although the formation of LiOH is considered to be mainly responsible for the additional storage capacity, the authors suggest that reversible SEI formation and simple Li adsorption on the Ru nanoparticles also may have minor contributions.

Yamamoto and co-workers [22] applied total-reflection fluorescence XAS to directly monitor the electronic structure at the electrode/electrolyte interface. This type of XAS can be used to perform surface sensitive measurements. The measurements showed that for a $LiCoO_2$ thin film electrode that exhibits gradual degradation upon electrochemical cycling, the Co-ions at the interface were reduced upon immersion in an organic electrolyte. Consequently, irreversible changes in the electronic structure at the interface were observed upon cycling. In contrast, in a $LiFePO_4$ thin film electrode with stable cycling performance, the electronic structure at the interface did not change and showed reversible cycling behavior. The stability of $LiFePO_4$ was attributed to the absence of a large potential drop across the space charge layer at the electrode surface. This study demonstrates a correlation between the stability of the electronic structure at the electrode/electrolyte interface and the cycling performance of Li-ion batteries.

To study the charge dynamics of battery electrodes, Liu *et al*. [23] used soft X-ray absorption spectroscopy (sXAS) to probe the oxidation state of metal ions in

cathode materials during battery operation. Due to the short penetration depth of soft X-rays, the measurements require an ultra-high vacuum and are performed in the reflection mode. Detection holes were created across the current collector to expose some regions of the cathode material directly to the incident x-ray beam. During charging of $LiFePO_4$ (LFP) electrodes the iron atoms in the probed regions predominantly retained their 2+ oxidation state and surprisingly even remained in this state when the battery was fully charged up to 4V. Only after a relaxation period of 40 hours under open-circuit condition a strong signal, corresponding to the charged state (Fe^{3+}), was observed. This indicates the existence of metastable phases that deviate from the well-known two-phase transformation that is expected to evolve in time. Indeed the exact (de)lithiation mechanism of LFP is still subject of debate [24, 25]. Based on these results and additional *ex situ* measurements, the authors conclude that upon cycling the change in State-of-Charge (SoC) starts in the region adjacent to the current collector as indicated in **Fig. 3.1**. This contradicts the conventional consensus that the ionic conductivity is the rate-limiting process, which would cause the SoC changes to start at the cathode/electrolyte interface. Measurements were also conducted on $LiCo_{1/3}Ni_{1/3}Mn_{1/3}O_2$ (NMC) where no large SoC gradients were observed. The authors designated the difference in behavior of the two cathode materials to a different (de)lithiation mechanism, *i.e.* two-phase transformation for LFP *versus* a solid-solution mechanism for NMC, a difference in particle morphology and the difference in their respective ionic/electronic conductivity. The authors point out that due to the surface sensitivity of the applied method, local phenomena could be distinguished from the bulk behavior.

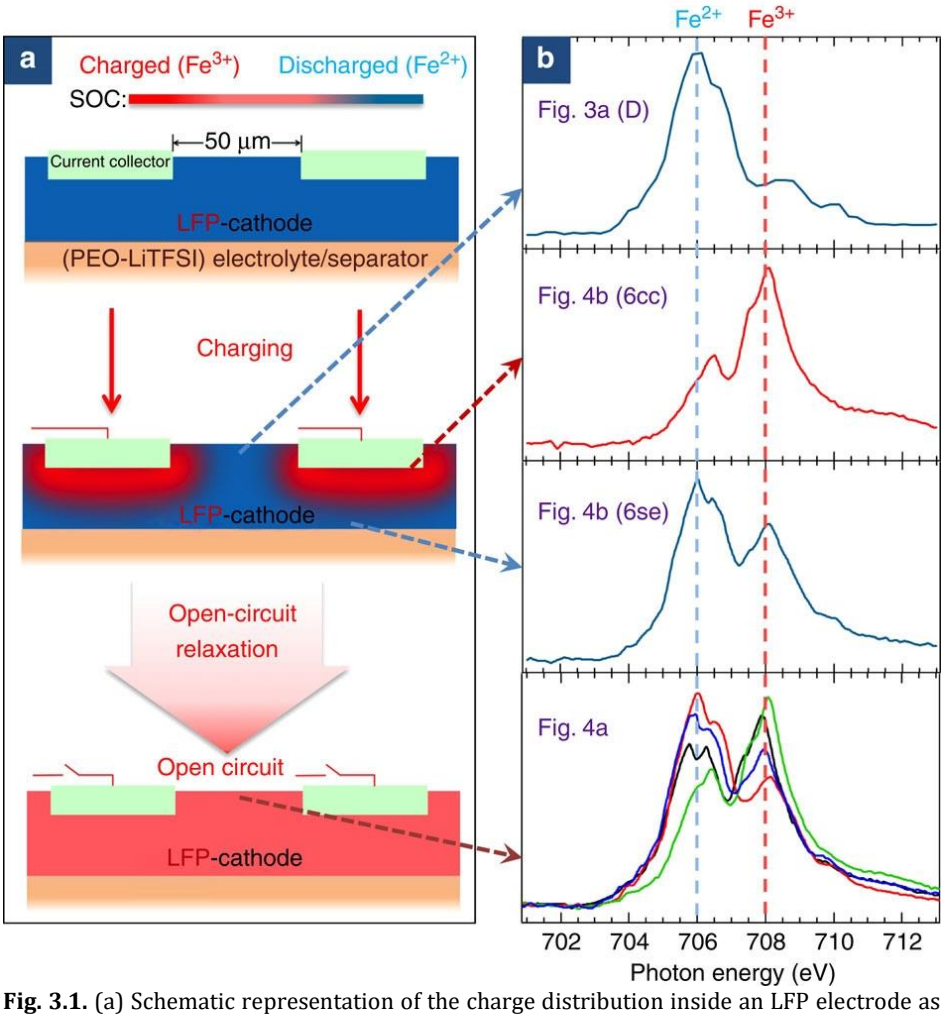

Fig. 3.1. (a) Schematic representation of the charge distribution inside an LFP electrode as revealed by combined *in situ* and *ex situ* sXAS. The SoC distribution after charging (middle panel) equilibrates during open-circuit relaxation (bottom panel) at the same SoC. (b) Corresponding sXAS spectra. Reprinted by permission from Macmillan Publishers Ltd: Nature Communications ref. [23], copyright (2013).

3.2.3. Transmission X-ray microscopy

With transmission X-ray microscopy (TXM), monochromatic X-rays are directed onto the sample under investigation and the radiation passing through is projected onto a CCD camera. In this way 2D images can be rendered of the internal electrode particle morphology.

As for many X-ray techniques, coin cells of which the covers of both sides are perforated and sealed with Kapton tapes to allow the X-ray beam to pass through can be used to facilitate this method [26].

Wang and colleagues [17] applied this method in combination with *in situ* XANES to map the chemical phase changes as well as the morphological development of

CuO electrode particles during electrochemical cycling. In their subsequent study the same combination of techniques has been used to monitor the delithiation process of $LiFePO_4$ *operando* [27].

3.2.4. X-ray tomographic microscopy

X-ray tomographic microscopy is an advanced form of TXM for which the *in situ* cell can be rotated through 180° to obtain a series of 2D images. From these 2D images, 3D microstructure representations can then be reconstructed using a tomographic algorithm. Observations of the changes in attenuation coefficient are related to changes in composition and mass density, enabling visualization and quantification of the phase transitions of electrode particles.

To allow such 180° rotation without blocking the X-ray beam, cells devised for *in situ* measurements often have a cylindrical shape and are made from a highly X-ray transparent material. Examples are a polymeric Swagelok cell [28] and a Kapton capillary tube cell [29]. The X-rays are directed onto the working electrode from the side of the cell to limit the battery components in the path of the beam. A conventional pouch cell has also been used [30]. Due to its flat design the angular range that can be measured is limited to 140° but this is sufficient to reconstruct high quality 3D images. As in this configuration the current collector is in the pathway of the X-ray beam, it should be kept very thin, of the order of less than 2.5 μm.

Recently Ebner *et al*. [28] were the first to apply *in situ* X-ray tomography to investigate Li-ion batteries. In their study the morphological evolution as well as the change in chemical composition of individual SnO particles upon (de)lithiation were monitored. Three dimensional images could be rendered with a resolution of 2.0 μm. **Fig. 3.2** shows the progress of the conversion reaction of SnO into Sn and LiO_2 according to Eq. 1, and the subsequent alloying of Li and Sn. The lithiation of the SnO particles leads to volume expansion and crack formation. Impressively, the authors were able to quantitatively link the electrochemically measured capacity losses to the observed electrically disconnected particles. More recently this technique has also been used to investigate Sn [29] and Ge [30] electrodes upon cycling, achieving even nanometer scale visualization.

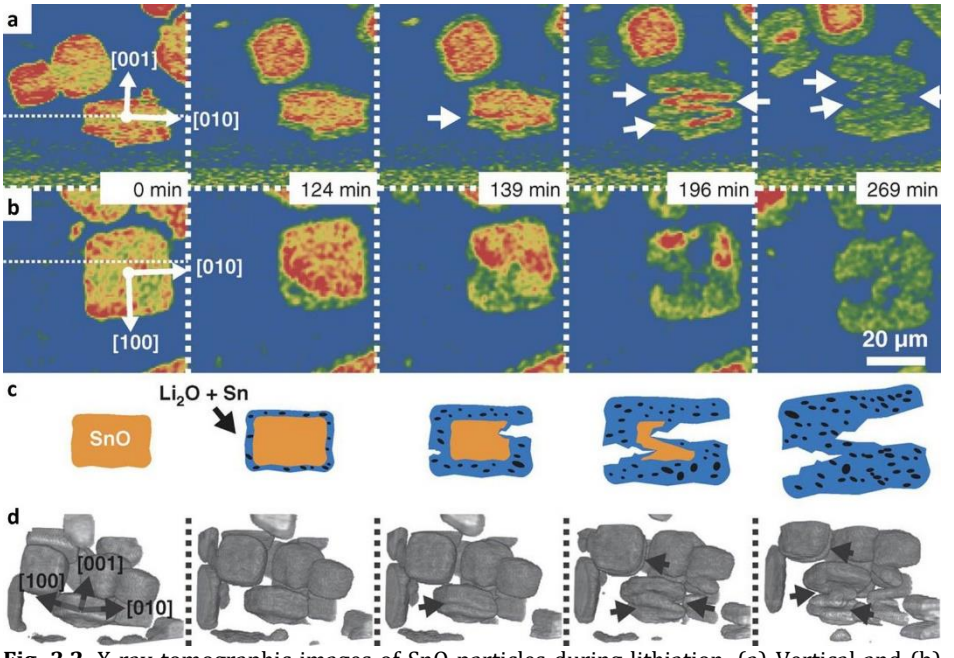

Fig. 3.2. X-ray tomographic images of SnO particles during lithiation. (a) Vertical and (b) horizontal cross sections through a SnO particle during electrochemical reduction. Cross sections at 0 min are indicated by dashed white lines revealing the cutting planes. The white arrows point out crack locations. (c) Schematic representation of phase evolution and crack development of a SnO particle due to lithiation. (d) 3D rendering of sub-volume. Black arrows indicate fracture. Adapted from ref. [28], with permission from AAAS.

3.3. Scanning probe microscopy

3.3.1. Atomic force microscopy

Atomic force microscopy (AFM) is based on the deflection of a cantilever with a sharp tip to examine surfaces. By scanning the interphase between the electrode and the liquid electrolyte, a height distribution is obtained, and thus volume changes and/or SEI formation upon cycling can be visualized. Furthermore through AFM enabled nano-indentation [31], the mechanical properties of nanostructures during (de)lithiation can be measured. In most of the *in situ* AFM studies a passive probe is used, *i.e.* no electronic stimulus is supplied via the cantilever. Voltage-biased AFM [32, 33], where the tip is acting as a current collector, allows studying the surface potential and topographic changes as a function of the applied voltage.
Obviously a critical feature of an *in situ* AFM design is the access of the cantilever into the battery. As an opening is necessary to facilitate the cantilever, measurements are often performed under inert atmosphere inside a glove-box to exclude contamination. The opening should be kept small and properly sealed since evaporation of the organic solvent will influence the measurements due to an increasing salt concentration of the electrolyte over time [34]. In order to scan the working electrode it should be sufficiently exposed and therefore the counter and reference electrodes are typically positioned to the sides of the working electrode

as shown in **Fig. 3.3**. An elaborate discussion of the design guidelines for *in situ* AFM cells can be found in ref. [34].

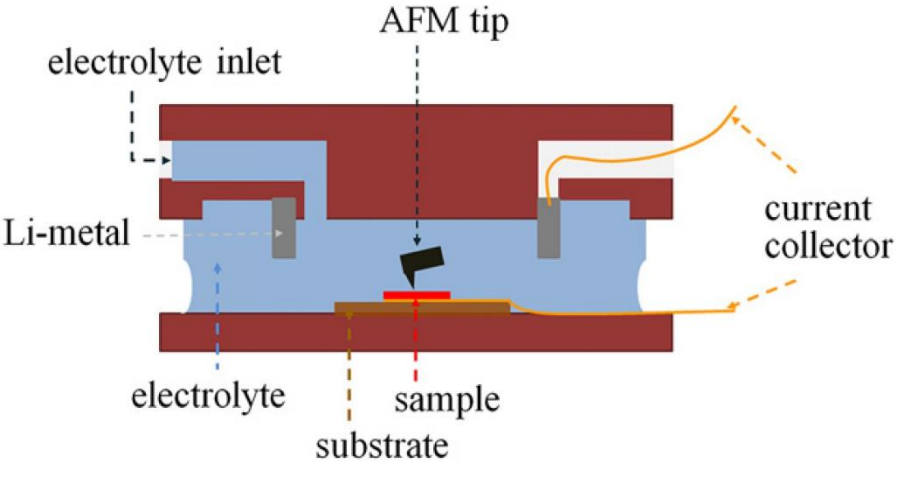

Fig. 3.3. Schematic representation of an AFM cell for *in situ* measurements. The thin film electrode is located at the bottom of the electrochemical cell. The current collector is located between the thin film and the substrate. Reprinted with permission from ref. [35]. Copyright © 2012 Elsevier B.V.

3.3.2. Electrochemical strain microscopy

An adapted form of AFM has recently been developed to study the lithium motion on a nanometer scale. This technique, denoted electrochemical strain microscopy (ESM) [36], is based on the application of periodic high frequency voltage-bias between the cathode and anode. The resulting oscillatory surface displacement on top of the thin film battery can then locally be detected by the AFM tip. The amplitude of the surface displacement is directly related to the change in Li-ion concentration induced by the applied bias. Since with this technique the Li-ion transport is probed by measuring the strain and not by an electric current as is traditionally done, the obtained resolution is much higher due to the sensitivity of the AFM.

The method can be applied to all-solid-state thin film batteries where the top current collector is omitted allowing the conductive cantilever to directly scan the top-electrode and act as the current collector. All ESM measurements of Li-ion batteries so far have been conducted in ambient air.

3.3.3. Scanning ion conductance microscopy

Scanning ion conductance microscopy (SICM) offers the opportunity to directly measure ionic currents as well as the surface topography by the application of a nano-scale pipette that scans the electrode at the electrode/liquid electrolyte interface. The spatial resolution depends on the pipette tip geometry and is therefore practically limited to tens of nanometers. The current sensitivity can reach sub-pA levels.

A relatively simple setup is used for this method as shown in **Fig. 3.4**. It consists of a petri dish to immerse an electrode in electrolyte and a pipette containing a lithium source that scans the interface while oscillating in the vertical direction. The apparatus is housed inside an argon glove-box.

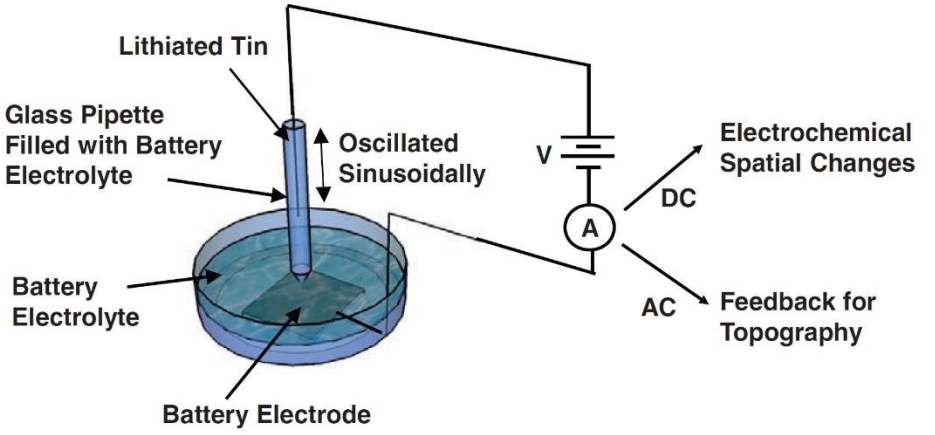

Fig. 3.4. Schematic representation of an *in situ* SICM configuration. Reprinted with permission from ref. [37] Copyright © 2011 WILEY-VCH.

3.4. Electron microscopy

3.4.1. Scanning electron microscopy

Scanning electron microscopy (SEM) is based on electrons to construct an image. An electron beam is focused on a sample and either the backscattered electrons or the secondary electrons emitted by the available atoms are detected. The technique offers a good spatial resolution to investigate morphological changes during battery operation, such as electrode volume expansion/shrinkage, electrode crack formation and delamination. Electron microscopes are often equipped with additional spectroscopy and diffraction tools that can give more detailed information. Force sensors and a piezo-actuators can be housed inside the SEM chamber to conduct mechanical experiments [38].

The monitoring ability is restricted to the outer surface and therefore the applied cells must have an open structure, where the electrode is directly exposed to the electron beam. Measurements require high vacuum and therefore *in situ* cells should be highly compatible with vacuum conditions. This can be achieved with batteries based on solid, polymer or low vapor pressure electrolytes, such as ionic liquids. To meet the requirements of having an open structure and vacuum compatibility an electrochemical cell can be employed that consists of a current collector mesh that is coated with electrode material in combination with an ionic electrolyte [39]. In this configuration the current collector does not obscure the electrode and the mesh allows permeation of the ionic liquid electrolyte to provide ionic contact. Another approach, applied by Miller *et al*. [40], is to assemble the battery inside the SEM chamber. **Fig. 3.5** shows the actual setup. It consists of an electrode particle which is attached to a manipulator probe. The probe, also serving

as electric lead, is used to bring the particle into contact with a droplet of ionic liquid electrolyte which covers the counter electrode.

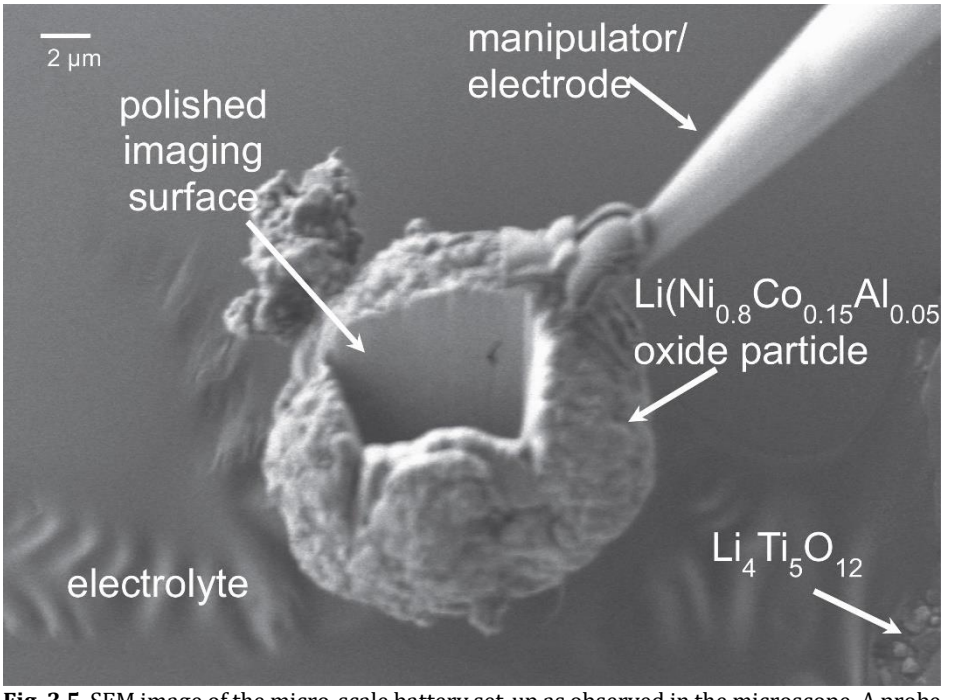

Fig. 3.5. SEM image of the micro-scale battery set-up as observed in the microscope. A probe is used to bring a single electrode particle into contact with an electrolyte droplet covering the counter electrode. The particle is etched with a focused ion beam for imaging purposes. Reprinted with permission from ref. [40]. Copyright © 2013 WILEY-VCH.

3.4.2. Transmission electron microscopy

Unarguably the biggest recent breakthrough in the field of *in situ* techniques for battery research has been the development of *in situ* transmission electron microscopy (TEM). After the initial work of Huang *et al*. [41] in 2010 on the (de)lithiation of a single SnO_2 nanowire, many reports on nanostructured electrodes studied by *in situ* TEM followed. Several reviews on the subject are available [3, 42-44].

With TEM electrons are detected that are transmitted through the sample of interest to construct an (atomic-scale) image, and therefore only ultra-thin samples *i.e.*, nano-batteries, can be investigated. In addition to the morphological changes that can be observed during battery operation, additional integrated techniques, such as electron diffraction and electron energy loss spectroscopy (EELS), can provide information about the local composition and structure.

TEM requires a high vacuum for its operation. Therefore liquid electrolyte batteries need to be sufficiently sealed to prevent electrolyte evaporation. This however requires extra material which adds to the thickness of the cell. To keep the cell as thin as possible and compatible with vacuum conditions, all-solid-state batteries or batteries containing ionic liquid electrolytes with an extremely low vapor pressure

are applied. **Fig. 3.6** shows the conventional set-ups for *in situ* TEM, the so called end-contact configuration where only a fraction of the nano-electrode under investigation is connected to either a solid- or ionic liquid electrolyte, which in turn is connected to a lithium source.

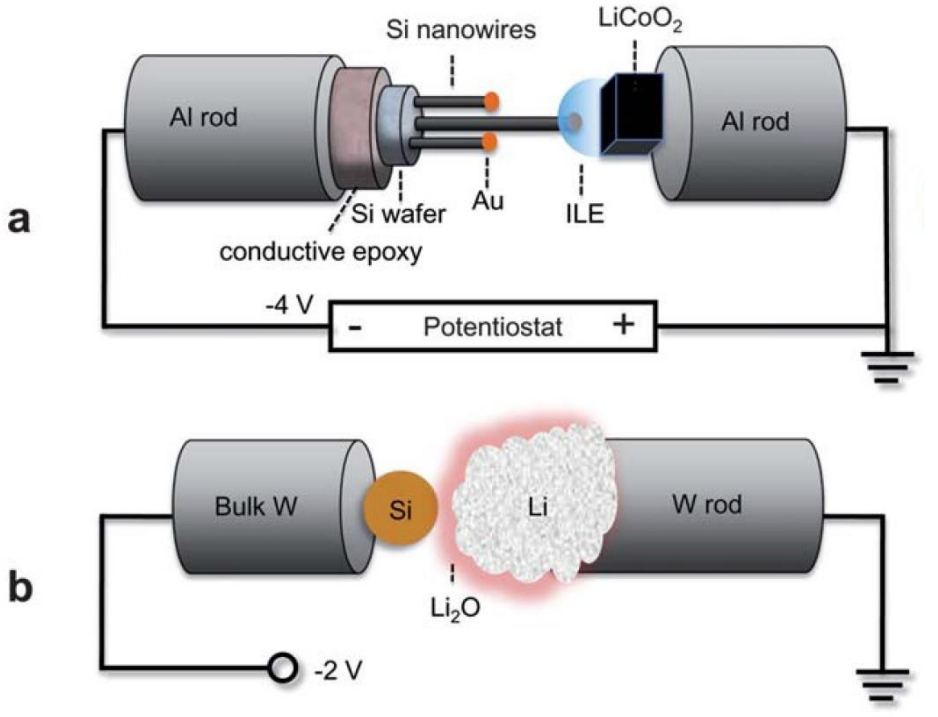

Fig. 3.6. Schematic representation of the open cell nano-battery setup, enabling *in situ* TEM. (a) Ionic liquid electrolyte (ILE) containing cell; a drop of the ILE is placed on the tip of a bulk cathode and long objects, such as nanowires, are used as anode. (b) Solid-state electrolyte cell; metallic Li acts as lithium source on which a naturally formed thin Li_2O layer serves as solid-state electrolyte. This configuration is suitable for small objects of interest, such as nanoparticles. Adapted from ref. [3] with permission from The Royal Society of Chemistry.

Amazing breakthroughs have taken place in the *in situ* TEM-monitoring of rechargeable batteries. However, many authors recognize the difference in configuration as well as testing methods, between the investigated nano-batteries and bulk-size batteries that are used in practice [42, 43, 45]. For instance, due to the required nano-sized configuration of the batteries, the contacts are very small and often non-optimized, inducing significant overpotentials during battery operation, which might influence their characteristics. Also, the currents involved in (de)lithiation processes of TEM batteries are often too small to be controlled in a galvanostatic mode, which hinders easy comparison with other battery research. Furthermore, the high energy electrons can induce crystallization or dissociation of materials [46]. Another concern is the use of vacuum compatible electrolytes. These electrolytes not necessarily influence the battery behavior as such, but do differ from the organic solvent-based electrolytes in conventional batteries. Lastly, during

the TEM measurements the electrode typically only has a small part of its outer surface in contact with the electrolyte, whereas in a normal battery it would be entirely immersed in the electrolyte, the so called “flooding geometry”.

In response to these limitations some *in situ* TEM investigations have been deviating from the general set-ups described above. For instance, Zhong *et al*. [47] reported on a SnO_2 nanowire partially flooded in an ionic liquid for which very different lithiation behavior was found compared to a SnO_2 electrode in the conventional setup in an earlier study [41]. The flooded geometry exposed a new type of lithiation, in which oblique stripes were formed across the width of the nanowire, after which elongation and swelling of the wire occurred. Gu and co-workers [48] were able to conduct *in situ* TEM measurements on a silicon nanowire cell, containing a liquid electrolyte. To this end a design was used consisting of SiN membranes to contain the liquid. A similar design was used earlier for *in situ* electron diffraction measurements during electrochemical cycling of a thin film of Sn [49]. The configuration was kept thin enough to allow transmission of electrons for imaging. Because the silicon nanowire is fully immersed in the electrolyte, lithiation indeed proceeds by uniform swelling along the axial axis of the entire nanowire. This is different from the lithiation of a silicon nanowire connected at only one end to electrolyte, featured by a reaction front advancing in the axial direction [50]. **Fig. 3.7** shows both situations.

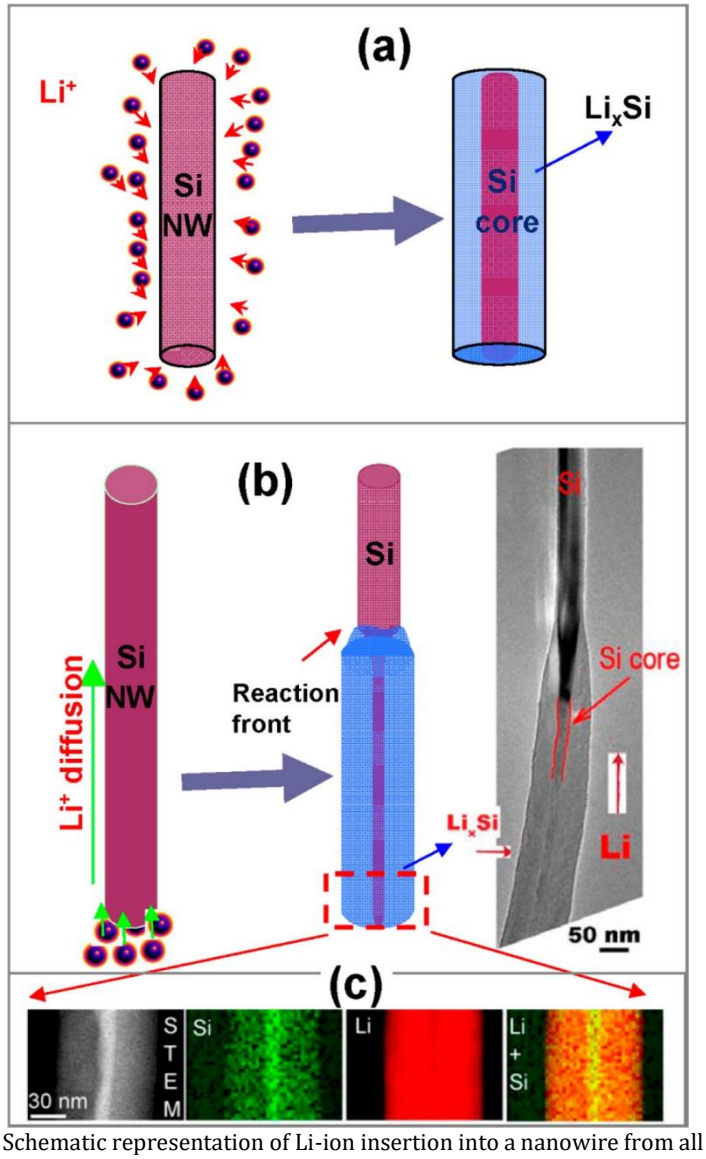

Fig. 3.7. (a) Schematic representation of Li-ion insertion into a nanowire from all directions, as is the case in a liquid cell. (b) Schematic representation of Li-ion insertion and diffusion in a nanowire partially in contact with the electrolyte. (c) STEM of Si, Li, and superimposed Si and Li EELS maps showing the distribution of silicon and lithium in the lithiated part of a nanowire. Reprinted with permission from ref. [48]. Copyright (2013) American Chemical Society.

With the configurations presented in the aforementioned studies, one is able to observe lithiation in a flooded geometry and potentially perform SEI analyses. However, due to the liquid electrolyte and the relatively thick membranes, these features are at the expense of spatial resolution and the ability to use the spectroscopy techniques available on electron microscopes. A type of spectroscopy

that recently has been performed on a liquid cell is valence EELS, which probes the low energy regime, and can be employed in thicker liquid layers than is typically feasible with conventional EELS [51].

A good example of new insight *in situ* TEM can provide is the study of Liu *et al*. [52] on aluminum nanowires and their native oxide layers. It shows that upon cycling, prior to the metal core, the metal oxide layer (Al_2O_3) is lithiated first, turning into a Li-Al-O glass. The aluminum core pulverizes after delithiation but, remarkably, the nanowire as a whole maintains its mechanical integrity due to the Li-Al-O surface layer as shown in **Fig. 3.8**. Apparently the Li-Al-O glass acts as a SEI layer. It conducts Li-ions and mechanically confines pulverized particles, thereby preventing loss of active material. This finding clarifies some of the underlying principles of coating active battery materials with metal oxides such as Al_2O_3, which is a well-known strategy to improve the overall battery performance [53, 54].

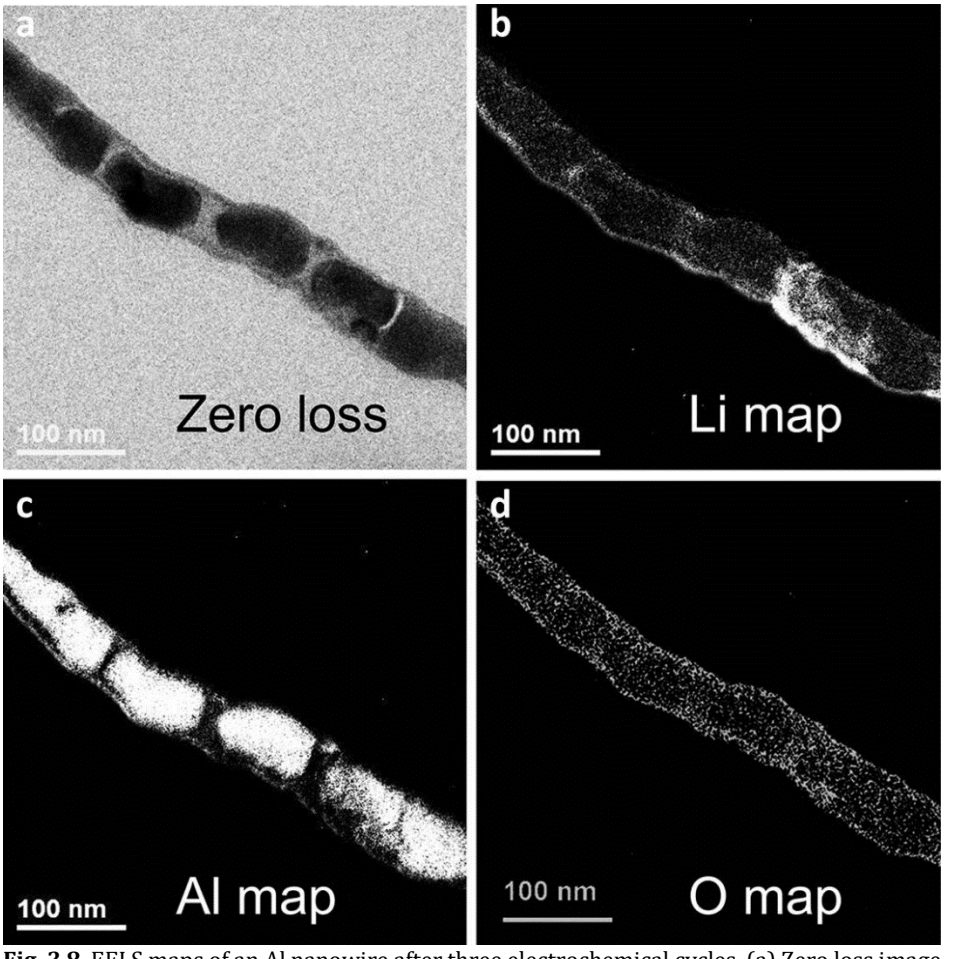

Fig. 3.8. EELS maps of an Al nanowire after three electrochemical cycles. (a) Zero loss image showing a pulverized nanowire, confined by a tube-like surface layer. (b–d) EELS maps of Li, Al, and O, respectively, revealing the nanoparticles are aluminum and the surface layer

consists of Li, Al, and O. A three-window technique was used to obtain the energy-filtered maps. Adapted with permission from ref. [52]. Copyright (2011) American Chemical Society.

Another interesting TEM study concerns the scaling limits of batteries. Ruzmetov and colleagues [55] investigated all-solid-state nano-batteries with a radial geometry, which were fabricated by subsequent (physical vapor) deposition of the various components onto Si nanowires. Based on their current-voltage characteristics the authors argue that the only 110 and 180 nm thick (LiPON) electrolyte layers were pin-hole free. However, the batteries suffered from severe self-discharge which, according to the study, is caused by the nano-scale dimensions of the electrolyte layer and the resulting onset of space-charge limited electronic conduction. The results show that in addition to the layer quality, other fundamental effects determine the scaling limits for nano-batteries.

Considering the early stage of development of *in situ* TEM for Li-ion batteries, an impressive amount of publications is already available. It therefore seems apparent that the method will continue to develop in the near future, also in terms of generating results that relate more to the world of real-life batteries. However, even in this stage a good consistency exists between the experimental data obtained by *in situ* TEM and other *ex situ* studies on bulk-type batteries [42].

3.4.3. Electron holography

In electron holography [56, 57] the sample is exposed to an electron beam of which the phase will be modulated by the electrostatic potential and magnetic field across the samples. The signal coming from the sample and a reference signal are let to interfere with each other, which results in a hologram, *i.e.* an interference fringe pattern. The phase modulation extracted from the hologram is used to reconstruct the electrostatic and/or magnetic fields in the samples, *e.g.* the inner mean potential.

Yamamoto *et al*. [58] applied the relatively unknown technique of electron holography to map the electric potential distribution across the cathode/solid electrolyte interface during battery operation. The authors used a planar thin film all-solid-state battery of which the area of interest was thinned down by a focused ion beam to 60 nm for TEM observation. **Fig. 3.9** shows a typical distribution of the measured potential together with the analyses of the lithium and electron distribution during charging. As can be seen, the profile has a linear voltage slope inside the cathode, a steep voltage drop across the interface and a more gradual slope in the solid electrolyte. The steep drop at the interface is consistent with the general consensus that voltage drops are mainly concentrated at the electrode/electrolyte interfaces. However the authors point out that the gradual slope of the potential distribution in the solid electrolyte is not easily accounted for. The length of about 1.5 μm is orders of magnitude bigger than the estimated Debye length, which is considered a measure of the thickness of the electrical double layer. The Debye length for this material, as calculated from the Gouy-Chapmann theory, only amounts to a few angstroms. It is furthermore remarkable that the obtained width of the space charge layer is of the same size of the entire electrolyte layer in conventional thin film batteries [59]. In a second paper using electron holography the anode side of the electrochemical cell has been investigated [60].

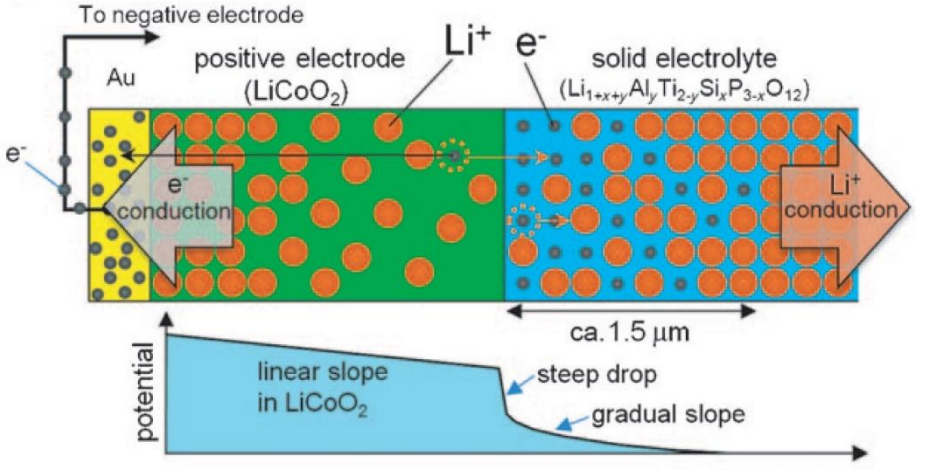

Fig. 3.9. Schematic representation of the formation of an electric double layer during battery charging. Distribution of lithium and electrons near the positive-electrode/electrolyte interface (top) and typical distribution of the measured potential distribution (bottom). Reprinted with permission from ref. [58]. Copyright © 2010 WILEY-VCH.

3.5. Optical techniques

3.5.1. Raman spectroscopy

Raman spectroscopy is based on the inelastic scattering of monochromatic light when it interacts with the sample. The shifts in wavelength or photon energy of the scattered light correspond to the vibrational modes of the system, which are characteristic for Raman-active molecules. Consequently, structural changes of electrodes during cycling can be determined. An extensive publication on *in situ* Raman spectroscopy in electrochemical research can be found elsewhere [61].

As an optical pathway needs to be created for laser light to reach the electrode, normally an opening in the *in situ* cell should is provided in the outer casing behind which a piece of thin glass is applied. This creates a window for the laser light to go through. In order to reach the electrode, two configurations can be used [62]: The first configuration [63, 64] makes use of a top current collector foil perforated near the casing opening, or is based on a current collector grid for which the mesh size is approximately an order of magnitude smaller than the laser beam diameter. The second option [65] comprises of a current collector, a lithium foil and separator, which are all configured with a hole to expose the second electrode at the bottom of the electrochemical cell. However, as the separator has been perforated in the second configuration, the examined electrode area may not have an optimal ionic connection to the counter electrode [62]. Furthermore the first configuration allows the glass window to be close to the electrode under investigation. Therefore the amount of liquid electrolyte in the pathway of the laser light can be kept to a minimum to limit the undesired scattering of light by the electrolyte [65, 66].

Combining complementary *in situ* techniques on the same cell is a powerful approach to investigate Li-ion batteries. Hy *et al*. [67] studied the SEI formation and

evolution on SiO_2-coated Au nanoparticles during cycling, combining normal Raman spectroscopy with surface enhanced Raman spectroscopy to investigate the surface as well as the bulk of the electrode particles. A standard *in situ* Raman cell, as described above, can also be applied for surface enhanced measurements. Using the same strategy, combining Raman with a surface sensitive technique, Pérez-Villar and co-workers [65] combined Raman spectroscopy with Fourier transform infrared spectroscopy. A specially designed cell compatible with both techniques allowed measurements to be performed at the same location. The authors selected a window material (CaF_2) that is transparent to both types of light utilized for these techniques. Furthermore a microscope objective was applied, allowing the Raman signal to incident normal to the electrode and the infra-red beam under a variable angle of incidence. Information could be obtained about the surface species involved in the interfacial reactions as well as the structural changes of the glassy carbon electrode induced by electrochemical cycling. In a follow-up study the same combination of technique has been used to investigate a graphite electrode [68].

An interesting example of an *in situ* Raman study is the work on the effects of B and P dopants on the lithiation of crystalline Si. Long *et al*. [69] measured the intensity of the characteristic phonon mode corresponding to crystalline silicon as a function of the electrode potential *vs* a Li/Li^+ reference electrode. Since a decrease in the phonon mode intensity is indicative of the transition from crystalline to amorphous silicon, it corresponds to the onset of the lithiation process. The B-doped Si showed an onset potential for the phonon decay at 0.68 V, whereas that of P-doped Si was found at 0.09 V. The authors concluded that, among other things, the different Fermi levels in B- and P-doped Si are responsible for the difference in onset voltage for the initial Li insertion.

3.5.2. Fourier transform infrared spectroscopy

Fourier transform infrared spectroscopy (FTIR) is very similar to Raman spectroscopy, however, it is based on the absorption of infrared light rather than inelastic scattering. Due to the surface sensitivity of FTIR it is often applied to probe the interfacial reactions between a working electrode and the electrolyte in the reflective mode, but also to identify gas products that are formed, resulting from the reduction or oxidation of the electrolyte in the transmission mode.

A relatively large number of different battery set-ups for *in situ* FTIR research have been described [70-72]. Several window materials, that are transparent to infra-red light and allow the beam to reach the working electrode, have been applied. Examples are KBr [70], CaF_2 [71] and diamond [72]. Most experimental setups do not have a conventional half-cell, sandwich-like, structure but have a more open structure with the counter electrode positioned aside the working electrode. This configuration ensures good accessibility to the electrode of interest which is necessary as the infrared beam is incident at an angle to obtain maximum reflection intensity. Such a design furthermore allows the incorporation of a reference electrode. **Fig. 3.10** shows a schematic representation of an *in situ* FTIR cell. Positioning the IR-window as close as possible to the working electrode is critical to limit the light absorption by the electrolyte between the window and electrode. However, it should be taken into consideration that as the liquid

electrolyte film becomes too thin, the diffusion of electrolyte species to/from the electrode may become a limiting factor [72].

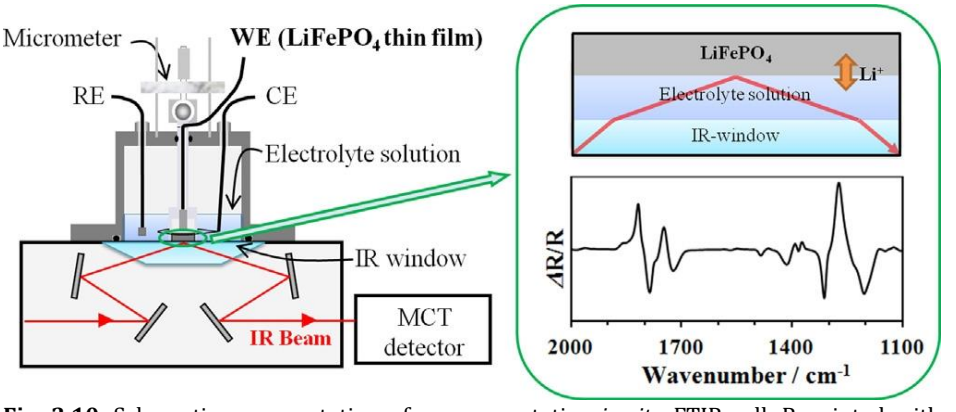

Fig. 3.10. Schematic representation of a representative *in-situ* FTIR cell. Reprinted with permission from ref. [71]. Copyright © 2013 Elsevier B.V.

3.5.3. Optical microscopy

The resolution of optical microscopy is fundamentally restricted by the diffraction limit of visible light, which is not sufficient to monitor microstructural changes. However electrochemically induced macroscopic structural changes of electrodes and dendritic lithium formation can be investigated through (digital) optical microscopy. Since the color of lithiated graphite is a measure of its SoC [73], the (de)lithiation process of graphite can be studied with an optical microscope by tracking the color evolution.

This technique does not put many restrictions on the design of *in situ* cells and many different cells have therefore been described in the literature. The only requirement is the presence of a glass window that allows the exposure of the electrodes to visible light.

3.5.4. Multi-beam optical stress sensor

The multi-beam optical stress sensor technique (MOSS) is a method to determine the stress in thin films by measuring the change in substrate curvature. This is done by employing an array of parallel laser beams and measuring the relative change in the spacing between them as they are reflected from the substrate. The electrochemically induced stress/strain during battery operation in thin film electrodes can, in this way, be monitored.

A typical *in situ* MOSS cell has the characteristics of a flooded beaker cell, comprising of a lithium foil, acting as a counter electrode positioned at the bottom of the cell, covered by a separator immersed by the electrolyte and the substrate containing the thin film electrode material. The substrate on which the electrode layer has been deposited is placed in the electrochemical cell such that the electrode-side faces the separator. The incorporation of a glass window allows optical access to the back of the substrate. Unlike most battery setups no pressure is applied to this system [74]. The array of laser beams applied to measure the curvature are reflected at the back of the substrate. It is essential that the used

substrates can deform elastically so that the induced stress in the thin film electrode is proportional to the measured substrate curvature. Barrier layers are deposited onto the substrate when necessary to isolate it from electrochemical reactions.

3.6. Magnetic resonance techniques

3.6.1. Nuclear magnetic resonance spectroscopy

Nuclear magnetic resonance spectroscopy (NMR) is based on the magnetic resonance properties of nuclear isotopes, which, depending on their nuclear spin and quadrupole moments, resonate at characteristic frequencies when placed in a strong static magnetic field. The nuclear magnetic resonance spectra are probed by additionally applying appropriate radio frequency (rf) magnetic field pulses at the resonance frequency. Slight variations in the observed resonance frequencies give detailed information about the local electronic environment around the nucleus. The local electronic environment of ^{7}Li (and ^{6}Li) can adequately be probed by NMR and, consequently, yields information about the Li environment and electrochemically induced structural changes of electrodes during or after cycling.
The metal parts normally present in a battery, such as casings, current collectors and metallic coatings in coffee-bag cells, shield the electrodes from the applied pulsed rf-fields. The batteries used for *in situ* measurements must therefore have as few metallic parts as possible. To this end Bellcore-type plastic cells have been successfully employed [75]. A common problem with plastic batteries is the lack of pressure across the cell. However, in this type of cell the components are laminated together through a process that involves heating under pressure and the addition of a binder, and they are therefore sufficiently coherent and stay attached. The cell furthermore comprises of a current collector mesh rather than a closed foil to limit the rf shielding effects [76]. Unlike batteries with a metal casing, plastic cells are permeable to air and relatively fragile. As an alternative a more robust cylindrical cell has been designed by Poli and colleagues [77].

^{7}Li NMR has shown to be an adequate technique to investigate anode materials. An elaborate overview has been provided by Blanc *et al*. [78]. However, recently researchers have shifted their interest to *in situ* NMR studies of cathode materials. This is quite challenging due to the signal broadening and peak shifting, which results from the paramagnetic nature of most cathode materials and the inability to use *in situ* magic angle spinning to overcome these limitations [79]. Detailed practical aspects associated with *in situ* NMR measurements of cathode materials are discussed in detail for $Li_{1.08}Mn_{1.92}O_4$ [76, 79]. Shimoda and co-workers [80] were able to observe the lithium extraction/insertion from/in $LiCoO_2$ by optimization of the cell components and increasing the magnetic field strength.
NMR is a quantitative method, but it yet remains challenging to obtain spatially resolved measurements. Recently, however, several *in situ* NMR studies have been conducted, measuring Li-ion concentration gradients [81, 82] and monitoring lithium dendrite formation [83]. Klett *et al*. [81] employed a 10 mm cylindrical cell to study the concentration gradient build up in $LiPF_6$ electrolyte under current flowing conditions. The 1D lithium distribution could be obtained with a nominal resolution of 19 μm. From the measured data, the authors quantified the salt diffusivity and the Li^+ transport number on the basis of a physical mass transport model. Krachkovskiy and colleagues [82] applied 1D ^{7}Li NMR imaging in

combination with slice-selective NMR to measure the Li^+ self-diffusion coefficients in liquid electrolytes.

Bhattacharyya *et al*. [83] were able to quantify the mass of moss/dendrite lithium microstructures formed during electrochemical cycling of a metallic Li electrode. Due to the skin effect, the applied rf-field penetrates the subsurface region only and the signal was therefore found to be proportional to the area of the metal electrode rather than its volume. This is, however, different for the microstructures formed upon cycling, which are totally penetrated by the magnetic field due to their limited size, resulting in a response which is directly proportional to their volume or mass. With the assumption that during cycling the total surface area of the bulk metal electrode was not changing significantly, the change in signal intensity was attributed to the amount of Li microstructures formed or stripped. Several different electrolytes were employed, resulting in different electrode behavior, which could be readily observed.

By applying NMR in the way discussed above, Chandrashekar *et al*. [84] measured the amount of deposited Li-microstructures during electrochemical cycling in a symmetric lithium cell. However, to determine the location of the lithium deposits, magnetic resonance imaging (MRI) was employed to obtain a three dimensional image (**Fig. 3.11**). The obtained spatial resolution is of the order of hundreds of μm. Tang *et al*. [85] applied stray-field imaging, which makes use of a magnetic field with higher field gradients than that used for MRI to monitor the Li-ion transfer between the electrodes in Li-graphite and Li-$LiFePO_4$ half-cells, obtaining a 1D distribution with a resolution of 39 μm.

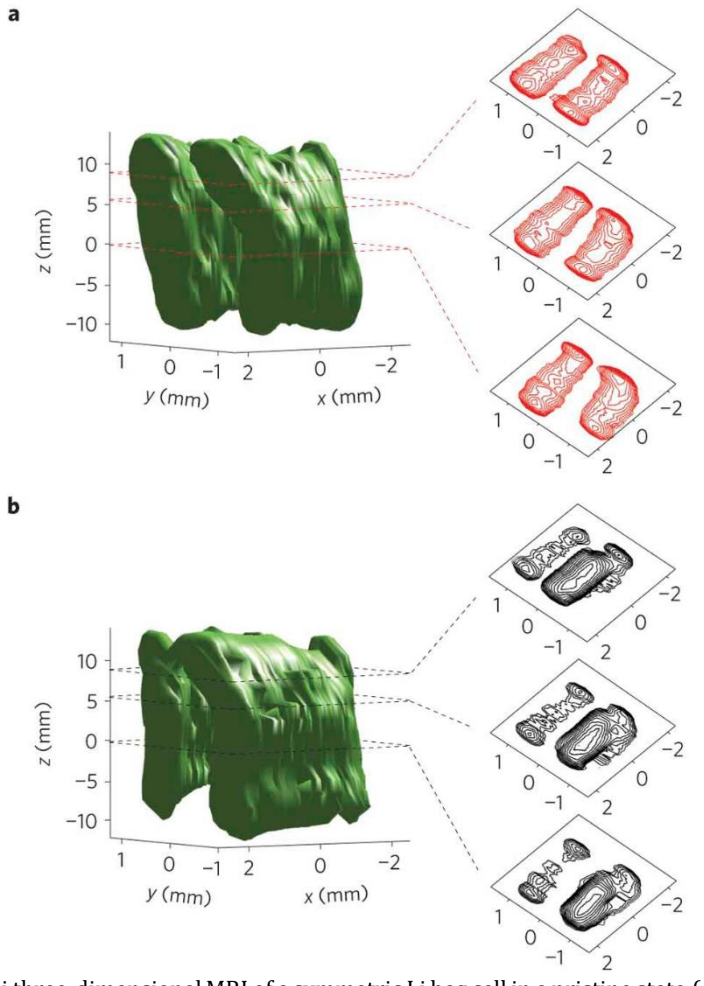

Fig. 3.11. ^{7}Li three-dimensional MRI of a symmetric Li bag cell in a pristine state (a) and after charging (b). In each panel horizontal cross-sections, perpendicular to the *z* direction, are included. Reprinted by permission from Macmillan Publishers Ltd: Nature Materials ref. [84], copyright (2012).

3.6.2. Mössbauer spectroscopy

Mössbauer spectroscopy (MS) is a nuclear hyperfine interaction method, which enables one to study the influence of the electronic environment on the nuclear hyperfine energy levels, and as such probes the structure of materials. The parameters probed are typically the Isomer Shift and Quadrupole Interaction that give information about the valence state and electronic configuration of the Mossbauer atom, as well as a magnetic hyperfine field (when present). In a typical experiment the intensity of the transmitted radiation is measured as a function of the Mössbauer source velocity. The specific requirements for a suitable gamma ray source limit the different isotopes that can be studied by this technique. Although

theoretically several Isotopes relevant for Li-ion batteries can be investigated by MS, most research has been restricted to ^{57}Fe and ^{119}Sn Mössbauer experiments.

The gamma ray energies are generally higher than typical XRD X-ray energies. For that reason electrochemical cells for *in situ* MS research are very similar to *in situ* XRD and XAS setups since the gamma rays can penetrate the cells and window configurations. For example, the specially designed cell by Leriche *et al*. [86] for *operando* studies of Li-ion batteries using synchrotron radiation, has been applied for *operando* MS experiments in combination with X-ray based techniques [87, 88]. A simpler, yet similar, design [89] used for *in situ* MS measurements is a coin-type cell equipped with a Be window in the cell cap and case. The Be window is transparent to γ-rays and also acts as a current collector. When in contact with a cathode material a layer of Al is, however, required to prevent the Be window from oxidation [86].

3.7. Neutron-based techniques

3.7.1. Neutron Diffraction

The technique of neutron diffraction is very similar to XRD. However, the technique can be used in addition to XRD, especially to study light elements such as lithium, as neutrons interact with the nucleus and its cross section rather than with the electrons surrounding the atom as is the case for X-rays [90]. Since the neutron cross section has similar but varying sizes for light and heavy isotopes throughout the periodic system, neutrons are sensitive to light elements (*e.g.* Li) next to heavier ones (*e.g.* Fe, Co), but can also be sensitive to the contrast between elements of almost the same mass (*e.g.* Ni and Mn).

Another difference is the weaker interaction of neutrons with matter and the resulting larger penetration depth. Consequently, a relatively high amount of electrode material is necessary for a proper measurement, which can be challenging for laboratory-scale batteries [91, 92]. However, due to this large penetration depth of the neutrons, measurements can be performed on unmodified commercial cells and diffraction patterns of the anode and cathode can be obtained simultaneously [93]. These batteries, however, are not optimized for *in situ* neutron diffraction. For instance, the technique is very sensitive to the hydrogen present in the separators and liquid electrolytes of commercial cells, which unfortunately gives rise to large background signals from incoherently scattered neutrons [94-96]. The use of custom-made cells with low H-content components that mimic, for example, cylindrical 18650-type commercial batteries leads to a significant increase of the signal-to-noise ratio [90]. A common strategy to lower the H-content is the use of deuterated electrolytes and special fluorinated separators [90, 97, 98]. A remaining issue is however the presence of many cell components in the pathway of the neutron beam. This results in additional undesired Bragg reflections and increased background intensity [91]. Also the different electrochemical equilibrium phases that are generally present lead to overlapping spectra of anode and cathode. At this moment in time it remains challenging to obtain high-quality full pattern Rietveld refinements of *in situ* neutron diffraction data [92]. In an effort to resolve the aforementioned issues, several promising new battery cells for *in situ* neutron diffraction measurements have recently been proposed [91, 92, 95, 97, 99].

3.7.2. Neutron reflectometry

Neutron reflectometry or scattering involves directing a highly collimated beam of neutrons onto a surface and measuring the intensity of the reflected radiation as a function of angle or neutron wavelength. It is used to determine the scattering length density as a function of penetration depth which, in turn, is related to the atomic composition. This allows monitoring of thin film growth, such as SEI formation, and volumetric changes induced by battery operation.

Due to the large penetration depth of the neutrons, commercial cylindrical batteries and conventional coin cells can be used for *in situ* reflectometry research. To prevent loss of intensity, isotopically enriched ^{7}Li electrodes can be applied, as ^{6}Li species are able to absorb neutrons [100]. To investigate thin films electrodes, custom-made electrochemical cells are used [101, 102]. These cells allow the substrate, onto which the electrode of interest has been deposited, to be mounted. The substrate is the incoming medium for the neutrons.

3.7.3. Neutron depth profiling

With neutron depth profiling (NDP) one is able to probe the ^{6}Li isotope as a function of sample depth. The sample is bombarded with moderated thermal (low energy) neutrons of about 25 meV, which can be absorbed by ^{6}Li that has a high neutron absorption cross section, resulting in the emission of an alpha and triton particle, according to

$$^{6}\mathrm{Li} + \mathrm{n} \rightarrow \alpha\ (2056.12\ \mathrm{keV}) + {}^{3}\mathrm{H}\ (2727.88\ \mathrm{keV})$$

The technique is considered non-destructive, since the amount of annihilated ^{6}Li atoms is negligible with respect to the total amount of Li atoms. Upon creation the alpha and triton particles have a well-defined energy. By measuring the energy loss of these particles when the detector is reached, the depth at which these were initially formed can be deduced. In order to obtain an accurate lithium depth profile the energy loss must only result from the interaction of the charged particles with the sample and not with gaseous species on the way to the detector. This implies that the measurements preferably must take place at sub-ambient pressures. As two different particles are emitted from the sample, two depth profiles can be obtained. The alpha particles with 2+ charge typically lose more energy while crossing the sample and can therefore be used to obtain a high resolution concentration profile of thin film batteries. The (1D) resolution can be as low as 72 nm for metal oxide cathodes [103]. To measure concentration profiles of bigger batteries the ^{3}H particles can alternatively be used.

Even though neutrons have a high penetration power, the created alpha and tritons particles are strongly absorbed by metal. Therefore, the thickness of the current collector of an *in situ* NDP cell must be kept as small as possible, and no metallic casing can be applied. The cell furthermore must be operational under vacuum conditions. However, in an exploratory study of Nagpure and co-workers [104] it has been shown that by the application of an inert helium atmosphere, measurements of (air-sensitive) materials are also possible at relatively high pressures.

Oudenhoven *et al*. [105] were the first to use *in situ* NDP to investigate Li-ion batteries. The study shows that NDP is a powerful method to probe the lithium concentration throughout a thin film battery. To achieve a better noise-to-signal ratio the measurements were conducted on a ^{6}Li enriched battery, as natural lithium consists of only 7.5% ^{6}Li. Recently Liu *et al*. [106] applied the technique to perform quantitative measurements on liquid electrolyte batteries. The used coin cell featured a Kapton window in the top casing to allow the ^{3}H particles to reach the detector. Because the study concerned the lithium concentration in a tin anode during battery operation the current collector could be omitted.

3.8. Outlook

The application of *in situ* methods to investigate battery materials plays an important role in the fundamental understanding of the operation of Li-ion batteries. Major developments have taken place in the recent years, most importantly the development of techniques that enable spatially resolved measurements such as *in situ* TEM and *in situ* X-ray tomography. The local probes enable detailed insight at the single crystallite level which can be compared to the full battery overall characteristics.

Obviously, with several techniques still in the early development stage, there is significant room to improve the current *in situ* methods for Li-ion battery research. In particular techniques that are capable of providing information on the 3D morphology of electrodes as well as the chemical composition have shown to be extremely insightful [28, 41, 83, 84] and further development is therefore expected. Furthermore, *operando* measurements, probing the non-equilibrium states, require a high data collection rate, which is presently challenging for several *in situ* tools.

A crucial part of *in situ* research is the design of electrochemical setups that are compatible with the applied technique. Researchers should be mindful of the extent to which these custom-made cells relate to practical batteries and be cautious of artefacts. Obviously the combined use of multiple *in situ* techniques is very powerful and can give increased overall insights. For certain methods this can be achieved with relative ease due to the large similarities in design of their respective *in situ* cells. Examples of such combinations are: Raman and FTIR [65], XRD and XAS [21], XAS and MS [19], and neutron diffraction together with neutron scattering [107]. Given the recent progress it can be expected that *in situ* research will become increasingly important in the development of future generations of Li-ion batteries.

References

[1] M. Shao, Journal of Power Sources, 270 (2014) 475-498.
[2] S. Ramdon, B. Bhushan, S.C. Nagpure, Journal of Power Sources, 249 (2014) 373-384.
[3] X.H. Liu, J.Y. Huang, Energy & Environmental Science, 4 (2011) 3844-3860.
[4] E.S. Takeuchi, A.C. Marschilok, K.J. Takeuchi, A. Ignatov, Z. Zhong, M. Croft, Energy & Environmental Science, 6 (2013) 1465-1470.
[5] M.R. Roberts, A. Madsen, C. Nicklin, J. Rawle, M.G. Palmer, J.R. Owen, A.L. Hector, Journal of Physical Chemistry C, 118 (2014) 6548-6557.
[6] C.R. Fell, M. Chi, Y.S. Meng, J.L. Jones, Solid State Ionics, 207 (2012) 44-49.
[7] J.S. Thorne, J.R. Dahn, M.N. Obrovac, R.A. Dunlap, Journal of the Electrochemical Society, 158 (2011) A1328-A1334.
[8] H.T. Zhou, M.A. Einarsrud, F. Vullum-Bruer, Journal of Power Sources, 238 (2013) 478-484.
[9] C. Villevieille, T. Sasaki, P. Novak, Rsc Advances, 4 (2014) 6782-6789.
[10] B.E. Wilson, W.H. Smyrl, A. Stein, Journal of the Electrochemical Society, 161 (2014) A700-A703.
[11] C.K. Lin, Y. Ren, K. Amine, Y. Qin, Z.H. Chen, Journal of Power Sources, 230 (2013) 32-37.
[12] S. Misra, N. Liu, J. Nelson, S.S. Hong, Y. Cui, M.F. Toney, Acs Nano, 6 (2012) 5465-5473.
[13] H. He, C. Huang, C.W. Luo, J.J. Liu, Z.S. Chao, Electrochimica Acta, 92 (2013) 148-152.
[14] W.R. Brant, S. Schmid, G.D. Du, Q.F. Gu, N. Sharma, Journal of Power Sources, 244 (2013) 109-114.
[15] M.A. Lowe, J. Gao, H.D. Abruna, Journal of Materials Chemistry A, 1 (2013) 2094-2103.
[16] D.P. Lv, J.Y. Bai, P. Zhang, S.Q. Wu, Y.X. Li, W. Wen, Z. Jiang, J.X. Mi, Z.Z. Zhu, Y. Yang, Chemistry of Materials, 25 (2013) 2014-2020.
[17] J. Wang, Y.-c.K. Chen-Wiegart, J. Wang, Chemical Communications, 49 (2013) 6480-6482.
[18] A. Ito, Y. Sato, T. Sanada, M. Hatano, H. Horie, Y. Ohsawa, Journal of Power Sources, 196 (2011) 6828-6834.
[19] R. Dominko, I. Arcon, A. Kodre, D. Hanzel, M. Gaberscek, Journal of Power Sources, 189 (2009) 51-58.
[20] M. Balasubramanian, X. Sun, X.Q. Yang, J. McBreen, Journal of Power Sources, 92 (2001) 1-8.
[21] Y.Y. Hu, Z.G. Liu, K.W. Nam, O.J. Borkiewicz, J. Cheng, X. Hua, M.T. Dunstan, X.Q. Yu, K.M. Wiaderek, L.S. Du, K.W. Chapman, P.J. Chupas, X.Q. Yang, C.P. Grey, Nature Materials, 12 (2013) 1130-1136.
[22] K. Yamamoto, T. Minato, S. Mori, D. Takamatsu, Y. Orikasa, H. Tanida, K. Nakanishi, H. Murayama, T. Masese, T. Mori, H. Arai, Y. Koyama, Z. Ogumi, Y. Uchimoto, The Journal of Physical Chemistry C, 118 (2014) 9538-9543.
[23] X.S. Liu, D.D. Wang, G. Liu, V. Srinivasan, Z. Liu, Z. Hussain, W.L. Yang, Nature Communications, 4 (2013) 2568.
[24] R. Malik, F. Zhou, G. Ceder, Nature Materials, 10 (2011) 587-590.
[25] C.W. Hu, N. Sharma, C.Y. Chiang, H.C. Su, V.K. Peterson, H.W. Hsieh, Y.F. Lin, W.C. Chou, B.Y. Shew, C.H. Lee, Journal of Power Sources, 244 (2013) 158-163.
[26] S.C. Chao, Y.C. Yen, Y.F. Song, Y.M. Chen, H.C. Wu, N.L. Wu, Electrochemistry Communications, 12 (2010) 234-237.
[27] J.J. Wang, Y.C.K. Chen-Wiegart, J. Wang, Nature Communications, 5 (2014) 4570.
[28] M. Ebner, F. Marone, M. Stampanoni, V. Wood, Science, 342 (2013) 716-720.
[29] J. Wang, Y.-c.K. Chen-Wiegart, J. Wang, Angewandte Chemie International Edition, 53 (2014) 4460-4464.
[30] J.N. Weker, N. Liu, S. Misra, J.C. Andrews, Y. Cui, M.F. Toney, Energy & Environmental Science, 7 (2014) 2771-2777.

[31] Q.P. McAllister, K.E. Strawhecker, C.R. Becker, C.A. Lundgren, Journal of Power Sources, 257 (2014) 380-387.
[32] J. Zhu, K.Y. Zeng, L. Lu, Journal of Applied Physics, 111 (2012) 063723.
[33] J. Zhu, J.K. Feng, L. Lu, K.Y. Zeng, Journal of Power Sources, 197 (2012) 224-230.
[34] D.E. Demirocak, B. Bhushan, Journal of Colloid and Interface Science, 423 (2014) 151-157.
[35] J. Park, S. Kalnaus, S. Han, Y.K. Lee, G.B. Less, N.J. Dudney, C. Daniel, A.M. Sastry, Journal of Power Sources, 222 (2013) 417-425.
[36] N. Balke, S. Jesse, Y. Kim, L. Adamczyk, I.N. Ivanov, N.J. Dudney, S.V. Kalinin, Acs Nano, 4 (2010) 7349-7357.
[37] A.L. Lipson, R.S. Ginder, M.C. Hersam, Advanced Materials, 23 (2011) 5613.
[38] S.T. Boles, A. Sedlmayr, O. Kraft, R. Moenig, Applied Physics Letters, 100 (2012) 243901.
[39] D. Chen, S. Indris, M. Schulz, B. Gamer, R. Monig, Journal of Power Sources, 196 (2011) 6382-6387.
[40] D.J. Miller, C. Proff, J.G. Wen, D.P. Abraham, J. Bareno, Advanced Energy Materials, 3 (2013) 1098-1103.
[41] J.Y. Huang, L. Zhong, C.M. Wang, J.P. Sullivan, W. Xu, L.Q. Zhang, S.X. Mao, N.S. Hudak, X.H. Liu, A. Subramanian, H. Fan, L. Qi, A. Kushima, J. Li, Science, 330 (2010) 1515-1520.
[42] X.H. Liu, Y. Liu, A. Kushima, S. Zhang, T. Zhu, J. Li, J.Y. Huang, Advanced Energy Materials, 2 (2012) 722-741.
[43] M.R. Zamfir, H.T. Nguyen, E. Moyen, Y.H. Lee, D. Pribat, Journal of Materials Chemistry A, 1 (2013) 9566-9586.
[44] C.-M. Wang, Journal of Materials Research, 30 (2015) 326-339.
[45] Y.M. Chiang, Science, 330 (2010) 1485-1486.
[46] F. Lin, I.M. Markus, M.M. Doeff, H.L.L. Xin, Scientific Reports, 4 (2014) 5694.
[47] L. Zhong, X.H. Liu, G.F. Wang, S.X. Mao, J.Y. Huang, Physical Review Letters, 106 (2011) 248302.
[48] M. Gu, L.R. Parent, B.L. Mehdi, R.R. Unocic, M.T. McDowell, R.L. Sacci, W. Xu, J.G. Connell, P.H. Xu, P. Abellan, X.L. Chen, Y.H. Zhang, D.E. Perea, J.E. Evans, L.J. Lauhon, J.G. Zhang, J. Liu, N.D. Browning, Y. Cui, I. Arslan, C.M. Wang, Nano Letters, 13 (2013) 6106-6112.
[49] K.W. Noh, S.J. Dillon, Scripta Materialia, 69 (2013) 658-661.
[50] X.H. Liu, L.Q. Zhang, L. Zhong, Y. Liu, H. Zheng, J.W. Wang, J.-H. Cho, S.A. Dayeh, S.T. Picraux, J.P. Sullivan, S.X. Mao, Z.Z. Ye, J.Y. Huang, Nano Letters, 11 (2011) 2251-2258.
[51] M.E. Holtz, Y.C. Yu, D. Gunceler, J. Gao, R. Sundararaman, K.A. Schwarz, T.A. Arias, H.D. Abruna, D.A. Muller, Nano Letters, 14 (2014) 1453-1459.
[52] Y. Liu, N.S. Hudak, D.L. Huber, S.J. Limmer, J.P. Sullivan, J.Y. Huang, Nano Letters, 11 (2011) 4188-4194.
[53] A.L. Lipson, K. Puntambekar, D.J. Comstock, X.B. Meng, M.L. Geier, J.W. Elam, M.C. Hersam, Chemistry of Materials, 26 (2014) 935-940.
[54] Y. He, D.M. Piper, M. Gu, J.J. Travis, S.M. George, S.H. Lee, A. Genc, L. Pullan, J. Liu, S.X. Mao, J.G. Zhang, C.M. Ban, C.M. Wang, Acs Nano, 8 (2014) 11816-11823.
[55] D. Ruzmetov, V.P. Oleshko, P.M. Haney, H.J. Lezec, K. Karki, K.H. Baloch, A.K. Agrawal, A.V. Davydov, S. Krylyuk, Y. Liu, J.Y. Huang, M. Tanase, J. Cumings, A.A. Talin, Nano Letters, 12 (2012) 505-511.
[56] H. Lichte, M. Lehmann, Reports on Progress in Physics, 71 (2008) 016102.
[57] K. Yamamoto, T. Hirayama, T. Tanji, Microscopy, 62 (2013) S29-S41.
[58] K. Yamamoto, Y. Iriyama, T. Asaka, T. Hirayama, H. Fujita, C.A.J. Fisher, K. Nonaka, Y. Sugita, Z. Ogumi, Angewandte Chemie-International Edition, 49 (2010) 4414-4417.
[59] J.B. Bates, N.J. Dudney, B. Neudecker, A. Ueda, C.D. Evans, Solid State Ionics, 135 (2000) 33-45.
[60] K. Yamamoto, Y. Iriyama, T. Asaka, T. Hirayama, H. Fujita, K. Nonaka, K. Miyahara, Y. Sugita, Z. Ogumi, Electrochemistry Communications, 20 (2012) 113-116.

[61] V. Stancovski, S. Badilescu, Journal of Applied Electrochemistry, 44 (2014) 23-43.
[62] T. Gross, L. Giebeler, C. Hess, Review of Scientific Instruments, 84 (2013) 073109.
[63] P. Lanz, C. Villevieille, P. Novak, Electrochimica Acta, 109 (2013) 426-432.
[64] J. Wu, G.K.P. Dathar, C.W. Sun, M.G. Theivanayagam, D. Applestone, A.G. Dylla, A. Manthiram, G. Henkelman, J.B. Goodenough, K.J. Stevenson, Nanotechnology, 24 (2013) 9.
[65] S. Perez-Villar, P. Lanz, H. Schneider, P. Novak, Electrochimica Acta, 106 (2013) 506-515.
[66] H. Nakagawa, Y. Domi, T. Doi, M. Ochida, S. Tsubouchi, T. Yamanaka, T. Abe, Z. Ogumi, Journal of Power Sources, 206 (2012) 320-324.
[67] S. Hy, Felix, Y.H. Chen, J.Y. Liu, J. Rick, B.J. Hwang, Journal of Power Sources, 256 (2014) 324-328.
[68] P. Lanz, P. Novak, Journal of the Electrochemical Society, 161 (2014) A1555-A1563.
[69] B.R. Long, M.K.Y. Chan, J.P. Greeley, A.A. Gewirth, Journal of Physical Chemistry C, 115 (2011) 18916-18921.
[70] R. Sharabi, E. Markevich, V. Borgel, G. Salitra, D. Aurbach, G. Semrau, M.A. Schmidt, Electrochemical and Solid State Letters, 13 (2010) A32-A35.
[71] Y. Akita, M. Segawa, H. Munakata, K. Kanamura, Journal of Power Sources, 239 (2013) 175-180.
[72] K. Hongyou, T. Hattori, Y. Nagai, T. Tanaka, H. Nii, K. Shoda, Journal of Power Sources, 243 (2013) 72-77.
[73] P. Maire, H. Kaiser, W. Scheifele, P. Novak, Journal of Electroanalytical Chemistry, 644 (2010) 127-131.
[74] V.A. Sethuraman, A. Nguyen, M.J. Chon, S.P.V. Nadimpalli, H. Wang, D.P. Abraham, A.F. Bower, V.B. Shenoy, P.R. Guduru, Journal of the Electrochemical Society, 160 (2013) A739-A746.
[75] F. Chevallier, M. Letellier, M. Morcrette, J.M. Tarascon, E. Frackowiak, J.N. Rouzaud, F. Beguin, Electrochemical and Solid State Letters, 6 (2003) A225-A228.
[76] N.M. Trease, L.N. Zhou, H.J. Chang, B.Y.X. Zhu, C.P. Grey, Solid State Nuclear Magnetic Resonance, 42 (2012) 62-70.
[77] F. Poli, J.S. Kshetrimayum, L. Monconduit, M. Letellier, Electrochemistry Communications, 13 (2011) 1293-1295.
[78] F. Blanc, M. Leskes, C.P. Grey, Accounts of chemical research, 46 (2013) 1952-1963.
[79] L.N. Zhou, M. Leskes, A.J. Ilott, N.M. Trease, C.P. Grey, Journal of Magnetic Resonance, 234 (2013) 44-57.
[80] K. Shimoda, M. Murakami, D. Takamatsu, H. Arai, Y. Uchimoto, Z. Ogumi, Electrochimica Acta, 108 (2013) 343-349.
[81] M. Klett, M. Giesecke, A. Nyman, F. Hallberg, R.W. Lindstrom, G. Lindbergh, I. Furo, Journal of the American Chemical Society, 134 (2012) 14654-14657.
[82] S.A. Krachkoyskiy, A.D. Pauric, I.C. Halalay, G.R. Goward, Journal of Physical Chemistry Letters, 4 (2013) 3940-3944.
[83] R. Bhattacharyya, B. Key, H.L. Chen, A.S. Best, A.F. Hollenkamp, C.P. Grey, Nature Materials, 9 (2010) 504-510.
[84] S. Chandrashekar, N.M. Trease, H.J. Chang, L.S. Du, C.P. Grey, A. Jerschow, Nature Materials, 11 (2012) 311-315.
[85] J.A. Tang, S. Dugar, G.M. Zhong, N.S. Dalal, J.P. Zheng, Y. Yang, R.Q. Fu, Scientific Reports, 3 (2013) 2596.
[86] J.B. Leriche, S. Hamelet, J. Shu, M. Morcrette, C. Masquelier, G. Ouvrard, M. Zerrouki, P. Soudan, S. Belin, E. Elkaim, F. Baudelet, Journal of the Electrochemical Society, 157 (2010) A606-A610.
[87] A. Perea, M.T. Sougrati, C.M. Ionica-Bousquet, B. Fraisse, C. Tessier, L. Aldon, J.C. Jumas, Rsc Advances, 2 (2012) 9517-9524.

[88] D.E. Conte, M. Mouyane, L. Stievano, B. Fraisse, M.T. Sougrati, J. Olivier-Fourcade, P. Willmann, C. Jordy, M. Artus, S. Cassaignon, K. Driezen, J.C. Jumas, Journal of Solid State Electrochemistry, 16 (2012) 3837-3848.
[89] J. Li, A. Smith, R.J. Sanderson, T.D. Hatchard, R.A. Dunlap, J.R. Dahn, Journal of the Electrochemical Society, 156 (2009) A283-A288.
[90] N. Sharma, V.K. Peterson, Journal of Solid State Electrochemistry, 16 (2012) 1849-1856.
[91] V.A. Godbole, M. Hess, C. Villevieille, H. Kaiser, J.F. Colin, P. Novak, Rsc Advances, 3 (2013) 757-763.
[92] M. Bianchini, J.B. Leriche, J.L. Laborier, L. Gendrin, E. Suard, L. Croguennec, C. Masquelier, Journal of the Electrochemical Society, 160 (2013) A2176-A2183.
[93] N. Sharma, V.K. Peterson, M.M. Elcombe, M. Avdeev, A.J. Studer, N. Blagojevic, R. Yusoff, N. Kamarulzaman, Journal of Power Sources, 195 (2010) 8258-8266.
[94] N. Sharma, V.K. Peterson, Electrochimica Acta, 101 (2013) 79-85.
[95] H.D. Liu, C.R. Fell, K. An, L. Cai, Y.S. Meng, Journal of Power Sources, 240 (2013) 772-778.
[96] O. Dolotko, A. Senyshyn, M.J. Muhlbauer, K. Nikolowski, H. Ehrenberg, Journal of Power Sources, 255 (2014) 197-203.
[97] M. Roberts, J.J. Biendicho, S. Hull, P. Beran, T. Gustafsson, G. Svensson, K. Edstrom, Journal of Power Sources, 226 (2013) 249-255.
[98] W.K. Pang, V.K. Peterson, N. Sharma, J.J. Shiu, S.H. Wu, Chemistry of Materials, 26 (2014) 2318-2326.
[99] B. Vadlamani, K. An, M. Jagannathan, K.S.R. Chandran, Journal of the Electrochemical Society, 161 (2014) A1731-A1741.
[100] C.A. Bridges, X.-G. Sun, J. Zhao, M.P. Paranthaman, S. Dai, Journal of Physical Chemistry C, 116 (2012) 7701-7711.
[101] B. Jerliu, L. Dorrer, E. Huger, G. Borchardt, R. Steitz, U. Geckle, V. Oberst, M. Bruns, O. Schneider, H. Schmidt, Physical Chemistry Chemical Physics, 15 (2013) 7777-7784.
[102] J.F. Browning, L. Baggetto, K.L. Jungjohann, Y. Wang, W.E. Tenhaeff, J.K. Keum, D.L. Wood, G.M. Veith, Acs Applied Materials & Interfaces, 6 (2014) 18569-18576.
[103] S. Whitney, S.R. Biegalski, Y.H. Huang, J.B. Goodenough, Journal of the Electrochemical Society, 156 (2009) A886-A890.
[104] S.C. Nagpure, P. Mulligan, M. Canova, L.R. Cao, Journal of Power Sources, 248 (2014) 489-497.
[105] J.F.M. Oudenhoven, F. Labohm, M. Mulder, R.A.H. Niessen, F.M. Mulder, P.H.L. Notten, Advanced Materials, 23 (2011) 4103.
[106] D.X. Liu, J.H. Wang, K. Pan, J. Qiu, M. Canova, L.R. Cao, A.C. Co, Angewandte Chemie-International Edition, 53 (2014) 9498-9502.
[107] A. Senyshyn, M.J. Muhlbauer, K. Nikolowski, T. Pirling, H. Ehrenberg, Journal of Power Sources, 203 (2012) 126-129.
[108] K.C. Kirshenbaum, D.C. Bock, Z. Zhong, A.C. Marschilok, K.J. Takeuchi, E.S. Takeuchi, Physical Chemistry Chemical Physics, 16 (2014) 9138-9147.
[109] K. Kirshenbaum, D.C. Bock, C.-Y. Lee, Z. Zhong, K.J. Takeuchi, A.C. Marschilok, E.S. Takeuchi, Science, 347 (2015) 149-154.
[110] X. Hua, R. Robert, L.S. Du, K.M. Wiaderek, M. Leskes, K.W. Chapman, P.J. Chupas, C.P. Grey, Journal of Physical Chemistry C, 118 (2014) 15169-15184.
[111] L. Baggetto, P.H.L. Notten, Journal of the Electrochemical Society, 156 (2009) A169-A175.
[112] C.W. Hu, T.Y. Chen, K.S. Shih, P.J. Wu, H.C. Su, C.Y. Chiang, A.F. Huang, H.W. Hsieh, C.C. Chang, B.Y. Shew, C.H. Lee, Journal of Power Sources, 270 (2014) 449-456.
[113] Q. Liu, H. He, Z.F. Li, Y.D. Liu, Y. Ren, W.Q. Lu, J. Lu, E.A. Stach, J. Xie, Acs Applied Materials & Interfaces, 6 (2014) 3282-3289.
[114] D. Mohanty, S. Kalnaus, R.A. Meisner, K.J. Rhodes, J.L. Li, E.A. Payzant, D.L. Wood, C. Daniel, Journal of Power Sources, 229 (2013) 239-248.

[115] F.C. Strobridge, R.J. Clement, M. Leskes, D.S. Middlemiss, O.J. Borkiewicz, K.M. Wiaderek, K.W. Chapman, P.J. Chupas, C.P. Grey, Chemistry of Materials, 26 (2014) 6193-6205.
[116] M. Hirayama, H. Ido, K. Kim, W. Cho, K. Tamura, J.i. Mizuki, R. Kanno, Journal of the American Chemical Society, 132 (2010) 15268-15276.
[117] C.H. Shen, L. Huang, Z. Lin, S.Y. Shen, Q. Wang, H. Su, F. Fu, X.M. Zheng, Acs Applied Materials & Interfaces, 6 (2014) 13271-13279.
[118] A. Singer, A. Ulvestad, H.M. Cho, J.W. Kim, J. Maser, R. Harder, Y.S. Meng, O.G. Shpyrko, Nano Letters, 14 (2014) 5295-5300.
[119] A. Ulvestad, A. Singer, H.M. Cho, J.N. Clark, R. Harder, J. Maser, Y.S. Meng, O.G. Shpyrko, Nano Letters, 14 (2014) 5123-5127.
[120] W. Zhu, D. Liu, J. Trottier, C. Gagnon, A. Mauger, C.M. Julien, K. Zaghib, Journal of Power Sources, 242 (2013) 236-243.
[121] W. Zhu, D. Liu, J. Trottier, C. Gagnon, A. Guerfi, C.M. Julien, A. Mauger, K. Zaghib, Journal of Power Sources, 264 (2014) 290-298.
[122] K. Sakamoto, M. Hirayama, N. Sonoyama, D. Mori, A. Yamada, K. Tamura, J. Mizuki, R. Kanno, Chemistry of Materials, 21 (2009) 2632-2640.
[123] C.H. Shen, Q. Wang, F. Fu, L. Huang, Z. Lin, S.Y. Shen, H. Su, X.M. Zheng, B.B. Xu, J.T. Li, S.G. Sun, Acs Applied Materials & Interfaces, 6 (2014) 5516-5524.
[124] H. Arai, K. Sato, Y. Orikasa, H. Murayama, I. Takahashi, Y. Koyama, Y. Uchimoto, Z. Ogumi, Journal of Materials Chemistry A, 1 (2013) 10442-10449.
[125] S. Taminato, M. Hirayama, K. Suzuki, K. Kim, Y.M. Zheng, K. Tamura, J. Mizuki, R. Kanno, Journal of Materials Chemistry A, 2 (2014) 17875-17882.
[126] W.K. Pang, V.K. Peterson, N. Sharma, C.F. Zhang, Z.P. Guo, Journal of Physical Chemistry C, 118 (2014) 3976-3983.
[127] F. Wang, L.J. Wu, B. Key, X.Q. Yang, C.P. Grey, Y.M. Zhu, J. Graetz, Advanced Energy Materials, 3 (2013) 1324-1331.
[128] K.J. Rhodes, R. Meisner, M. Kirkham, N. Dudney, C. Daniel, Journal of the Electrochemical Society, 159 (2012) A294-A299.
[129] P. Reale, M. Morcrette, J. Hassoun, Nanoscience and Nanotechnology Letters, 4 (2012) 132-135.
[130] P.P. Ferguson, R.A. Dunlap, J.R. Dahn, Journal of the Electrochemical Society, 157 (2010) A326-A332.
[131] K. Shen, H. Chen, F. Klaver, F.M. Mulder, M. Wagemaker, Chemistry of Materials, 26 (2014) 1608-1615.
[132] M. Fehse, M. Ben Yahia, L. Monconduit, F. Lemoigno, M.L. Doublet, F. Fischer, C. Tessier, L. Stievano, Journal of Physical Chemistry C, 118 (2014) 27210-27218.
[133] Q. Liu, Y. Liu, C.-J. Sun, Z.-f. Li, Y. Ren, W. Lu, E.A. Stach, J. Xie, Electrochimica Acta, 136 (2014) 318-322.
[134] A. Ulvestad, H.M. Cho, R. Harder, J.W. Kim, S.H. Dietze, E. Fohtung, Y.S. Meng, O.G. Shpyrko, Applied Physics Letters, 104 (2014) 073108.
[135] L. Baggetto, E.J.M. Hensen, P.H.L. Notten, Electrochimica Acta, 55 (2010) 7074-7079.
[136] W. Zhang, P.N. Duchesne, Z.L. Gong, S.Q. Wu, L. Ma, Z. Jiang, S. Zhang, P. Zhang, J.X. Mi, Y. Yang, Journal of Physical Chemistry C, 117 (2013) 11498-11505.
[137] C.J. Patridge, C.T. Love, K.E. Swider-Lyons, M.E. Twigg, D.E. Ramaker, Journal of Solid State Chemistry, 203 (2013) 134-144.
[138] D. Takamatsu, Y. Koyama, Y. Orikasa, S. Mori, T. Nakatsutsumi, T. Hirano, H. Tanida, H. Arai, Y. Uchimoto, Z. Ogumi, Angewandte Chemie-International Edition, 51 (2012) 11597-11601.
[139] K.-W. Nam, W.-S. Yoon, K. Zaghib, K.Y. Chung, X.-Q. Yang, Electrochemistry Communications, 11 (2009) 2023-2026.

[140] F.F. Yang, Y.J. Liu, S.K. Martha, Z.Y. Wu, J.C. Andrews, G.E. Ice, P. Pianetta, J. Nanda, Nano Letters, 14 (2014) 4334-4341.
[141] X.Q. Yu, Y.C. Lyu, L. Gu, H.M. Wu, S.M. Bak, Y.N. Zhou, K. Amine, S.N. Ehrlich, H. Li, K.W. Nam, X.Q. Yang, Advanced Energy Materials, 4 (2014) 1300950.
[142] J.G. Zhou, D. Hong, J. Wang, Y.F. Hu, X.H. Xie, H.T. Fang, Physical Chemistry Chemical Physics, 16 (2014) 13838-13842.
[143] J. Yoon, S. Muhammad, D. Jang, N. Sivakumar, J. Kim, W.H. Jang, Y.S. Lee, Y.U. Park, K. Kang, W.S. Yoon, Journal of Alloys and Compounds, 569 (2013) 76-81.
[144] U. Lafont, D. Carta, G. Mountjoy, A.V. Chadwick, E.M. Kelder, Journal of Physical Chemistry C, 114 (2010) 1372-1378.
[145] S.C. Chao, Y.F. Song, C.C. Wang, H.S. Sheu, H.C. Wu, N.L. Wu, Journal of Physical Chemistry C, 115 (2011) 22040-22047.
[146] S.C. Chao, Y.C. Yen, Y.F. Song, H.S. Sheu, H.C. Wu, N.L. Wu, Journal of the Electrochemical Society, 158 (2011) A1335-A1339.
[147] F.R. Brushett, L. Trahey, X.H. Xiao, J.T. Vaughey, Acs Applied Materials & Interfaces, 6 (2014) 4524-4534.
[148] D.S. Eastwood, P.M. Bayley, H.J. Chang, O.O. Taiwo, J. Vila-Comamala, D.J.L. Brett, C. Rau, P.J. Withers, P.R. Shearing, C.P. Grey, P.D. Lee, Chemical Communications, 51 (2015) 266-268.
[149] D.S. Eastwood, V. Yufit, J. Gelb, A. Gu, R.S. Bradley, S.J. Harris, D.J.L. Brett, N.P. Brandon, P.D. Lee, P.J. Withers, P.R. Shearing, Advanced Energy Materials, 4 (2014) 1300506.
[150] F. Tariq, V. Yufit, D.S. Eastwood, Y. Merla, M. Biton, B. Wu, Z.W. Chen, K. Freedman, G. Offer, E. Peled, P.D. Lee, D. Golodnitsky, N. Brandon, Ecs Electrochemistry Letters, 3 (2014) A76-A78.
[151] Y.C. Lu, E.J. Crumlin, G.M. Veith, J.R. Harding, E. Mutoro, L. Baggetto, N.J. Dudney, Z. Liu, Y. Shao-Horn, Scientific Reports, 2 (2012) 715.
[152] R. Robert, D.L. Zeng, A. Lanzirotti, P. Adamson, S.J. Clarke, C.P. Grey, Chemistry of Materials, 24 (2012) 2684-2691.
[153] T. Kawaguchi, K. Shimada, T. Ichitsubo, S. Yagi, E. Matsubara, Journal of Power Sources, 271 (2014) 431-436.
[154] S. Chattopadhyay, A.L. Lipson, H.J. Karmel, J.D. Emery, T.T. Fister, P.A. Fenter, M.C. Hersam, M.J. Bedzyk, Chemistry of Materials, 24 (2012) 3038-3043.
[155] A.v. Cresce, S.M. Russell, D.R. Baker, K.J. Gaskell, K. Xu, Nano Letters, 14 (2014) 1405-1412.
[156] C.R. Becker, K.E. Strawhecker, Q.P. McAllister, C.A. Lundgren, Acs Nano, 7 (2013) 9173-9182.
[157] A. Tokranov, B.W. Sheldon, C.Z. Li, S. Minne, X.C. Xiao, Acs Applied Materials & Interfaces, 6 (2014) 6672-6686.
[158] I.T. Lucas, E. Pollak, R. Kostecki, Electrochemistry Communications, 11 (2009) 2157-2160.
[159] Y. Tian, A. Timmons, J.R. Dahn, Journal of the Electrochemical Society, 156 (2009) A187-A191.
[160] L.X. Wang, D. Deng, L.C. Lev, S. Ng, Journal of Power Sources, 265 (2014) 140-148.
[161] R.R. Liu, X. Deng, X.R. Liu, H.J. Yan, A.M. Cao, D. Wang, Chemical Communications, 50 (2014) 15756-15759.
[162] F. Xu, C. Jung, International Journal of Electrochemical Science, 9 (2014) 380-389.
[163] Y. Takahashi, A. Kumatani, H. Munakata, H. Inomata, K. Ito, K. Ino, H. Shiku, P.R. Unwin, Y.E. Korchev, K. Kanamura, T. Matsue, Nature Communications, 5 (2014) 5450.
[164] N. Balke, S. Jesse, Y. Kim, L. Adamczyk, A. Tselev, I.N. Ivanov, N.J. Dudney, S.V. Kalinin, Nano Letters, 10 (2010) 3420-3425.
[165] S. Jesse, N. Balke, E. Eliseev, A. Tselev, N.J. Dudney, A.N. Morozovska, S.V. Kalinin, Acs Nano, 5 (2011) 9682-9695.

[166] P. Hovington, M. Dontigny, A. Guerfi, J. Trottier, M. Lagace, A. Mauger, C.M. Julien, K. Zaghib, Journal of Power Sources, 248 (2014) 457-464.
[167] S.T. Boles, C.V. Thompson, O. Kraft, R. Monig, Applied Physics Letters, 103 (2013) 263906.
[168] F. Sagane, R. Shimokawa, H. Sano, H. Sakaebe, Y. Iriyama, Journal of Power Sources, 225 (2013) 245-250.
[169] M. Nagao, A. Hayashi, M. Tatsumisago, T. Kanetsuku, T. Tsuda, S. Kuwabata, Physical Chemistry Chemical Physics, 15 (2013) 18600-18606.
[170] M. Motoyama, M. Ejiri, Y. Iriyama, Electrochemistry, 82 (2014) 364-368.
[171] Q.M. Su, L. Chang, J. Zhang, G.H. Du, B.S. Xu, Journal of Physical Chemistry C, 117 (2013) 4292-4298.
[172] L.L. Luo, J.S. Wu, J.M. Xu, V.P. Dravid, Acs Nano, 8 (2014) 11560-11566.
[173] Q.M. Su, J. Zhang, Y.S. Wu, G.H. Du, Nano Energy, 9 (2014) 264-272.
[174] Q.M. Su, J. Xie, J. Zhang, Y.J. Zhong, G.H. Du, B.S. Xu, Acs Applied Materials & Interfaces, 6 (2014) 3023-3029.
[175] Q.M. Su, G.H. Du, J. Zhang, Y.J. Zhong, B.S. Xu, Y.H. Yang, S. Neupane, K. Kadel, W.Z. Li, Acs Nano, 7 (2013) 11379-11387.
[176] X. Wang, D.-M. Tang, H. Li, W. Yi, T. Zhai, Y. Bando, D. Golberg, Chemical Communications, 48 (2012) 4812-4814.
[177] F. Wang, H.C. Yu, M.H. Chen, L.J. Wu, N. Pereira, K. Thornton, A. Van der Ven, Y.M. Zhu, G.G. Amatucci, J. Graetz, Nature Communications, 3 (2012) 1201.
[178] Q.M. Su, D. Xie, J. Zhang, G.H. Du, B.S. Xu, Acs Nano, 7 (2013) 9115-9121.
[179] W.T. Liang, L. Hong, H. Yang, F.F. Fan, Y. Liu, H. Li, J. Li, J.Y. Huang, L.Q. Chen, T. Zhu, S.L. Zhang, Nano Letters, 13 (2013) 5212-5217.
[180] W.T. Liang, H. Yang, F.F. Fan, Y. Liu, X.H. Liu, J.Y. Huang, T. Zhu, S.L. Zhang, Acs Nano, 7 (2013) 3427-3433.
[181] X. Wang, Q.H. Weng, X.Z. Liu, X.B. Wang, D.M. Tang, W. Tian, C. Zhang, W. Yi, D.Q. Liu, Y. Bando, D. Golberg, Nano Letters, 14 (2014) 1164-1171.
[182] W. Neng, M. Martini, S. Wei-ning, X. Ling, S. Li-tao, S. Yu-ting, CrystEngComm, 15 (2013) 7872-7878.
[183] M.L. Trudeau, D. Laul, R. Veillette, A.M. Serventi, A. Mauger, C.M. Julien, K. Zaghib, Journal of Power Sources, 196 (2011) 7383-7394.
[184] Y.J. Zhu, J.W. Wang, Y. Liu, X.H. Liu, A. Kushima, Y.H. Liu, Y.H. Xu, S.X. Mao, J. Li, C.S. Wang, J.Y. Huang, Advanced Materials, 25 (2013) 5461-5466.
[185] J.J. Niu, A. Kushima, X.F. Qian, L. Qi, K. Xiang, Y.M. Chiang, J. Li, Nano Letters, 14 (2014) 4005-4010.
[186] S. Lee, Y. Oshima, E. Hosono, H.S. Zhou, K. Kim, H.M. Chang, R. Kanno, K. Takayanagi, Journal of Physical Chemistry C, 117 (2013) 24236-24241.
[187] L. Zhong, R.R. Mitchell, Y. Liu, B.M. Gallant, C.V. Thompson, J.Y. Huang, S.X. Mao, Y. Shao-Horn, Nano Letters, 13 (2013) 2209-2214.
[188] S. Lee, Y. Oshima, S. Niitaka, H. Takagi, Y. Tanishiro, K. Takayanagi, Japanese Journal of Applied Physics, 51 (2012) 020202.
[189] S.Y. Liu, J. Xie, Q.M. Su, G.H. Du, S.C. Zhang, G.S. Cao, T.J. Zhu, X.B. Zhao, Nano Energy, 8 (2014) 84-94.
[190] L.F. Wang, Z. Xu, W.L. Wang, X.D. Bai, Journal of the American Chemical Society, 136 (2014) 6693-6697.
[191] X.Y. Shan, G.M. Zhou, L.C. Yin, W.J. Yu, F. Li, H.M. Cheng, Journal of Materials Chemistry A, 2 (2014) 17808-17814.
[192] M. Gu, Z.G. Wang, J.G. Connell, D.E. Perea, L.J. Lauhon, F. Gao, C.M. Wang, Acs Nano, 7 (2013) 6303-6309.
[193] K. Karki, E. Epstein, J.-H. Cho, Z. Jia, T. Li, S.T. Picraux, C. Wang, J. Cumings, Nano Letters, 12 (2012) 1392-1397.

[194] C.F. Sun, K. Karki, Z. Jia, H.W. Liao, Y. Zhang, T. Li, Y. Qi, J. Cumings, G.W. Rubloff, Y.H. Wang, Acs Nano, 7 (2013) 2717-2724.
[195] H. Yang, S. Huang, X. Huang, F. Fan, W. Liang, X.H. Liu, L.-Q. Chen, J.Y. Huang, J. Li, T. Zhu, S. Zhang, Nano Letters, 12 (2012) 1953-1958.
[196] J.M. Yuk, H.K. Seo, J.W. Choi, J.Y. Lee, Acs Nano, 8 (2014) 7478-7485.
[197] L.F. Wang, D.H. Liu, S.Z. Yang, X.Z. Tian, G.Y. Zhang, W.L. Wang, E.G. Wang, Z. Xu, X.D. Bai, Acs Nano, 8 (2014) 8249-8254.
[198] M. Gu, Y. Li, X. Li, S. Hu, X. Zhang, W. Xu, S. Thevuthasan, D.R. Baer, J.-G. Zhang, J. Liu, C. Wang, Acs Nano, 6 (2012) 8439-8447.
[199] C.M. Wang, X.L. Li, Z.G. Wang, W. Xu, J. Liu, F. Gao, L. Kovarik, J.G. Zhang, J. Howe, D.J. Burton, Z.Y. Liu, X.C. Xiao, S. Thevuthasan, D.R. Baer, Nano Letters, 12 (2012) 1624-1632.
[200] L.L. Luo, J.S. Wu, J.Y. Luo, J.X. Huang, V.P. Dravid, Scientific Reports, 4 (2014) 3863.
[201] M. Gu, X.C. Xiao, G. Liu, S. Thevuthasan, D.R. Baer, J.G. Zhang, J. Liu, N.D. Browning, C.M. Wang, Scientific Reports, 4 (2014) 3684.
[202] Y.F. Zhang, Y.J. Li, Z.Y. Wang, K.J. Zhao, Nano Letters, 14 (2014) 7161-7170.
[203] Q.Q. Li, P. Wang, Q. Feng, M.M. Mao, J.B. Liu, S.X. Mao, H.T. Wang, Chemistry of Materials, 26 (2014) 4102-4108.
[204] A.M. Nie, L.Y. Gan, Y.C. Chong, H. Asayesh-Ardakani, Q.Q. Li, C.Z. Dong, R.Z. Tao, F. Mashayek, H.T. Wang, U. Schwingenschlogl, R.F. Klie, R.S. Yassar, Acs Nano, 7 (2013) 6203-6211.
[205] L.F. Wang, Z. Xu, S.Z. Yang, X.Z. Tian, J.K. Wei, W.L. Wang, X.D. Bai, Science China-Technological Sciences, 56 (2013) 2630-2635.
[206] L.Q. Zhang, X.H. Liu, Y.-C. Perng, J. Cho, J.P. Chang, S.X. Mao, Z.Z. Ye, J.Y. Huang, Micron, 43 (2012) 1127-1133.
[207] Q.Q. Li, W.Q. Li, Q. Feng, P. Wang, M.M. Mao, J.B. Liu, L.M. Zhou, H.T. Wang, H.M. Yao, Carbon, 80 (2014) 793-798.
[208] J. Xie, F.F. Tu, Q.M. Su, G.H. Du, S.C. Zhang, T.J. Zhu, G.S. Cao, X.B. Zhao, Nano Energy, 5 (2014) 122-131.
[209] Q. Gao, M. Gu, A.M. Nie, F. Mashayek, C.M. Wang, G.M. Odegard, R. Shahbazian-Yassar, Chemistry of Materials, 26 (2014) 1660-1669.
[210] S.J. Kim, S.Y. Noh, A. Kargar, D.L. Wang, G.W. Graham, X.Q. Pan, Chemical Communications, 50 (2014) 9932-9935.
[211] L.Q. Zhang, J.S. Zhang, Y. Shao, D.Q. Jiang, F. Yang, Y.P. Guo, L.S. Cui, Nanotechnology, 24 (2013) 325702.
[212] K.E. Gregorczyk, Y. Liu, J.P. Sullivan, G.W. Rubloff, Acs Nano, 7 (2013) 6354-6360.
[213] Q.M. Su, Z.M. Dong, J. Zhang, G.H. Du, B.S. Xu, Nanotechnology, 24 (2013) 255705.
[214] A.M. Nie, Y.C. Cheng, Y.H. Zhu, H. Asayesh-Ardakani, R.Z. Tao, F. Mashayek, Y. Han, U. Schwingenschlogl, R.F. Klie, S. Vaddiraju, R. Shahbazian-Yassar, Nano Letters, 14 (2014) 5301-5307.
[215] H. Nakagawa, Y. Domi, T. Doi, M. Ochida, S. Tsubouchi, T. Yamanaka, T. Abe, Z. Ogumi, Journal of Power Sources, 236 (2013) 138-144.
[216] H. Nakagawa, Y. Domi, T. Doi, M. Ochida, S. Tsubouchi, T. Yamanaka, T. Abe, Z. Ogumi, Journal of the Electrochemical Society, 161 (2014) A480-A485.
[217] C. Sole, N.E. Drewett, L.J. Hardwick, Faraday Discussions, 172 (2014) 223-237.
[218] J. Shu, M. Shui, D. Xu, S. Gao, T.F. Yi, D.J. Wang, X. Li, Y.L. Ren, Ionics, 17 (2011) 503-509.
[219] R. Baddour-Hadjean, C. Navone, J.P. Pereira-Ramos, Electrochimica Acta, 54 (2009) 6674-6679.
[220] R. Schmitz, R.A. Muller, R.W. Schmitz, C. Schreiner, M. Kunze, A. Lex-Balducci, S. Passerini, M. Winter, Journal of Power Sources, 233 (2013) 110-114.
[221] J.T. Li, H. Su, L. Huang, S.G. Sun, Science China-Chemistry, 56 (2013) 992-996.
[222] M. Matsui, K. Dokko, K. Kanamura, Journal of the Electrochemical Society, 157 (2010) A121-A129.

[223] J.-T. Li, S.-R. Chen, F.-S. Ke, G.-Z. Wei, L. Huang, S.-G. Sun, Journal of Electroanalytical Chemistry, 649 (2010) 171-176.
[224] E. Markevich, R. Sharabi, V. Borgel, H. Gottlieb, G. Salitra, D. Aurbach, G. Semrau, M.A. Schmidt, Electrochimica Acta, 55 (2010) 2687-2696.
[225] S. Bhattacharya, A.R. Riahi, A.T. Alpas, Scripta Materialia, 64 (2011) 165-168.
[226] Y. Qi, S.J. Harris, Journal of the Electrochemical Society, 157 (2010) A741-A747.
[227] S.J. Harris, A. Timmons, D.R. Baker, C. Monroe, Chemical Physics Letters, 485 (2010) 265-274.
[228] S.J. Harris, E.K. Rahani, V.B. Shenoy, Journal of the Electrochemical Society, 159 (2012) A1501-A1507.
[229] J.B. Chen, A.K. Thapa, T.A. Berfield, Journal of Power Sources, 271 (2014) 406-413.
[230] H. Sano, H. Sakaebe, H. Matsumoto, Chemistry Letters, 42 (2013) 77-79.
[231] K. Nishikawa, T. Mori, T. Nishida, Y. Fukunaka, M. Rosso, Journal of Electroanalytical Chemistry, 661 (2011) 84-89.
[232] F. Sagane, K. Ikeda, K. Okita, H. Sano, H. Sakaebe, Y. Iriyama, Journal of Power Sources, 233 (2013) 34-42.
[233] J. Steiger, D. Kramer, R. Moenig, Electrochimica Acta, 136 (2014) 529-536.
[234] K. Nishikawa, H. Munakata, K. Kanamura, Journal of Power Sources, 243 (2013) 630-634.
[235] A. Tokranov, B.W. Sheldon, P. Lu, X. Xiao, A. Mukhopadhyay, Journal of the Electrochemical Society, 161 (2014) A58-A65.
[236] A. Mukhopadhyay, A. Tokranov, X.C. Xiao, B.W. Sheldon, Electrochimica Acta, 66 (2012) 28-37.
[237] A. Mukhopadhyay, A. Tokranov, K. Sena, X.C. Xiao, B.W. Sheldon, Carbon, 49 (2011) 2742-2749.
[238] M. Pharr, Z.G. Suo, J.J. Vlassak, Nano Letters, 13 (2013) 5570-5577.
[239] G. Bucci, S.P.V. Nadimpalli, V.A. Sethuraman, A.F. Bower, P.R. Guduru, Journal of the Mechanics and Physics of Solids, 62 (2014) 276-294.
[240] M.J. Chon, V.A. Sethuraman, A. McCormick, V. Srinivasan, P.R. Guduru, Physical Review Letters, 107 (2011) 045503.
[241] S.P.V. Nadimpalli, V.A. Sethuraman, G. Bucci, V. Srinivasan, A.F. Bower, P.R. Guduru, Journal of the Electrochemical Society, 160 (2013) A1885-A1893.
[242] V.A. Sethuraman, M.J. Chon, M. Shimshak, N. Van Winkle, P.R. Guduru, Electrochemistry Communications, 12 (2010) 1614-1617.
[243] V.A. Sethuraman, M.J. Chon, M. Shimshak, V. Srinivasan, P.R. Guduru, Journal of Power Sources, 195 (2010) 5062-5066.
[244] V.A. Sethuraman, V. Srinivasan, A.F. Bower, P.R. Guduru, Journal of the Electrochemical Society, 157 (2010) A1253-A1261.
[245] M. Pharr, Z.G. Suo, J.J. Vlassak, Journal of Power Sources, 270 (2014) 569-575.
[246] A. Mukhopadhyay, R. Kali, S. Badjate, A. Tokranov, B.W. Sheldon, Scripta Materialia, 92 (2014) 47-50.
[247] Y. Moritomo, K. Wakaume, M. Takachi, X.H. Zhu, H. Kamioka, Journal of the Physical Society of Japan, 82 (2013).
[248] P. Mukherjee, A. Lagutchev, D.D. Dlott, Journal of the Electrochemical Society, 159 (2012) A244-A252.
[249] F. Chevalier, F. Poli, B. Montigny, M. Letellier, Carbon, 61 (2013) 140-153.
[250] K. Gotoh, M. Izuka, J. Arai, Y. Okada, T. Sugiyama, K. Takeda, H. Ishida, Carbon, 79 (2014) 380-387.
[251] N. Schweikert, A. Hofmann, M. Schulz, M. Scheuermann, S.T. Boles, T. Hanemann, H. Hahn, S. Indris, Journal of Power Sources, 228 (2013) 237-243.
[252] B. Key, R. Bhattacharyya, M. Morcrette, V. Seznec, J.M. Tarascon, C.P. Grey, Journal of the American Chemical Society, 131 (2009) 9239-9249.

[253] K. Ogata, E. Salager, C.J. Kerr, A.E. Fraser, C. Ducati, A.J. Morris, S. Hofmann, C.P. Grey, Nature Communications, 5 (2014) 3217.
[254] M. Giesecke, S.V. Dvinskikh, I. Furo, Journal of Magnetic Resonance, 226 (2013) 19-21.
[255] L. Aldon, A. Perea, Journal of Power Sources, 196 (2011) 1342-1348.
[256] J. Wandt, C. Marino, H.A. Gasteiger, P. Jakes, R.-A. Eichel, J. Granwehr, Energy & Environmental Science, (2015) 1358-1367.
[257] G. Gershinsky, E. Bar, L. Monconduit, D. Zitoun, Energy & Environmental Science, 7 (2014) 2012-2016.
[258] N. Sharma, M.V. Reddy, G.D. Du, S. Adams, B.V.R. Chowdari, Z.P. Guo, V.K. Peterson, Journal of Physical Chemistry C, 115 (2011) 21473-21480.
[259] N. Sharma, D.H. Yu, Y.S. Zhu, Y.P. Wu, V.K. Peterson, Chemistry of Materials, 25 (2013) 754-760.
[260] M. Bianchini, E. Suard, L. Croguennec, C. Masquelier, Journal of Physical Chemistry C, 118 (2014) 25947-25955.
[261] W.K. Pang, N. Sharma, V.K. Peterson, J.J. Shiu, S.H. Wu, Journal of Power Sources, 246 (2013) 464-472.
[262] J.-F. Colin, V. Godbole, P. Novak, Electrochemistry Communications, 12 (2010) 804-807.
[263] N. Sharma, G.D. Du, A.J. Studer, Z.P. Guo, V.K. Peterson, Solid State Ionics, 199 (2011) 37-43.
[264] G.D. Du, N. Sharma, V.K. Peterson, J.A. Kimpton, D.Z. Jia, Z.P. Guo, Advanced Functional Materials, 21 (2011) 3990-3997.
[265] X.L. Wang, K. An, L. Cai, Z.L. Feng, S.E. Nagler, C. Daniel, K.J. Rhodes, A.D. Stoica, H.D. Skorpenske, C.D. Liang, W. Zhang, J. Kim, Y. Qi, S.J. Harris, Scientific Reports, 2 (2012) 747.
[266] O. Dolotko, A. Senyshyn, M.J. Muhlbauer, K. Nikolowski, F. Scheiba, H. Ehrenberg, Journal of the Electrochemical Society, 159 (2012) A2082-A2088.
[267] L. Cai, K. An, Z. Feng, C. Liang, S.J. Harris, Journal of Power Sources, 236 (2013) 163-168.
[268] N. Sharma, V.K. Peterson, Journal of Power Sources, 244 (2013) 695-701.
[269] M.A. Rodriguez, M.H. Van Benthem, D. Ingersoll, S.C. Vogel, H.M. Reiche, Powder Diffraction, 25 (2010) 143-148.
[270] I.A. Bobrikov, A.M. Balagurov, C.W. Hu, C.H. Lee, T.Y. Chen, S. Deleg, D.A. Balagurov, Journal of Power Sources, 258 (2014) 356-364.
[271] V. Zinth, C. von Luders, M. Hofmann, J. Hattendorff, I. Buchberger, S. Erhard, J. Rebelo-Kornmeier, A. Jossen, R. Gilles, Journal of Power Sources, 271 (2014) 152-159.
[272] B. Jerliu, E. Huger, L. Dorrer, B.K. Seidlhofer, R. Steitz, V. Oberst, U. Geckle, M. Bruns, H. Schmidt, Journal of Physical Chemistry C, 118 (2014) 9395-9399.
[273] J.E. Owejan, J.P. Owejan, S.C. DeCaluwe, J.A. Dura, Chemistry of Materials, 24 (2012) 2133-2140.
[274] A. Senyshyn, M.J. Muhlbauer, O. Dolotko, M. Hofmann, T. Pirling, H. Ehrenberg, Journal of Power Sources, 245 (2014) 678-683.
[275] J.P. Owejan, J.J. Gagliardo, S.J. Harris, H. Wang, D.S. Hussey, D.L. Jacobson, Electrochimica Acta, 66 (2012) 94-99.
[276] A. Same, V. Battaglia, H.Y. Tang, J.W. Park, Journal of Applied Electrochemistry, 42 (2012) 1-9.
[277] J.B. Siegel, X.F. Lin, A.G. Stefanopoulou, D.S. Hussey, D.L. Jacobson, D. Gorsich, Journal of the Electrochemical Society, 158 (2011) A523-A529.
[278] J.H. Wang, D.X. Liu, M. Canova, R.G. Downing, L.R. Cao, A.C. Co, Journal of Radioanalytical and Nuclear Chemistry, 301 (2014) 277-284.

4

Spatio-temporal Quantification of lithium both in Electrode and in Electrolyte with atomic precision via Operando Neutron Absorption

This chapter has been published as PPRML Harks, TW Verhallen, C George, JK van den Biesen, Q Liu, M Wagemaker, FM Mulder, Journal American Chemical Society 141 (36), 14280-14287 (2019)

4.1 Introduction

Clean energy sources are transforming the energy landscape, as sustainable power sources are intrinsically intermittent and unable to match supply and demand[1-4]. Electrochemical energy storage has become paramount to stabilize the grid and mitigate this mismatch[1,5]. To this end, developing safe and cost-effective rechargeable batteries lays the necessary foundation and among the various battery chemistries available today, the high theoretical energy density (2600 Wh/kg), natural abundancy of sulfur (~2.9%), environmental benignity (low toxicity) and low cost make lithium-sulfur (Li-S) batteries highly attractive alternative to supersede the current Li ion technology[6-8].

Nevertheless, the Li-S battery system suffers from rapid capacity fading and poor round-trip efficiency [6,7], which seem inherently linked to the material properties of sulfur, i.e. dissolution of the intermediate lithium polysulfide species in the battery electrolyte and Li metal corrosion via polysulfide accumulation[6,7]. The discharge curve of a Li–S battery consists of a high (≈2.3 V) and a low (≈2.0 V) voltage plateau, attributed to a solid (S_8)→liquid (Li_2S_x)→solid (Li_2S_2/Li_2S) process with a gradual decrease in the sulfur chain length. The high plateau is ascribed to the reduction of the cyclic S_8 ring to soluble long chain polysulfides (Li_2S_x, $4 < x < 8$), while the low voltage plateau is believed to correspond to further reduction of polysulfides to solid Li_2S_2/Li_2S[9,10]. A conductive matrix, most commonly carbon, provides both a pathway for electrons and reaction sites, such that the migrated Li ions can shorten the sulfide backbone until the solid product Li_2S is formed[11].

This 'solid-liquid-solid' mode of operation inevitably incurs a number of issues. Since the intermediate products are dissolved, the active material is no longer confined to the electrode region and instead are able to migrate to the anode, where they undergo parasitic reactions. This not only severely limits the practical performance of Li-S batteries, it is also the root cause for battery self-discharge and capacity decay[12]. Nonetheless, sulfur has an extremely low electronic conductivity, thus rendering it unsuitable as active material in the traditional sense. Hence the redox process is enabled owing to the limited but sufficient solubility in organic electrolytes of elemental sulfur and the high solubility of the electrochemically produced polysulfides[7], thereby circumventing the limitation of low electronic conductivity of bulk sulfur effectively[8,13].

Nonetheless, the migration must be restrained in order to achieve reasonable capacity. A common approach is to add additives to the electrolyte that passivate the anode surface, such as lithium nitrate ($LiNO_3$)[14]. Through chemical reaction with S and Li, $LiNO_3$ incurs the formation of a passivating layer on the Li anode. This layer prevents Li metal from being directly exposed to polysulfides, while allowing Li-ion conduction, due to ion conductive Li_3N species[15]. However,

morphological changes during cyclic Li re-deposition cause repetitive break-down of the passivating layer and hence inducing continuous consumption of the $LiNO_3$. Another potential bottleneck is that although $LiNO_3$ has a sufficient electrochemical stability window that covers the operating potential limits of Li-S batteries, discharging below 1.7V reduces the $LiNO_3$ at the cathode, adversely affecting the battery performance[14,16]. More importantly, this additive alone cannot inhibit the active material from diffusing out of the electrode region.

Aimed at avoiding active material loss, efforts were focused on physically encapsulating the sulfur active material within hollow carbon structures. Yet the weak interaction between carbon and polysulfide yielded little improvements in terms of cycle life, especially when benchmarked against the current Li-ion cells[13,17]. Recently, chemical bonding strategies for immobilizing polysulfides have been developed[18], which are based on the strong interactions between polar functional groups and polysulfides[18-20]. Functional groups (e.g. oxygen, boron, nitrogen and sulfur) are introduced to electrodes via the conductive additive (carbon matrix), or by dispersing polymer or (transition) metal oxide additives (e.g. TiO_2 and $Li_4Ti_5O_{12}$)[21]. Their addition has offered considerable improvements in the performance of Li-S batteries, such as increased battery capacity and elongated cycle life[22,23]. The beneficial effects are attributed to their high polarity which should yield a high chemical affinity towards polysulfide species[24]. Yet, to date, direct experimental evidence is completely lacking.

Among the reasons is the intrinsic difficulty to study light ions, such as lithium, using methods based on X-rays or electrons[21,25,26]. Furthermore these dynamic and delicate processes escape the probing ability of ex-situ methods[25]. Operando diffractometric techniques are powerful in detecting the formation of crystalline phases, yet the considerable amount of amorphous phases and nanocrystalline particles cannot be resolved[11]. Nonetheless, the vast majority of the studies have relied on ex-situ measurements and electrochemical testing, as operando techniques are sparsely employed in Li-S battery research[23]. However, to advance rational Li-S electrode design by taking maximal advantage of these transition metal approaches requires understanding the full breadth of Li-S mechanistic processes, starting from experimental observations in real time.

Neutron Depth Profiling (NDP) allows for the absolute detection of Li with atomic selectivity, independent of the oxidation state or phase. As NDP exploits neutron capture reaction of the lithium-6 isotope, it ensures unique selectivity and intrinsic low noise, whereas the high depth of penetration of neutrons allows practical sample environments, i.e. resembling a commercial cell[27-30]. In this neutron capture reaction, a thermal neutron is absorbed by a ^6Li atom initiating the

formation of two charged particles with a well-defined energy, according to **equation 4.1**[31,32];

$$^{6}Li + n_{thermal} \xrightarrow{yields} {}^{3}H^{+}\ (2727.88keV) + He^{2+}\ (2055.12keV) \qquad \textbf{eq. 4.1}$$

The nuclear reaction energy released is much larger than the energy of a thermal neutron (~25 meV), hence the charged particle kinetic energies are constant, independent of the neutron energy. A fraction of particles that escape the sample are detected with an energy sensitive detector, as is illustrated in **Fig. 4.1**, adapted from ref [26].

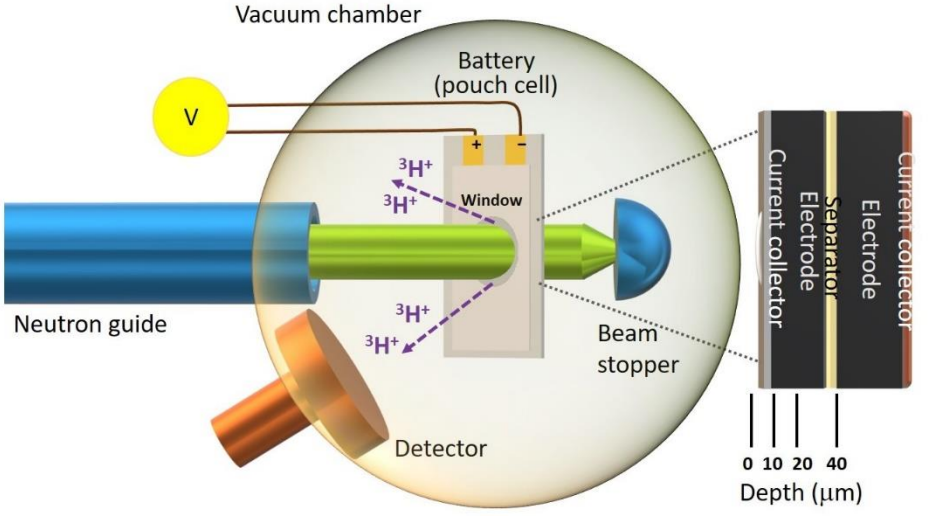

Figure 4.1. Schematic representation of the operando neutron depth profiling (NDP) setup, the inset shows a cross section of a pouch cell and indicates the electrode region probed.

The charged particle detector opening angle is decreased by the sample to detector distance such that incoming the $^{3}H^{+}$ and $^{4}He^{2+}$ particles trajectories are close to perpendicular to both detector and sample plane. The particles lose energy as they travel through the battery electrode materials, the resulting energy is measured by the detector. The energy difference, caused by energy lost in the material, is a measure of the original isotope depth in the sample. Hence through neutron depth profiling a cross sectional averaged Li concentration profile as a function of depth is determined, i.e. along the axis perpendicular to the sample surface[32]. The ability to measure the ^{6}Li isotope independent of oxidation state allows for the simultaneous detection of lithium in both electrode and electrolyte, which makes NDP a unique battery diagnostic platform to unravel the space and time dependent

lithium density resulting from the complex electrochemical processes taking place across battery electrodes[27].

To reveal electrode-wide dynamics that govern polysulfide behavior in Li-S batteries three groups of electrodes are investigated; a standard carbon-sulfur composite electrode, one standard carbon-sulfur composite electrode with a membrane containing 140nm $Li_4Ti_5O_{12}$ particles and an electrode with 10%wt 140nm $Li_4Ti_5O_{12}$ particles added[33]. These cells will be referred to as *Standard*, *Layered* and *Composite* respectively. In the layered cell the $Li_4Ti_5O_{12}$ particles are not connected electronically to the current collector, whereas in the composite cell, carbon, binder, active material (sulfur) and $Li_4Ti_5O_{12}$ particles are intimately mixed. Through measuring and quantifying the local lithium concentration across these electrodes, direct evidence for Li containing polysulfide dissolution, migration and adsorption by metal oxides is presented.

4.2 Results and discussion

Fig. 4.2 shows the lithium concentration profiles obtained from the pristine cells during their initial resting time. At zero the current collector/battery electrode interface is located. On the right, at high depths, the electrolyte region is located. The lithium concentration in the electrolyte should be close to 1.2 molar, LiTFSI and $LiNO_3$ in TEGDME. Hence even though no current was drawn from the cells, Li ions of the battery electrolyte, which has infiltrated the porous network of electrode, are measured. For the standard electrode, indicated by the black squares, a nearly constant lithium concentration of 0.8 molar is measured. This is lower as part of the volume is occupied by intrinsically lithium-free components, carbon, PDVF binder and active material or the battery separator. In the other samples, the presence of Li in the LTO of the composite electrode and the membrane of the layered cell increases the Li-density and therefore signal those specific regions, as the Li concentration in pure LTO is over 30 mol/l. The layered cell shows a strong Li increase at ~15 micron depth where the LTO membrane is located. Note that a step transition is not to be expected as a transverse average of the full electrode interface is measured, which, due to the rough interface of the electrode and membrane leads to a sloping concentration. Similarly, the 10wt% of LTO in the composite electrode occupies 6% of the volume, thereby increasing the lithium concentration to 1.7 molar, indicated by the red spheres, shows a small step at 7 micron, thereby marking the pristine electrode thickness. The Li-concentration in the composite electrode converges with increasing depth towards the same concentration as the standard electrode, representing the concentration in the separator. In conclusion, by addition of LTO to the electrode, the pristine electrode thickness can be

retrieved, thus enhancing the ability to monitor the location of Li upon reduction of sulfur during battery discharge.

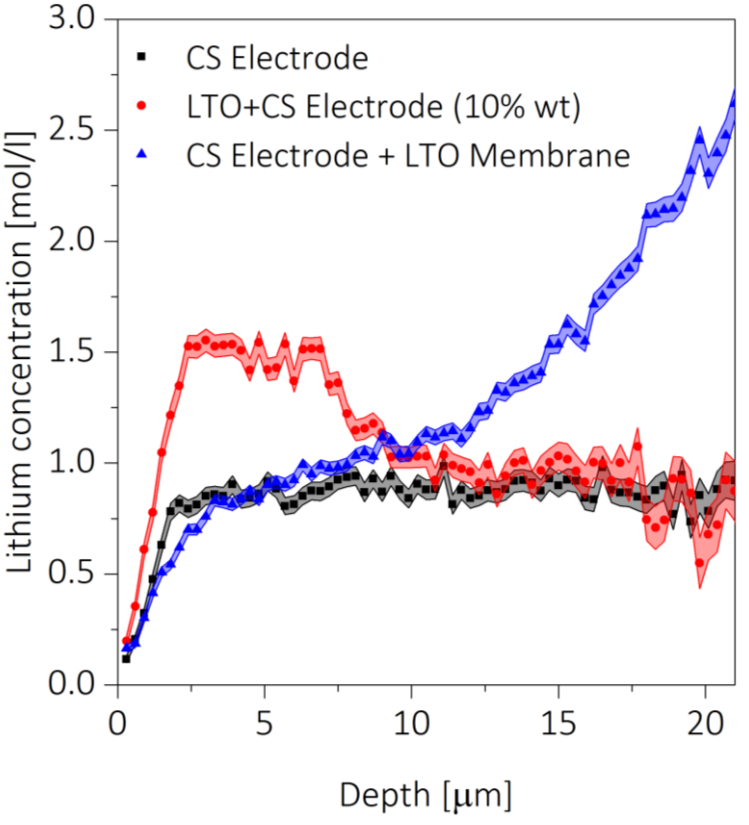

Figure 4.2. Pristine cells with different electrodes, neuron depth profiling measurements obtained during the rest period before discharge. The end of the aluminum current collector/window is at 0 micron depth, from which the porous electrode starts. The error bars increase with depth as the subtracted background is larger for lower energies hence the signal to noise ratio decreases while the measurement uncertainty increases.

As we focus on the role of LTO in this type of batteries, the results obtained on the standard electrode are found in the supplementary information, **Fig. S4.3**. The results on the additive cells are given in **Fig. 4.3.** These color contour images show lithium concentration versus time (horizontal) and electrode depth (vertical) during L-S battery discharge. The plots shown the Li concentration increase during discharge. To remove the contribution of the pristine electrolyte the concentration of the standard cell (black line in **Fig. 4.2**) has been subtracted. This correction

highlights the change in lithium concentration over time both in the electrode and in the electrolyte.

The bottom panels indicate the cell voltage versus Li. The discharge voltage and plateaus are characteristic of the curve of a Li-S battery. The battery discharge cut-off voltage was set to 1.7V, in order to prevent electrochemical activity of LTO, as well as decomposition of $LiNO_3$. Therefore, the recorded lithium concentration increase is solely due to the electrochemical activity of sulfur forming soluble and solid discharge products, i.e. polysulfide species.

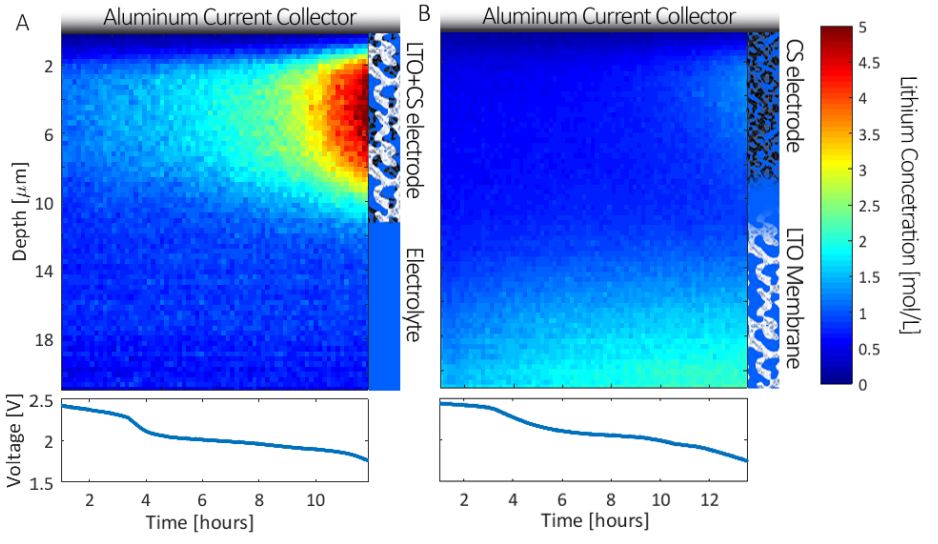

Figure 4.3. Color contour neuron depth profiling images show the increase in lithium concentration with time versus depth at a constant current discharge; the initial signal of electrolyte and LTO has been subtracted. The aluminum current collector/window is at the top of the plot whereas the electrolyte (and membrane) are found below. **A** depicts the LTO+CS electrode and **B** The standard CS electrode and LTO membrane.

Fig. 4.3A shows the results from the composite electrode. Surprisingly it appears that the most of the lithiation concentration increase takes place at the end of discharge. This apparently contradicts the view that sulfur reduction should occur at a constant rate on the conductive carbon cathode surface as a constant current is applied. This indicates that the oxidized Li is stored in the electrolyte in the form of soluble polysulfide species. Furthermore these species rapidly diffuse and equilibrate in the electrolyte, since no significant concentration change is observed in the first ~20 micron visible with NDP, although the sulfur reduction accompanying the Li+ concentration growth in the electrolyte will occur on the

electronically conductive carbon. Note that a 250 micron thick separator is used which poses a significant polysulfide reservoir.

At the end of discharge a high lithium concentration is attained in this electrode. Furthermore the electrode layer thickness slightly increases, reaching 11 micron at the end of charge (volume expansion). This is a 50 % increase when compared to **Fig. 4.2**, where the original layer thickness was deduced from the LTO additive. Proving that even though the active material is deposited from soluble products, the solid deposits are able to strain the carbon host matrix.

Fig. 4.3B shows the layered cell with an LTO membrane. The increased lithium concentration due to the LTO membrane at depths above 10 micron is obvious. In this case, lithiation of the electrode area itself does not progress as significant as in the composite electrode, even though the same C-rate is applied. Especially in the first half of the discharge there is no visible concentration increase in the electrode region, however, there is a pronounced concentration increase within the LTO membrane. This means that a large fraction of the oxidized Li and reduced sulfur is actually stored within the membrane, instead of the electrode region at depths, i.e. below 12 μm. We can safely rule out the possibility of the intercalation or lithiation of LTO particles as the cell potential is well above the 1.55V, where intercalation in LTO occurs. Therefore it can be rationalized that the accumulation of Li in the LTO membrane is not a result of an electrochemical process within the LTO region but is due to the adsorption of Li polysulfides that are produced in the electronically conductive electrode area and then concentrate within the LTO membrane. In other words, they migrate from the electrode region and are confined within the LTO membrane, apparently preventing subsequent Li migration to the anode. To our knowledge, this is the first direct evidence of the ability of LTO to bond the dissolute Li-polysulfide species. In the second half of discharge the electrode region (< 12 μm) does show an increase in lithium concentration. This lithiation might result from low solubility solid products, which deposit on the carbon matrix. This deposition can only occur when electrons are supplied and this process is therefore restricted to the electrode region. However, the concentration of lithium in the membrane does not decrease, which indicates that the absorbed species are relatively stable and do not re-dissolve to keep the reaction going. Hence the final concentration attained in the carbon-sulfur electrode with LTO membrane is much lower, which also corroborates its relatively low capacity. This can explain why a Li-S electrode design involving cathode interlayers offers sub-optimal battery performance, if the interlayer does not provide high electron conductivity or other properties aiding the re-dissolution and reduction of polysulfides.

Hence it seems lithiation proceeds sequentially in the available regions, that is in the electrode and electrolyte/membrane region. To further explore this behavior the counts from the two different regions in the cell are summed; the region from 0-12 micron represents the entire host matrix (standard carbon-sulfur or composite) available in electrodes for lithiation and the region from 12-28 micron encompasses the measurable part of the electrolyte or the membrane only. Simultaneously this increases measurement statistics. Next the measured Li concentration increase, integrated over these two separate regions, is related to the current that was retrieved from the battery during discharge, thereby elucidating differences in C-rated current and allowing direct comparison to the cell electrochemistry.

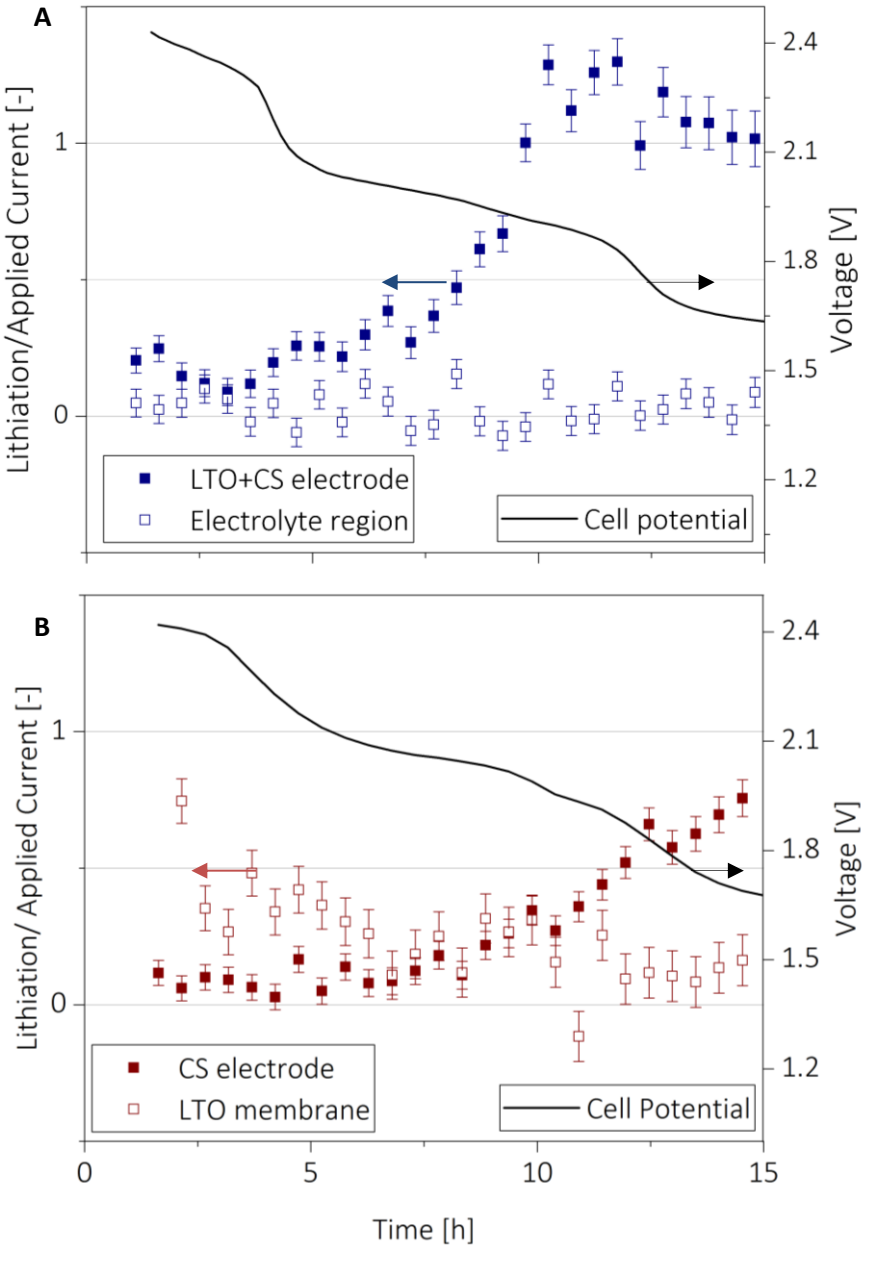

Figure 4.4. Regional lithiation defined as the Li concentration increase per time unit divided by the current and plotted versus discharge time. **(a)** Here blue symbols reflect composite electrode cell and **(b)** red symbols the standard electrode with membrane, filled squares indicate electrode region whereas open spheres denoted electrolyte and electrolyte/membrane region. Data has been binned, error bars reflect the spread in the data set of one point.

In a conventional intercalation type battery, the ratio between lithiation and the obtained current should be 1 for the electrode region (assuming no significant side reactions are taking place). This is because for the amount of negative charge produced per second (current) from the battery, the same amount of positive charge (Li ions) should be inserted into the positive electrode (during discharge). Similarly, a ratio of 1 in the case of a Li-S battery means the shuttle is completely stopped as for every electron a lithium is stored in the electrode, with no lithium diffusing into the electrolyte. It should be noted that the ratio for the electrode and electrolyte combined, also can be lower than 1 as the electrolyte is not fully probed in this study and therefore polysulfides can exist outside the measured area. During initial stages of discharge, at the first plateau 2.5-2.3V, the current divided by the lithiation speed is indeed lower than 1. Here, for both types of electrodes, the lithium increase is slower than expected based on the applied current in the total measurable domain, in **Fig. 4.4**. This, in line with Li concentration profiles in **Fig. 4.3**, can be explained by diffusion of Li_2S_n polysulfide species. In this voltage range highly soluble polysulfides are formed and driven out of the electrode by their concentration gradient. The corresponding increase in Li concentration in both cells spreads over an extended electrolyte area and therefore the change in Li concentration does not supersede the measurement error inside the probed area. Although the increase in lithium concentration is lower than expected due to the diffusion of PS, in both electrodes the regions that contain LTO do exhibit lithiation. In **Fig. 4.4a**, the composite electrode shows significant electrochemical activity whereas the electrolyte region barely changes. Even more obvious is the change in the membrane region of the layered cell, **Fig. 4.4b**. Here, because of the high LTO concentration (85 wt%) in the membrane, more surface area for adsorption is available within the LTO membrane, which is why lithiation proceeds more readily at this stage of discharge. As the cell potential forbids electrochemical activity of the LTO, the sole explanation for the observed lithiation are adsorbed polysulfide species. A direct indication that indeed LTO can retain lithium sulfur based solutes. In the second stage of discharge, when the voltage reaches the 2V plateau a clear shift is seen. The composite electrode shows a sudden increase in lithiation speed halfway through the second plateau, the relative lithiation even exceeds 1. This reveals that solid compounds are formed, rapidly consuming the polysulfide species present in the electrolyte in the porous network of the electrode as well as on the surface of the LTO particles. Together with (two) Li ions from the electrolyte these species are reduced to insoluble products, which are subsequently deposited on the carbon substrate. On top of this process the lowering of the local PS concentration and results in a net influx of these species from the electrolyte reservoir, hence leading to the observed 'surplus' in lithiation speed. The fact that

the observed value surpasses 1 is thereby proof that solid sulfur compounds are formed.

In **Fig. 4.4b,** the layered cell also shows the jump in lithiation speed, albeit somewhat later in the discharge process. Moreover, there is an obvious transition during this voltage plateau, as the activity is moving from the membrane to the electrode region. The contribution to the current of the membrane does not become negative. Hence the otherwise mobile polysulfide species, formed during the first stages of discharge, are irreversibly trapped in the membrane**.** The LTO membrane is incapable of supplying the adhered lithium sulfides with electrons, therefore, these polysulfides cannot be further reduced. Furthermore the jump is much lower than previously seen for the composite electrode, the ratio between lithium concentration increase and applied current never reaches 1. A clear indication of soluble products, and consequently capacity, is leaving the measurement scope. This explains the poor capacity obtained for this cell compared to the composite electrode.

To exclude the scenario that significant regions of the carbon matrix are outside of the window, the potential was decreased further (to ~1.6V), such that the NO_3 anions become instable, forming lithium oxide according to;

$$2Li^+ + NO_3{}^- + 2e^- = Li_2O(s) + NO_2{}^-$$

This would cause solid deposition of Li_2O on the carbon host, and the exchange of NO_3^- with NO_2^- ions in solution. Hence this insoluble lithium oxide is only formed on the carbon electrode matrix. Therefore at 1.6 V the lithiation (normalized to the current) in the electrode should be found to be ~1 for both electrode configurations. This is the case for both cells, proving that the electrochemically active regions are fully within the window of the measurement.

However, it should be noted that for both systems the absorption rate of polysulfides onto the LTO nanopowder does not occur on par with the applied current, which could be due to a lack of available surface sites. Here commercially available LTO nanopowder is used, which is not intended for this application[33]. Surely room for optimization is available, however, it is shown that operando NDP is a powerful tool to unambiguously show the effectivity of proposed Li polysulfide retention mechanisms.

Based on our NDP spatiotemporal measurements, we were able to piece together a comprehensive picture of Li-S batteries at work, as sketched in **Fig. 4.5**. Starting from the rest period, where at OCP dissolved S_8 rings are in an equilibrium concentration with the electrolyte. As soon as electrons are supplied, these rings are allowed to open and form PS complexes. This initiates to progressive

dissolution of the sulfur active material, see **Fig. 4.5B.** These complexes are molecules or possibly ionized to Li^+ and S_n^{2-}. From the results shown in **Fig. 4.3 and 4.4**, we can confirm that the soluble polysulfides migrate out of the electrode and are adsorbed at LTO sites. In the case of the layered cell, this migration is observed by a subpar lithiation speed and through the lithium concentration increase in the LTO membrane, which at this voltage can only be attributed to absorbed lithium polysulfide species. This adsorption process also takes place in the composite electrode, but to a smaller extend due to the lower LTO loading. In the last step (**Fig. 4.5C**) the dissolved polysulfide species react to form solid compounds which can only occur on a conducting surface, leading to a lithium ion concentration increase in the electrode region. Then the available polysulfide species are consumed, which in the composite electrode cell leads to a higher Li concentration, as adsorbed polysulfide can diffuse over the LTO surface to be reduced at the carbon matrix, whereas in the CS + LTO membrane electrode (layered) they are contained by the membrane, unable to participate in further reactions. Due to the conversion of dissolved polysulfide into solid products, the concentration in the electrode area decreases, hence it becomes thermodynamically favorable for polysulfide species from the electrolyte to diffuse towards the electrode region. This additional flux is registered atop of the reaction necessary to sustain the current.

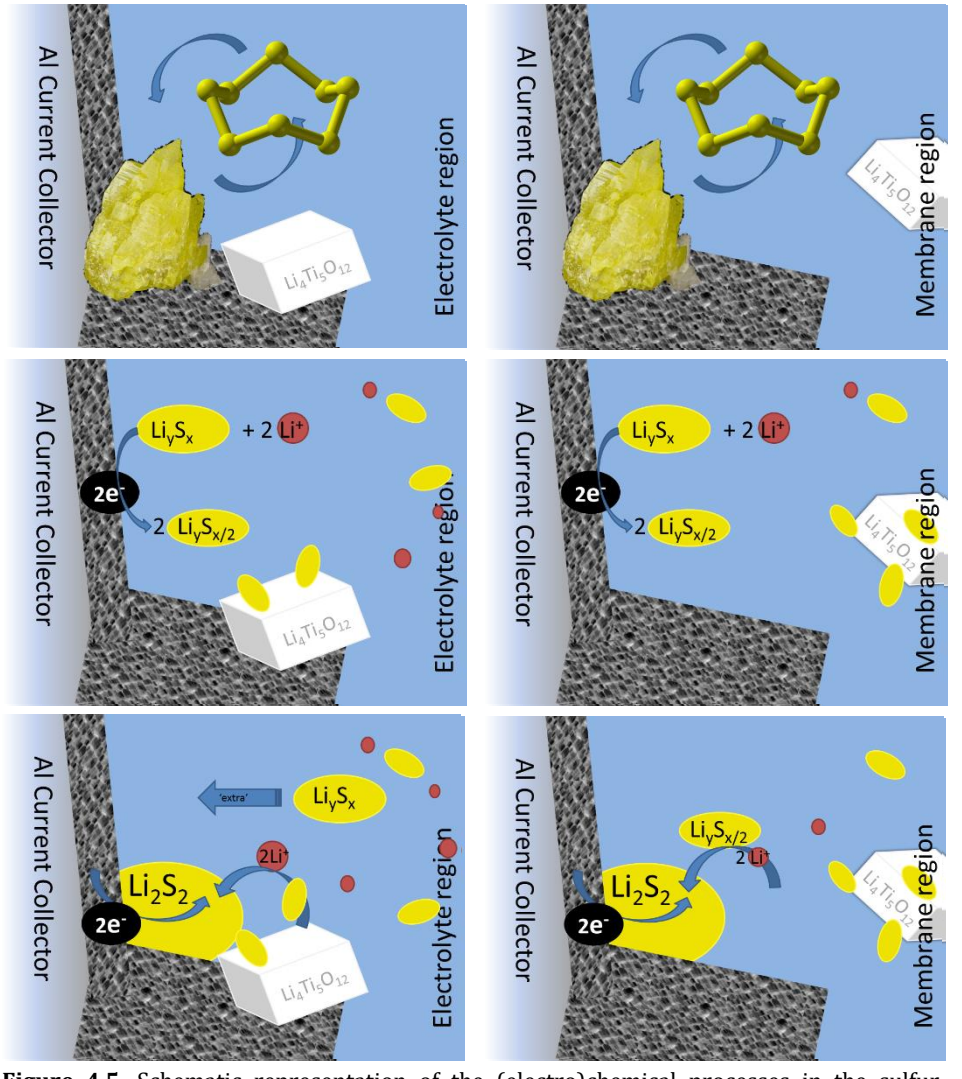

Figure 4.5. Schematic representation of the (electro)chemical processes in the sulfur electrodes during discharge as derived from the operando NDP measurements.

4.3 Conclusion

By using neutron depth profiling (NDP) we presented real-time evidence for polysulfide migration during different stages of the Li-S cell discharge process. As NDP enables us to measure Li concentration both in electrode and electrolyte simultaneously, we also presented the first in-operando evidence of polysulfide adsorption onto metal oxide (LTO). By comparing the electrochemical processes and the diffusional behavior of active material in Li-S batteries using three

electrode types of Li-S based cells spatio-temporally measured via NDP, we set forth conclusive views that;

(i) The utilization of the Li-S capacity is highly dependent on the availability of sulfur, the migration and adsorption of polysulfides and the applied current, demonstrating the importance of operando methods to determine accurately the inner mechanistic processes.

(ii) Dissolved active species readily escape the electrode region, but remain mobile and therefore are able to return at a later stage in the discharge.

(iii) Volume expansion can be in part offset by the dissolution of polysulfide, however the formation of solid products can strain the host matrix significantly.

(iv) Trapping of polysulfides by using a metal oxide membrane interlayer does not necessarily improve the capacity of a Li-S battery. Instead ideal trapping-agents are mixed in the electrode matrix and electronically conductive, such that the agent can transfer electrons to the adhered species. Hence providing a catalytic function and aiding polysulfide redox reaction towards solid deposition.

We therefore remark that for the design of commercial sulfur batteries, finding the optimum ratio between sulfur and adsorbing additive for dissolution and confinement and reutilization of polysulfide, is indispensable.. Thus, our findings enabled by spatio-temporal NDP measurement can guide both Li-S electrode and cell-design with negligible capacity fade and improved life, which is the crucial step towards realizing commercially viable Li-S batteries.

4.4 Methods

Electrodes were prepared by the conventional slurry based process. A slurry was prepared by mixing Sulfur (Sigma Aldrich), Ketjen black (Akzo Nobel), KS4 graphite (Timcal) and PVDF (Kynar Flex) in a weight ratio of 60:15:10:15 in N-methyl pyrolidone (NMP, from Sigma Aldrich). For the LTO containing electrodes, 10 wt% pure LTO (particle size ~150 nm, Süd-Chemie) was applied to the mixture, at the expense of sulfur. The slurry was then casted onto Al-foil using a doctor blade. LTO membranes were prepared by mixing LTO and PVDF in a weight ratio of 85:15, without a conductive additive. The semiconducting LTO's intrinsic low electronic conductivity and low operating potential should prevent electrochemical energy storage in the membrane and thereby solely showcasing the polysulfide confinement ability. The slurry was subsequently casted on a glass substrate and then immersed in demineralized water, which produced a free-standing membrane which is self-detachable from the substrate. This membrane is then dried and

stacked upon a standard carbon sulfur electrode, the two are not pressed or calendared to avoid electronic contact. Interested readers are referred to the supplementary information for SEM images of electrode cross sections.

The cells were assembled inside an Ar filled glovebox with oxygen and water content less than 1 ppm. Lithium foil was used as the counter and reference electrode, combined with a glass fiber (Whatman) separator (~250 micron thick) and the working electrodes to make up the cell. As electrolyte a solution of 1M LiTFSI in TEGDME was used, with 1 wt% $LiNO_3$ additive. The galvanostatic cycling experiments were performed with a programmable Maccor 4000 series galvanostat. The cells were discharged to 1 V and charged to 3.8 V vs. Li^+/Li^0 at various C-rates (1C = 1675 $mA \cdot g^{-1}$).Prior to electrochemical measurements, the electrodes were shortly dried at 60°C in a vacuum oven.

Pouch cells or coffee bag cells, similar to industrial practice were used in the neutron depth profiling set-up[34,35]. Their simplicity allows straightforward sealing of the current collector with the pouch material, enabling it to be used as a window for the ^3H ions[36,37]. A window diameter of 16 mm was used, whilst electrodes were cast within a 13 mm diameter to facilitate alignment. Despite the high capacity and associated volume change of sulfur (80%)[38] a constant energy to depth conversion is used, rationalized by the mere minor differences in the stopping power between the lithiated sulfur and the pristine material, especially in relation to the other constituents. The use of the low vapor pressure TEGDME solvent allows operation in the vacuum chamber of the NDP experiment[39].

In the NDP experiments the tritons, $^3H^+$, formed from neutron capture are counted versus particle energy. Every, $^3H^+$, counted reflects one lithium (^6Li), while the associated energy reflects the depth of origin on the trajectory towards the detection. The energy lost per unit of length, or the stopping power, is calculated straightforwardly by taking into account all electrode constituents and their volume ratios[27]. It should be noted that all constituents are of similar stopping power and hence a change in volume ratio should not significantly alter the depth interpretation, see details in the **supporting information** chapter. Together the depth, sample area, measured beam intensity and known measurement efficiency allows for the translation of $^3H^+$ counts into Li concentration as shown in **Fig. 4.2**[26]**.**

References

1 Mulder, F. M., Implications of diurnal and seasonal variations in renewable energy generation for large scale energy storage. *Journal of Renewable and Sustainable Energy* **6**, *033105 (2014)*

2 Dunn, B., Kamath, H. & Tarascon, J.-M. Electrical Energy Storage for the Grid: A Battery of Choices. *Science* **334**, 928-935, doi:10.1126/science.1212741 (2011).

3 Armaroli, N. & Balzani, V. Towards an electricity-powered world. *Energy & Environmental Science* **4**, 3193-3222, doi:10.1039/C1EE01249E (2011).

4 Aggeler, D. *et al.* in *2010 IEEE PES Innovative Smart Grid Technologies Conference Europe (ISGT Europe).* 1-8.

5 Keshan, H., Thornburg, J. & Ustun, T. S. in *4th IET Clean Energy and Technology Conference (CEAT 2016).* 1-7.

6 Kang, H. S. *et al.* A Scaled-Up Lithium (Ion)-Sulfur Battery: Newly Faced Problems and Solutions. *Advanced Materials Technologies* **1**, 1600052, doi:10.1002/admt.201600052 (2016).

7 Harks, P. P. R. M. L., Robledo, C. B., Verhallen, T. W., Notten, P. H. L. & Mulder, F. M. The Significance of Elemental Sulfur Dissolution in Liquid Electrolyte Lithium Sulfur Batteries. *Adv Energy Mater* **7**, 1601635-n/a, doi:10.1002/aenm.201601635 (2017).

8 Manthiram, A., Fu, Y., Chung, S.-H., Zu, C. & Su, Y.-S. Rechargeable Lithium–Sulfur Batteries. *Chemical Reviews* **114**, 11751-11787, doi:10.1021/cr500062v (2014).

9 Zhao, E. Y. *et al.* Advanced Characterization Techniques in Promoting Mechanism Understanding for Lithium-Sulfur Batteries. *Advanced Functional Materials* **28**, doi:10.1002/adfm.201707543 (2018).

10 Fang, R. P. *et al.* More Reliable Lithium-Sulfur Batteries: Status, Solutions and Prospects. *Advanced Materials* **29**, doi:10.1002/adma.201606823 (2017).

11 Conder, J. *et al.* Direct observation of lithium polysulfides in lithium–sulfur batteries using operando X-ray diffraction. *Nature Energy* **2**, 17069, doi:10.1038/nenergy.2017.69 https://www.nature.com/articles/nenergy201769#supplementary-information (2017).

12 Cleaver, T., Kovacik, P., Marinescu, M., Zhang, T. & Offer, G. Perspective—Commercializing Lithium Sulfur Batteries: Are We Doing the Right Research? *Journal of The Electrochemical Society* **165**, A6029-A6033, doi:10.1149/2.0071801jes (2018).

13 Zhang, S. S. Liquid electrolyte lithium/sulfur battery: Fundamental chemistry, problems, and solutions. *Journal of Power Sources* **231**, 153-162, doi:https://doi.org/10.1016/j.jpowsour.2012.12.102 (2013).

14 Aurbach, D. *et al.* On the Surface Chemical Aspects of Very High Energy Density, Rechargeable Li-Sulfur Batteries. *Journal of the Electrochemical Society* **156**, A694-A702, doi:10.1149/1.3148721 (2009).

15 Park, K. & Goodenough, J. B. Dendrite-Suppressed Lithium Plating from a Liquid Electrolyte via Wetting of Li3N. *Adv Energy Mater* **7**, 1700732, doi:10.1002/aenm.201700732 (2017).

16 Zhang, S. S. A new finding on the role of LiNO3 in lithium-sulfur battery. *Journal of Power Sources* **322**, 99-105 (2016).

17 Chen, R., Zhao, T. & Wu, F. From a historic review to horizons beyond: lithium–sulphur batteries run on the wheels. *Chemical Communications* **51**, 18-33, doi:10.1039/C4CC05109B (2015).

18 Liang, X., Garsuch, A. & Nazar, L. F. Sulfur cathodes based on conductive MXene nanosheets for high-performance lithium–sulfur batteries. *Angewandte Chemie* **127**, 3979-3983 (2015).

19 Pang, Q., Liang, X., Kwok, C. Y. & Nazar, L. F. Advances in lithium–sulfur batteries based on multifunctional cathodes and electrolytes. *Nature Energy* **1**, 16132, doi:10.1038/nenergy.2016.132 (2016).

20 Pang, Q., Liang, X., Kwok Chun, Y., Kulisch, J. & Nazar Linda, F. A Comprehensive Approach toward Stable Lithium–Sulfur Batteries with High Volumetric Energy Density. *Adv Energy Mater* **7**, 1601630, doi:10.1002/aenm.201601630 (2016).

21 Rao, D. *et al. Mechanism on the Improved Performance of Lithium Sulfur Batteries with MXene-Based Additives*. Vol. 121 (2017).

22 Liu, X., Huang, J. Q., Zhang, Q. & Mai, L. Q. Nanostructured Metal Oxides and Sulfides for Lithium-Sulfur Batteries. *Advanced Materials* **29**, doi:10.1002/adma.201601759 (2017).

23 Fan, X., Sun, W., Meng, F., Xing, A. & Liu, J. Advanced chemical strategies for lithium–sulfur batteries: A review. *Green Energy & Environment* **3**, 2-19 (2018).

24 Qu, Q. *et al.* Strong Surface-Bound Sulfur in Conductive MoO2 Matrix for Enhancing Li–S Battery Performance. *Advanced Materials Interfaces* **2**, 1500048, doi:10.1002/admi.201500048 (2015).

25 Conder, J. & Villevieille, C. Is the Li–S battery an everlasting challenge for operando techniques? *Current Opinion in Electrochemistry* **9**, 33-40, doi:https://doi.org/10.1016/j.coelec.2018.03.029 (2018).

26 Zhang, X. Y., Verhallen, T. W., Labohm, F. & Wagemaker, M. Direct Observation of Li-Ion Transport in Electrodes under Nonequilibrium Conditions Using Neutron Depth Profiling. *Adv Energy Mater* **5**, 1500498, doi:ARTN 1500498 10.1002/aenm.201500498 (2015).

27 Verhallen, T. W., Lv, S. & Wagemaker, M. Operando Neutron Depth Profiling to Determine the Spatial Distribution of Li in Li-ion Batteries. *Frontiers in Energy Research* **6**, doi:10.3389/fenrg.2018.00062 (2018).

28 Wang, H., Downing, R. G., Dura, J. A. & Hussey, D. S. in *Polymers for Energy Storage and Delivery: Polyelectrolytes for Batteries and Fuel Cells* Vol. 1096 *ACS Symposium Series* Ch. 6, 91-106 (American Chemical Society, 2012).

29 Harks, P. P. R. M. L., Mulder, F. M. & Notten, P. H. L. In situ methods for Li-ion battery research: A review of recent developments. *Journal of Power Sources* **288**, 92-105, doi:https://doi.org/10.1016/j.jpowsour.2015.04.084 (2015).

30 Wang, J. *et al.* Profiling lithium distribution in Sn anode for lithium-ion batteries with neutrons. *Journal of Radioanalytical and Nuclear Chemistry* **301**, 277-284, doi:10.1007/s10967-014-3102-5 (2014).

31 Ziegler, J. F., Cole, G. W. & Baglin, J. E. E. Technique for determining concentration profiles of boron impurities in substrates. *Journal of Applied Physics* **43**, 3809-3815, doi:10.1063/1.1661816 (1972).

32 Whitney, S. M., Biegalski, S. R. F. & Downing, G. Benchmarking and analysis of 6Li neutron depth profiling of lithium ion cell electrodes. *Journal of Radioanalytical and Nuclear Chemistry* **282**, 173, doi:10.1007/s10967-009-0229-x (2009).

33 Singh, D. P., Mulder, F. M. & Wagemaker, M. Templated spinel Li4Ti5O12 Li-ion battery electrodes combining high rates with high energy density. *Electrochemistry Communications* **35**, 124-127, doi:https://doi.org/10.1016/j.elecom.2013.08.014 (2013).

34 Gustafsson, T., Thomas, J. O., Koksbang, R. & Farrington, G. C. The polymer battery as an environment for in situ X-ray diffraction studies of solid-state electrochemical processes. *Electrochimica Acta* **37**, 1639-1643, doi:https://doi.org/10.1016/0013-4686(92)80128-9 (1992).

35 Trask, S. E. *et al.* From coin cells to 400 mAh pouch cells: Enhancing performance of high-capacity lithium-ion cells via modifications in electrode constitution and fabrication. *Journal of Power Sources* **259**, 233-244, doi:https://doi.org/10.1016/j.jpowsour.2014.02.077 (2014).

36 Lv, S. *et al.* Operando monitoring the Lithium spatial distribution of Li-metal anodes. *Nature Communications*, in press (2018).

37 Zhang, X. *et al.* Rate-Induced Solubility and Suppression of the First-Order Phase Transition in Olivine LiFePO4. *Nano Letters* **14**, 2279-2285, doi:10.1021/nl404285y (2014).

38 Wang, D.-W. *et al.* Carbon–sulfur composites for Li–S batteries: status and prospects. *Journal of Materials Chemistry A* **1**, 9382-9394, doi:10.1039/C3TA11045A (2013).

39 Tang, S. & Zhao, H. Glymes as versatile solvents for chemical reactions and processes: from the laboratory to industry. *RSC Advances* **4**, 11251-11287, doi:10.1039/C3RA47191H (2014).

Chapter 4 Supporting information

Electrode fabrication:
Electrodes with and without LTO were prepared by the conventional slurry based process. The slurry was casted onto Aluminum foil current collectors using a doctor blade. After drying at 70˚C in the coating was dried further in a vacuum (0.01 bar) oven for 1h at 60 ˚C, a cross section of such an electrode is shown in **Fig. S4.1.** LTO membranes were prepared by mixing LTO and PVDF in a weight ratio of 85:15, without a conductive additive. This slurry was casted on a glass plate and subsequently immersed in demineralized water. This process forms a self-detaching and free-standing membrane. This membrane is then dried and stacked upon a standard carbon sulfur electrode, the two are not pressed or calendared to avoid electronic contact, a SEM image of the cross sections of the stack.

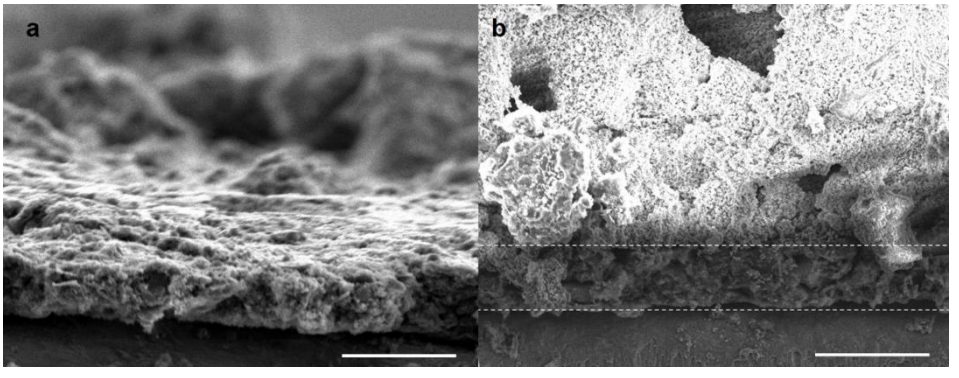

Figure S4.1. Scanning electron microscopy cross-sectional view of the electrodes on Al-foil applied in this study. a) A LTO + CS electrode, containing 10 w% LTO, and b) a CS electrode covered by an LTO membrane with the electrode region clarified by the dashed lines. The scale bars represent 10 µm.

Despite the high capacity and large volume change of sulfur (80%)[1] a constant energy to depth conversion is used, rationalized by the mere minor differences in the stopping power between the various constituents, see **Fig. S4.2**.

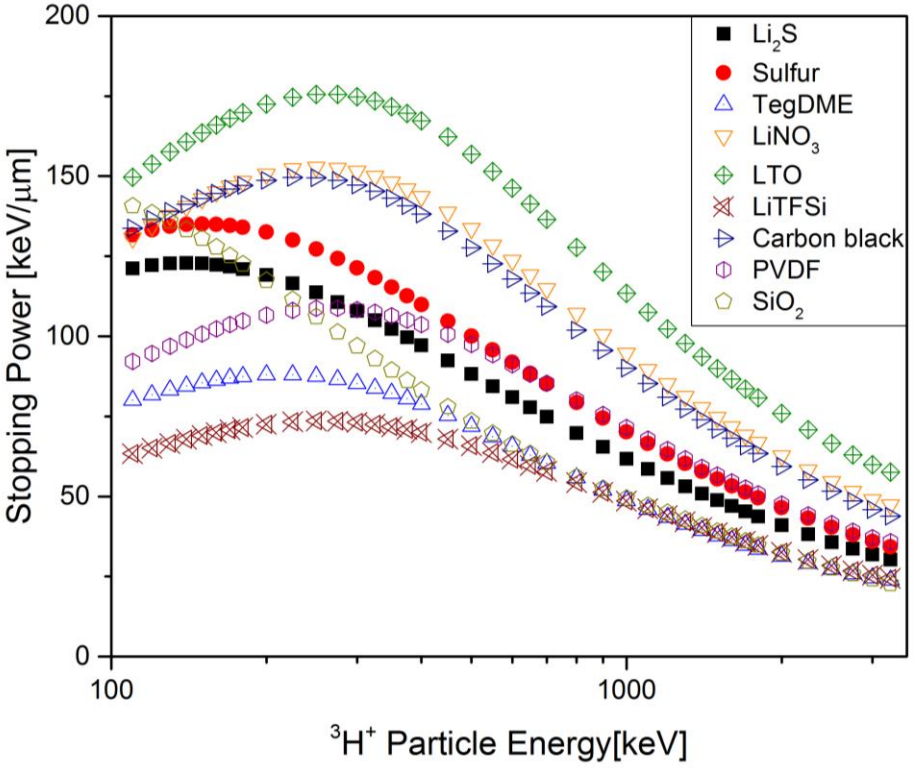

Figure S4.2 The stopping power of all cell constituents calculated using SRIM[2].

The standard cells, that is the CS electrode, which showed poor performance, especially in the first cycle. This result is, by itself, not enough to compare and deduce any beneficial properties or positive influence of the LTO membrane or LTO + CS electrode, however an interesting result was obtained when a cell was paused mid-discharge, while it was entering the second plateau, shown in **Fig. S4.3.**

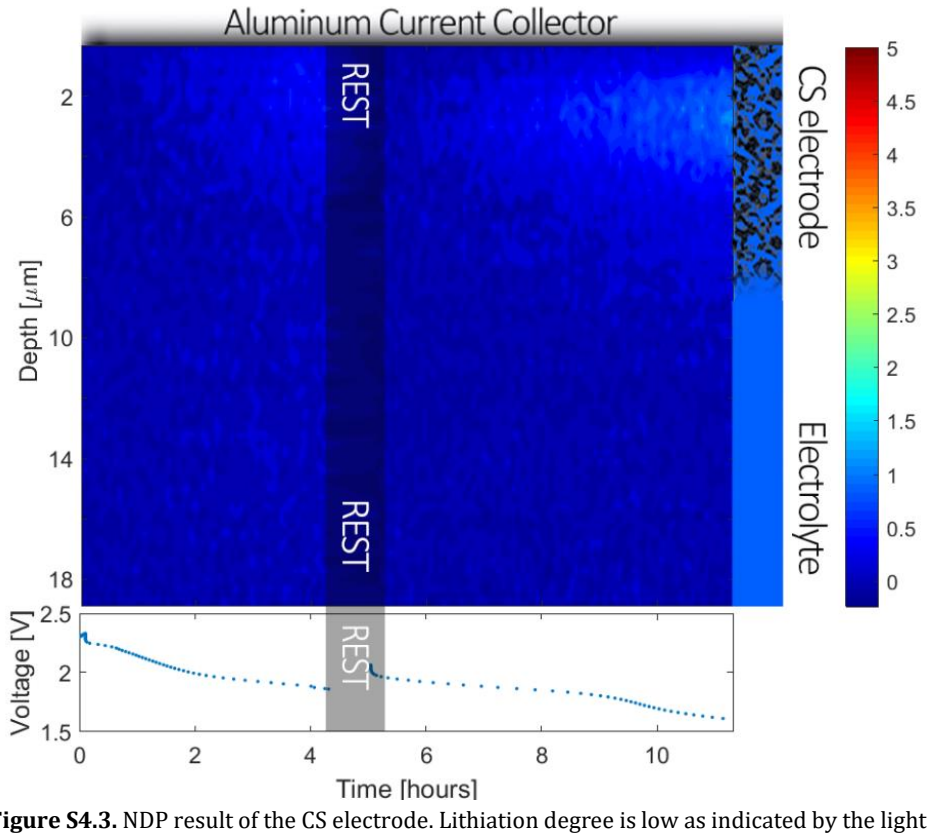

Figure S4.3. NDP result of the CS electrode. Lithiation degree is low as indicated by the light blue colors.

The first plateau ~2.4V was relatively short and the cell quickly entered the second plateau, after approximately 2 hours. Nonetheless the CS electrode is lithiated, whereas the comparable CS electrode+LTO membrane needs almost 8 hours to reach a similar concentration in the electrode. Hence it seems that the rapid voltage drop allows an earlier onset of solid sulfur deposition. However, when after 4 hours discharge was stopped and the cell was left to rest for 1 hour, the lithium concentration decreased. Indicating that lithium had left the measurement scope. This concentration increase and decrease might be explained by soluble polysulfide species diffusing slowly outward of the porous network, however this was not observed in the cells containing LTO additives. An alternative explanation could be that the solid deposits are re-dissolved with the aid of sulfide (S_8) rings from the available uncycled sulfur. This observation helps to explain the large experimental discrepancies in the reported onset of solid deposition[1, 3, 4, 5].

References

1. Wang D-W, *et al.* Carbon–sulfur composites for Li–S batteries: status and prospects. *Journal of Materials Chemistry A* 1, 9382-9394 (2013).

2. Ziegler JF, Ziegler MD, Biersack JP. SRIM - The stopping and range of ions in matter (2010). *Nuclear Instruments & Methods in Physics Research Section B-Beam Interactions with Materials and Atoms* 268, 1818-1823 (2010).

3. Zhao EY, *et al.* Advanced Characterization Techniques in Promoting Mechanism Understanding for Lithium-Sulfur Batteries. *Advanced Functional Materials* 28, (2018).

4. Zhang SS. Liquid electrolyte lithium/sulfur battery: Fundamental chemistry, problems, and solutions. *Journal of Power Sources* 231, 153-162 (2013).

5. Nelson J, *et al.* In Operando X-ray Diffraction and Transmission X-ray Microscopy of Lithium Sulfur Batteries. *Journal of the American Chemical Society* 134, 6337-6343 (2012).

5

Immersion Precipitation Route Towards High Performance Thick and Flexible Electrodes For Li-ion Batteries

This chapter has been published as PPRML Harks, CB. Robledo, C George, C Wang, T van Dijk, L Sturkenboom, HDW Roesink, FM Mulder, Journal of Power Sources, 10. 1016/j.jpowsour.2019.227200

Abstract

Enabling the transition to renewable power sources requires further optimization of batteries in terms of energy/power density and cost-effectiveness. Increasing the practical thickness of Li ion battery electrodes not only can improve energy density on cell level but reduces manufacturing cost. However, thick electrodes exhibit sluggish charge-transport kinetics and are mechanically less stable, typically resulting in substandard battery performance compared to the current commercial standards (~50 micron). Here we disclose a novel method based on immersion precipitation by employing a non-solvent to solidify the battery binder, instead of solvent evaporation. This method allows for the fabrication of thick and suitable density electrodes (>100 microns with ultra-high mass loading) offering excellent electrochemical performance and mechanical stability. Using commercial electrode active materials at a remarkable mass-loading of 24 mg cm^{-2}, the electrodes processed via immersion method are shown to deliver 3.5 mAh cm^{-2} at a rate of 2C and operate at rates up to 10C. As additional figure of merit, this method produces electrodes that are both stand-alone and highly flexible, which have been evaluated in flexible full-cells. Furthermore, via immersion precipitation the commonly used more toxic N-Methyl-2-pyrrolidone can be supplanted by environmentally benign dimethyl sulfoxide as solvent for processing electrode layers.

5.1 Introduction

Li-ion batteries (LIB) with high energy density and adequate power output are required to enable heavy-duty applications such as power tools, drones/robots, power storage from intermittent energy sources[1], and electric vehicles with optimal driving range. To put these in practice a rapid improvement in both battery energy/power density and cost-effectiveness is needed. A straightforward way to improve the energy density of batteries is to adopt thicker electrodes. This increases the energy density on the cell level and reduces the cost as it minimizes inactive components such as current collectors and separators, and requires only fewer layers to be processed (see **Fig. 5.1a,b**)[2, 3]. If one assumes doubling the electrode thickness from 50 to 100 μm, the increase in volumetric and gravimetric energy density (without considering the packaging) can be estimated to be ~ 16 and 20%, respectively (see Supporting Information). The cost reduction as a result of doubling the electrode thickness has been calculated to be in the range of 16 to 25%[2, 3]. However, there are two major hurdles en route to achieving operable thick battery electrodes. Firstly, the commercial LIB-electrodes are produced by coating a slurry that is prepared by mixing a liquid solvent, a polymeric binder, active material and conductive carbon on metal foils as current collector (Cu or Al). The slot-die coated metal foils are then dried and followed by roll-mill pressing. For

research purposes the method remains mostly unaltered, however often a doctor blade technique is used for casting[4]. Unfortunately, thick coatings are prone to form cracks due to high stress developed during drying, and tend to crumble away or detach from metal current collectors and mechanically weak electrodes are extremely difficult to process using roll-to-roll coaters. Consequently, these issues limit electrode thickness for this method to the maximum of 100 μm, where high-performance LIB electrodes in practice even have thinner electrodes of 50-60 μm[3, 5, 6]. In addition, the current process does not impart electrodes with sufficient mechanical strength and resilience for applications such as wearable electronics, bendable smart phones and medical implants. To date, the development of flexible electrodes relies heavily on the use of expensive and advanced carbon structures such as carbon nanotubes, nanofibers and graphene(oxide) to accommodate flexibility[7, 8].

Secondly, the diffusion limited ionic resistance increases exponentially with increasing thickness, leading to poor electrochemical performance and drastic reduction in both energy/power capabilities. In fact the extent to which electrodes can be thickened depends on whether battery performance still meets the power/energy requirements of the given application (e.g. portable electronics or electric vehicles). Therefore, unless considerable improvements on thick electrodes in terms of charge transport kinetics and mechanical integrity are achieved, it is highly unlikely to increase the energy density by increasing the thickness, without compromising the power density. This severely bottlenecks the fabrication of thick electrodes on commercial scale to date.

Surprisingly, research on the fabrication and optimization of thick electrodes is limited[9-16], let alone those that are capable of being self-supporting or flexible. Furthermore, much of battery materials research is conducted on thin and low mass-loading electrodes (~1mg cm^{-2}), which cannot be directly used to extrapolate and predict the performance of thick electrodes that are plagued by severe mechanical and charge transport issues[17-19]. It is therefore difficult to translate results based on low mass loadings into real-world batteries. Also, it is often not indicated whether such special methods and/or conductive additives adopted in research can actually make the fabrication of battery electrodes to be economically feasible and/or scalable.

In this work we present a versatile method for the fabrication of high performance thick and flexible electrodes by a phase inversion process, namely immersion precipitation. This process allows for the choice between substrate based (with current collectors) and self-supporting electrodes (stand-alone). To show the versatility of the method and its relevance to commercial battery electrodes, we tested electrodes produced by this method using commercial lithium

titanate ($Li_4Ti_5O_{12}$, or LTO), lithium iron phosphate (LFP) and lithium cobalt oxide (LCO) as active materials. The obtained electrodes are flexible, mechanically stable, and can easily be made thicker than current standards. Electrodes with a high mass-loading of 24 mg cm^{-2}, corresponding to a capacity of 4 mAh cm^{-2}, can be cycled at high C-rates.

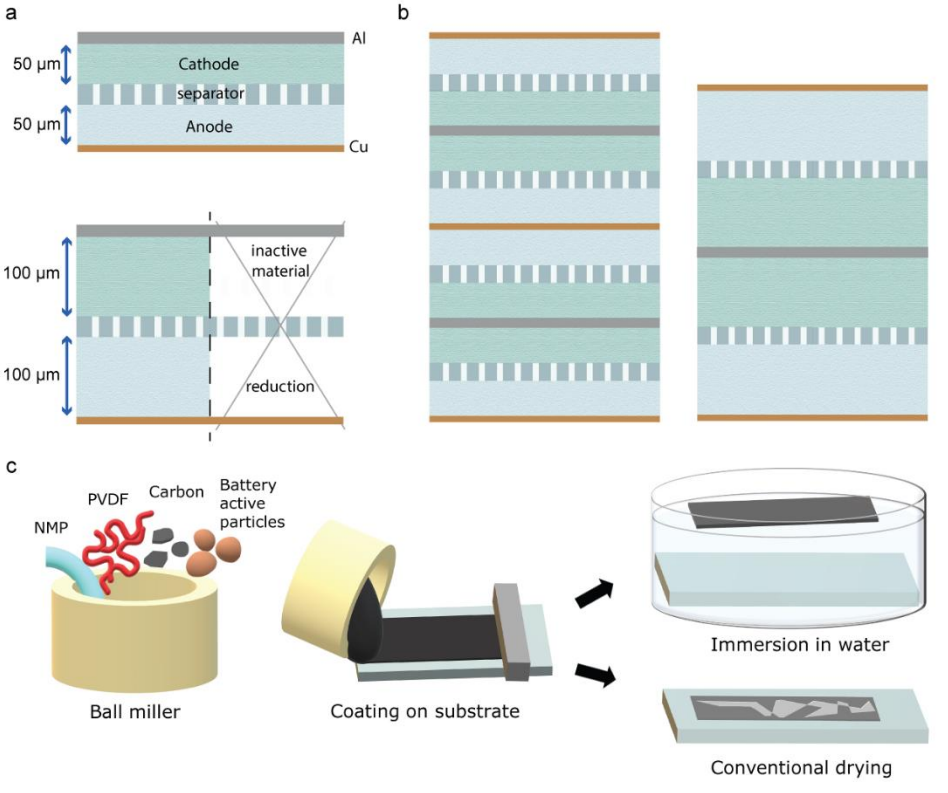

Fig. 5.1 Schematic representation of doubling battery electrode thickness. a) A conventional battery based on thin electrodes and a battery with the same theoretical capacity, but based on twice as thick electrodes, resulting in a reduction of inactive materials, and thus costs. b) The battery with two times thicker electrodes at the right has the same amount of active material in a smaller volume and with lower mass because of the lower number of current collectors and separators, needing a lower amount of layers to process. The components are drawn to scale; separator 25µm, Cu 9µm, Al 15µm. c) The fabrication of self-supporting electrodes using immersion precipitation.

5.2 Results and discussion

Phase inversion is the general term for a process of controlled polymer transformation from the dissolved liquid to solid precipitate phase. The method is

a well-established large-scale process to synthesize polymer membranes for diverse applications[20]. Conversely, with regard to battery electrodes the technique is seldom applied and publications on this topic are scarce[21-25]. Phase inversion is often achieved by immersion precipitation, also referred to as non-solvent induced phase separation. Here a polymer containing solution is casted on a suitable support and subsequently immersed in a coagulation bath containing a non-solvent for the polymer that mixes well with the polymer solvent. The exchange of the polymer solution and the non-solvent leads to a thermodynamically unstable system, causing liquid–liquid de-mixing. This typically results in a two-phase system, *i.e.*, a solid polymer-rich phase which solidifies through processes such as gelation, vitrification, or crystallization, resulting in the membrane structure, in which a liquid polymer-poor phase induces the formation of pores in the membrane. The kinetic aspects that play a role in immersion precipitation are mostly related to the exchange rate of solvent out of, and non-solvent into, the casting solution, which in turn is related to (non-)solvent molecule size, miscibility, and the viscosity of the coating. All these factors that affect the rate of polymer solidification ultimately determine the physical morphology of membranes formed by this method[20, 26].

We adopt this immersion precipitation in the conventional Li-ion electrode fabrication to achieve thick and flexible electrodes by introducing only a minor alteration of the conventional slurry casting method, in order to meet manufacturability compliance. Basically, the battery electrodes are made following the conventional slurry casting method, however, before the drying step the casted electrode is shortly submerged in a coagulation bath containing a non-solvent for the binder (**Fig. 5.1c**). This modification has surprising impact on the morphology and structural integrity of the obtained electrode. Electrodes produced by this method are over ~100 μm thick while being highly flexible, with no sign of cracking or delamination, an example is shown in **Fig. 5.2a**. Casting exactly the same slurry (as used in immersion method) but using a drying step to invert the phase of the binder, as is done traditionally, leads to a cracked and delaminated layer (**Fig. 5.2b**). This points to the beneficial effects of the coagulation step on the electrode's mechanical characteristics. This is better reflected by the fact that, after an extended period in the coagulation bath, the electrodes release themselves from the (sufficiently smooth) substrate as a self-supporting polymer bound film (**Fig. 5.2c** and **5.2d**).

Remarkable levels of mass loading (similar to commercial levels) can be achieved as the self-supporting electrodes can be casted to thicknesses of hundreds of microns. Alternatively, the electrodes can be processed relatively thin and conveniently stacked on top of each other to obtain the desired mass loading. **Fig.**

5.2e shows a cross-section of a typical self-supporting electrode with a binder content as low as 5wt% (this wt.% is close to industry standard) and these electrodes were used for the electrochemical measurements (inset of **Fig. 5.2e**). It can be observed that the electrode is characterized by a high porosity, while providing excellent interconnectivity between the individual electrode constituents, allowing the electrode to be substrate free.

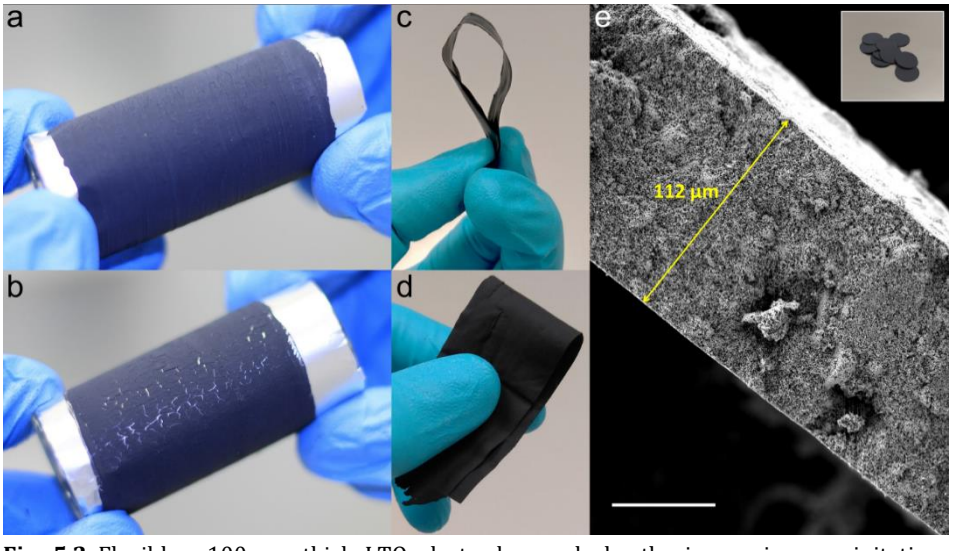

Fig. 5.2 Flexible ~100 µm thick LTO electrodes made by the immersion precipitation method. a) An electrode with 8 wt% binder on standard aluminum foil at a bending radius of 10 mm. Processing the same slurry by the conventional way of evaporating the solvent results in an extremely cracked and delaminated layer (b). c and d) A self-supporting, highly flexible electrode with 15 wt% binder. e) A SEM image of the cross-section of a self-supporting electrode with a binder content of 5 wt%, the scale bar represents 50 µm. These self-supporting electrodes were cut into 0.5 cm^2 disks (inset) and used in test cells.

To quantify the apparent difference in physical properties of both types of electrodes, tensile testing was performed. **Fig. S5.1** shows the stress-strain curve of an immersion precipitation LTO electrode with 5wt% PVDF and a thickness of 150 µm. The tensile strength amounts to 0.25 MPa at breaking point. This is quite remarkable since pure (100%) PVDF membranes fabricated through phase inversion processes are known to have a tensile strength of 2-5 MPa[27, 28]. On the contrary, when same slurry was used to make equally thick electrodes through the conventional drying technique, this yielded a cracked layer similar to the one depicted in **Fig. 5.2b**. The recovered cracked and brittle flakes have extremely poor mechanical integrity and could not be tested with that range of electrode thickness.

To reveal the origins of the enhanced mechanical integrity, a simple membrane, purely for imaging purposes, was made with both immersion and conventional methods, consisting of 95 wt% glassy carbon and 5 wt% polyvinylidene fluoride (PVDF). The reasons why we chose glassy carbon to reveal how PDVF is distributed across these electrodes are as follows. Firstly, they have spherical particles, and are relatively monodisperse, which allows for optimal discernibility of the binder phase. Secondly, it is extremely difficult to distinguish the PVDF network in the presence of LTO particles and Super P (**Fig. 5.2e**), which fill-up entire void space, making the visualization of PVDF almost impossible by scanning electron microscopy. Therefore, the glassy carbon and PVDF is the simplest but yet the most effective choice for demonstrating this. **Fig. 5.3** shows the cross sections and top views of both types of electrodes. Clearly, it can be observed that long-range cobweb like PVDF structures run throughout the immersion precipitated membrane (**Fig. 5.3b**), whereas in conventionally prepared films on Al substrates (**Fig. 5.3a**), no macroscopic PVDF networks or filaments were present. It is a general consensus that the dissolved polymer binder tends to adsorb onto battery materials (active particles and carbon) already in the slurry, i.e. before drying[29]. This process should thus occur for both methods. This binder layer on the electrode particles is able to glue neighboring particles together, i.e. forming connections on a small length scale, and seems to be the only mechanism occurring for the conventionally prepared membrane. The absence of binder or its scarce distribution across the conventionally prepared film can be further clarified by taking a look at the top of the electrode, where large aggregates of PVDF binder undergoing phase segregation/isolation can be observed. Energy dispersive X-ray spectroscopy mapping of fluorine was used to confirm the large PVDF particles (**Fig. S5.2**). This upward binder diffusion during drying is often observed in the conventional method (be it to a lesser extent than in our glassy carbon membrane used here for imaging clarity)[30, 31]. The quick inversion of the binder via the immersion precipitation technique can overcome this problem by severely limiting the time for the binder to diffuse, and thus produces a homogeneous distribution of polymeric filaments throughout electrodes. Due to the ineffective precipitation of the non-adsorbed binder that occurs during drying, the ability of battery particles to glue each other at larger length scales is severely diminished, explaining the brittle nature of conventional electrodes. Conversely, during the immersion method the surplus of polymer in solution tends to precipitate as cobweb like structures, well distributed throughout the film, which, in addition to the adsorbed binder layer on the battery particles, results in a flexible layer with excellent interparticle connection. We remark that only a small fraction of PVDF is adsorbed on the particles and therefore much of it still in solution during drying, perhaps more than

in a typical slurry containing also a carbon additive. It is probably caused by the limited affinity between glassy carbon and PVDF, or simply due to the small surface area of the smooth and relatively large particles. Nevertheless these experiments unambiguously establish that the distribution and secondary morphology of PVDF binder within electrodes for the two methods determine their mechanical integrity and resilience. Especially, even for materials with limited binder adsorption, immersion precipitation, as opposed to the conventional method, is able to produce flexible membranes with a homogeneous binder distribution.

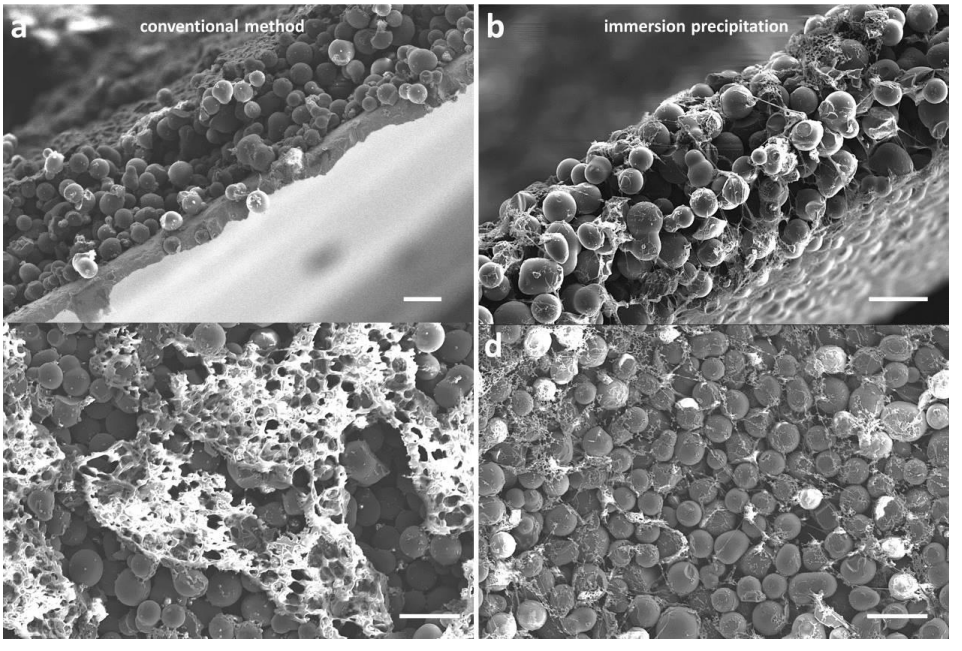

Fig. 5.3 Scanning electron microscopy images of 95 wt% glassy carbon membranes (5 wt% PVDF). Side-view (a) and top-view (c) of a conventionally prepared membrane on Al-foil. Side-view (b) and top-view (d) of a self-supporting membrane via immersion precipitation. The scale bars represent 20 μm.

As a next step we fabricated both half and full cells with the thick and flexible LTO electrodes to assess their electrochemical performance. First, as control experiments, LTO electrodes with an active mass loading of 1.5 mg cm^{-2} (0.26 mAh cm^{-2}) were tested, which is a typical mass-loading adopted in lab-scale research purposes. **Fig. S5.3** in the supporting information shows the rate capability and cycle life tests. The electrodes are able to retain 25% of their initial capacity at a very high rate of 100C and their capacity loss is only 3% over 1000 cycles at a 5C charge and discharge rate, delivering around 140 mAh g^{-1}. The overall electrochemical performance of these electrodes is comparable to literature

reports that exploit more sophisticated techniques and materials[32-35], however, as discussed earlier, such low mass loadings have little-to-no relevance with respect to commercial applications. Commercial battery electrodes typically have capacities around 2 mAh cm^{-2} or higher, and an active material loading of at least 90 wt%.

To demonstrate the potential of immersion precipitation for commercial application, self-supporting electrodes consisting of 90 wt% active material, 5 wt% conductive carbon, and 5 wt% binder were prepared with a LTO mass-loading of 24 mg cm^{-2} (4.2 mAh cm^{-2}). **Fig. 5.4a** shows the rate capability of such a high mass loading electrode. At rates that are critical for practical application (0.5 to 2C required for electric vehicles and power tools), it shows excellent performance. In this range the electrode delivers a high capacity in excess of 3.5 mAh cm^{-2}. It is important to assess whether this capacity is attained in an energy efficient way, and therefore the voltage curves as a function of specific capacity are shown in **Fig. 5.4b**. At 2C the LTO electrode still delivers 140 mAh g^{-1}, about 80% of its theoretical specific capacity (175 mAh g^{-1}). In terms of over-potentials, the difference between the output and equilibrium voltage of the cell, it is important to consider that the associated ohmic heating would cause the battery temperature to increase. However, at increased temperature the ionic conduction improves, which in turn lowers the over-potential and thus the losses. To test the degree to which this effect takes place on electrodes prepared via immersion precipitation, temperature dependent cycling measurements were carried out, which are shown in **Fig. 5.4c**. With LTO being an anode (low-voltage) material it is important to focus on the discharge (lithiation) of the electrode, as this would correspond to the charging process in a full cell, which is required to proceed quickly. The discharge was conducted at 2C (corresponding to a full charge in 30 minutes). When the battery temperature was increased from 25 to 45°C, the over-potentials decreased more than 40%, which indicates reduced efficiency losses. Assuming an operating temperature of max 45°C, a charge rate of 2C to 80% of an 80kWh battery and an over-potential of 0.11V at a cell potential of 3.5V, one would need to cool away an amount of heat losses of 4 kWh (see Supporting Information). Such cooling amount appears practically feasible.

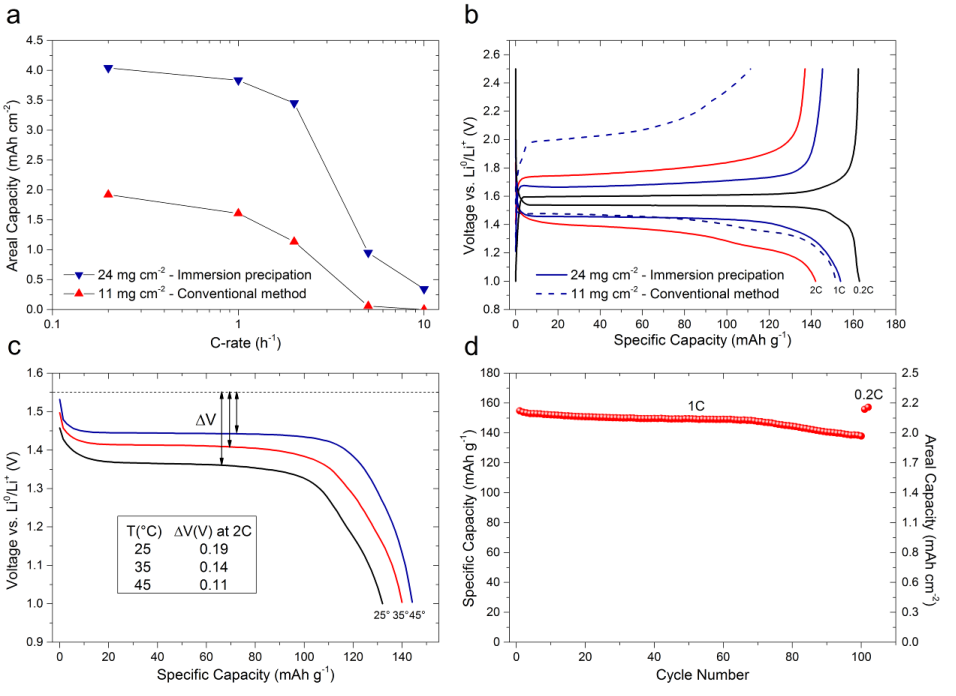

Fig. 5.4 Electrochemical testing of high mass-loading LTO electrodes. a) Apparent areal capacity as a function of C-rate. b) Voltage curves as a function of specific capacity for various C-rates. c) Voltage curves as a function of specific capacity of a 24 mg cm^{-2} electrode cycled at 2C, with the difference in equilibrium and discharge voltage indicated at half state-of-charge. d) Cycle performance at a rate of 1C of an electrode with a mass-loading of 14 mg cm^{-2}.

To compare electrodes via immersion precipitation with standard electrodes, the same slurry (as in the immersion method) was used to prepare electrodes as in the conventional way (drying method). First of all, the electrodes had to be casted relatively thin in order to obtain an acceptable level of structural integrity that allows for the fabrication of electrodes and testing. In principle it is possible to cast slurries to obtain same electrode thickness as that of immersion method but electrodes showed increased tendency to delaminate and crumble away. Solvent evaporation in the conventional method causes a larger proportion of binder to leave the active particles behind and to precipitate at the top of electrodes, which further aggravates the problem of binder deficiency across the bulk electrodes, leading to coatings with poor mechanical properties. The dried electrodes had a thickness of 80 µm before calendaring and an areal mass loading of 11 mg cm^{-2}. Strikingly, having only less than half of the areal mass loading (compared to 24 mg

cm^{-2}), these electrodes show similar or even more dependency on the (dis)charge rate (**Fig. 5.4a**) and greater over-potentials than the high-mass loading electrode prepared via immersion precipitation. Especially during charging the over-potentials were much larger than those of the much heavier counterpart. Already at 1C the electrode cannot be fully charged (dashed line **Fig. 5.4b**). At the high cycle rates (5 to 10C) an abrupt drop in performance is observed for both electrodes. At such high current densities the Li-ion transport through the electrolyte becomes a severe limiting factor[10, 11, 36]. However the mere fact that the immersion precipitation electrodes can still be cycled at these rates is significant. For comparison, very recently Elango et al.[15] have proposed an interesting route to achieve electrode thickness as high as 1000 microns by combining spark plasma sintering and salt templating. As expected, rate performance tests showed that while the capacity of LFP based electrodes dropped close to zero at 2C, LTO based electrodes reached almost zero capacity at 1C, attributed to poor charge transport across electrodes. Despite the high energy density these thick electrodes can pack, they are not suitable for high-power applications for example electric vehicles.

To test the cycle stability, a high mass-loading electrode of 14 mg cm^{-2} was cycled at 1C (**Fig. 5.4d**). The electrode exhibits a very stable capacity for 70 cycles, after which it shows only a slight decline. After 100 cycles the electrode still has a specific capacity of almost 140 mAh g^{-1} which is 90% of the initial capacity. After 100 cycles at 1C, the C-rate was lowered to 0.2C. At the lower cycle rate the initial capacity is again achieved, indicating the kinetic origin of the observed fractional decrease. The decline is for the largest part related to the degradation of the Li anode of the half-cell, as the development of solid electrolyte interface and dendrites with every cycle is very large due to the high areal capacity of the tested electrode[18]. In the Supporting Information (**Fig. S5.4**) we show for a cell with similar mass loading that by replacing the Li anode most of the 'lost' reversible capacity can be recovered.

It is important to note that the conventionally prepared electrodes had to be compacted (equivalent to calendaring) in order to improve their performance, whereas the electrodes via immersion precipitation can be used as prepared. Even though in this work the calendaring procedure for conventional electrodes was not optimized and therefore maximum performance most likely was not yet achieved, it still provides sufficient insights into how critical this calendaring step is for conventional electrodes, whereas for immersion precipitation electrodes it is a non-factor. This is especially surprising as electrodes obtained through the immersion precipitation process are typically characterized by a relatively high porosity[21]. Such a degree of porosity (>40%) in conventional battery electrodes often means poor inter-particle connectivity and consequently has a negative effect on their

electronic conductivity and thus their performance[37, 38]. Increasing the porosity can be a strategy to improve the performance of an electrode as it would result in a larger electrode/electrolyte interface for charge transfer and a better ability to accommodate volume changes of the active material during cycling[39]. This strategy can thus be pursued with the immersion precipitation electrodes, as high porosity can be achieved without compromising the inter-connectivity of the electrode particles. However, from practical application standpoint an optimal volumetric capacity is desired. This means the electrode porosity should be minimized to the point where the performance of the electrode still meets the requirement of the application. Remarkably, a compressed phase inversion LTO electrode with a porosity of only 32% and a mass loading of approximately 20 mg cm^{-2} showed only a moderate decrease in rate capability compared to its 67% porous counterpart (**Fig. S5.5**, Supporting Information).

The excellent performance of the immersion precipitated electrodes might be partly explained by the enhanced particle interconnectivity, which facilitates good electronic conductivity everywhere throughout the film. Indeed, the DC electrical resistance of immersion electrodes is 37% lower than a conventional electrode with the same mass loading (**Table S5.1**). However at the high current densities applied in this study, the ionic transport through the porous electrode would still be a limiting factor[10, 11]. This is supported by the large decrease in polarization at higher temperatures (**Fig. 5.4c**) due to the decrease of the ionic resistivity of the electrolyte, whereas the electronic resistance is less temperature dependent. Therefore the enhanced performance should (for the larger part) be a result of an increased ionic transport in the electrode, which in turn is associated with the pore morphology. Ionic effects such as charge transfer resistance and ion diffusivity are reflected in the impedance of the electrode at lower and midrange frequencies[40]. Electrochemical impedance spectroscopy confirms an overall lower impedance in this range for the electrodes made via immersion precipitation (**Fig. S5.6**), which proves that immersion electrodes offer better ionic conductivity. Also, the Low DC resistance and Impedance of electrodes prepared via immersion is indicative of optimal degree of PVDF crystallization, combined with its uniform distribution across electrodes, and therefore immersion method provides a novel solution for uneven binder distribution and high degree of crystallization that can lead to high electrode impedance. While the SEM images (**Fig. 5.1**) offered the first glimpse of porosity and interconnectivity in immersion electrodes, more light can be shed on the porous networks formed within both types of electrodes (immersion and conventional) by conducting mercury intrusion porosimetry. **Fig. S5.7** shows the intrusion and extrusion of mercury as a function of pore diameter (applied pressure). Based on the volume of mercury that could infiltrate the films, their

porosity is deduced to be ~60%, which is consistent with their apparent porosity based on their geometry and density. Both electrodes have very similar pore size distribution, ranging between 100-300 nm, characterized by a steep increase in mercury intrusion. However upon extrusion the conventional electrode shows large hysteresis. This is associated with a non-uniform pore shape and/or a poorer interconnectivity of the pores[41]. This is also reflected in the pore tortuosity and permeability measured by this method. The electrode via immersion precipitation shows a ~20% lower tortuosity (2.05 vs. 2.53) and its permeability is 2.5 times higher than the conventional electrode (91625 vs. 35307 mdarcy), which explains its enhanced ionic transport. The origin may lie in the fact that during phase inversion the non-solvent diffuses all the way through the film, from the top to the bottom, which leaves long and connected pores stretching across the whole film, whereas for conventional electrodes their pore structure is based upon much more random processes that occur during the (slow) removal of the solvent as a vapor. We had used higher % binder (8 or 15 wt %) only to demonstrate that even such high binder concentration the electrodes have exceptional mechanical properties such as crack-free (>100 um) layers and ultra-flexible self-supporting electrodes. This cannot be achieved via conventional method where the same binder % leads to severe cracks and delamination and poor quality coating. Especially when the mass loading is very high due to the doubling electrode thickness, there needs to be much higher amount of binder but they should be highly networked and evenly distributed throughout electrodes to impart a high degree of mechanical flexibility and resilience (in particular for flexible electrode applications). Lower binder (5%), which is close to industrial standard, can also be administered in thick electrodes for standard batteries. Practically in lab-scale battery studies ~10% binder content in electrodes is very common, which is almost double that of commercial electrodes, but then the actual mass loadings is typically 1 to 2 mg cm^{-2}, which is at least 10 times smaller than that of commercial electrodes. In our studies, we have achieved a well-balanced recipe using immersion method for producing high-performance thick electrodes (with low binder) for standard batteries and ultra-flexible thick electrodes that can have either commercial level binder or more for special proposes. This of course involves a trade-off between energy density and electrode mechanical flexibility.

We further emphasis that the immersion precipitation method for battery electrodes is by no means limited to LTO[21]. Electrochemical tests of LFP and LCO electrodes and LTO-LFP full cells are supplied in the Supporting Information, **Fig. S5.8** and **Fig. S5.9**, respectively. As a proof of concept we fabricated a flexible LTO-LFP pouch-cell (1 mAh cm^{-2}), shown in **Fig. 5.5**. The flexible battery is able to power a red light emitting diode (LED) even when it is completely folded (bending angle

~180°), and during battery bent (to full folding) and flat stages the LED showed no change in intensity.

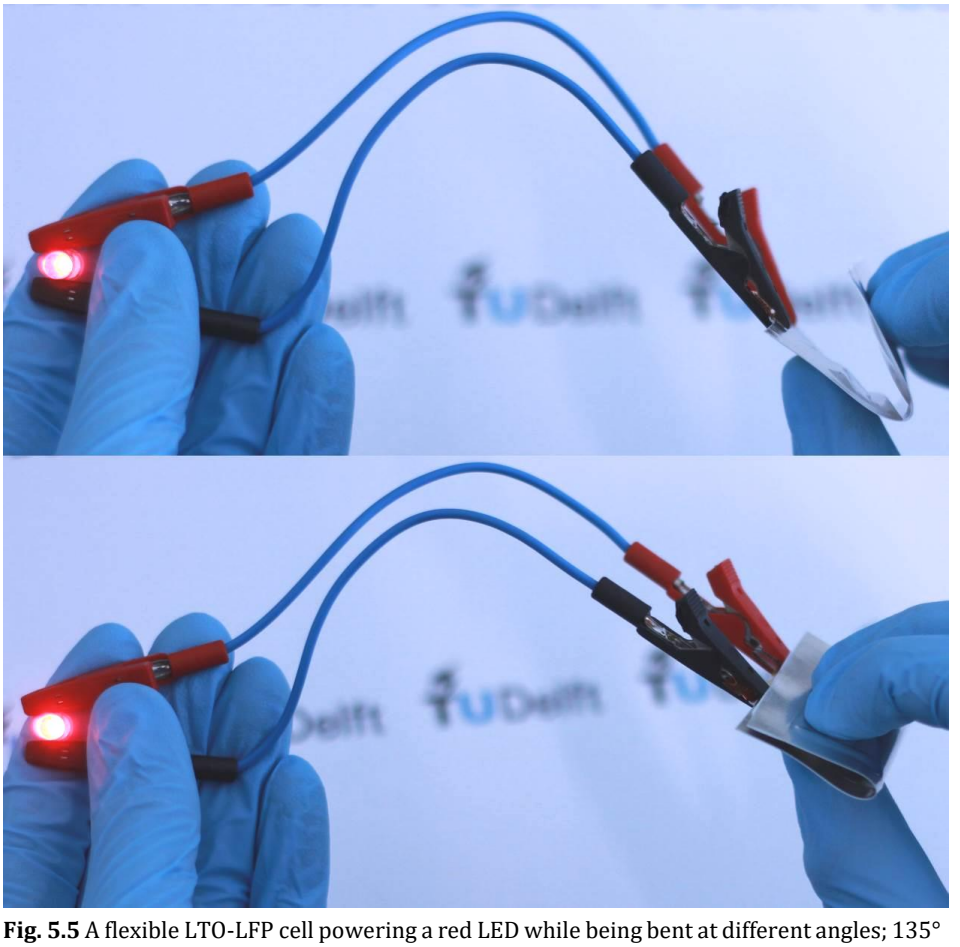

Fig. 5.5 A flexible LTO-LFP cell powering a red LED while being bent at different angles; 135° (top), and 180° (bottom).

In terms of solvent-binder combinations, N-methyl-2-pyrrolidone (NMP) and PVDF were used in this study, as it is the most widely applied solvent-binder combination for Li-ion electrodes. However, the commonly used polymers besides PVDF such as carboxymethyl cellulose and styrene-butadiene rubber have convenient non-solvents available that are miscible with their standard solvents, which suggests that they are applicable for immersion precipitation. In particular, because the widely used NMP is carcinogenic we tested the compatibility of this immersion process with dimethyl sulfoxide (DMSO) that is a relatively green solvent instead of NMP. **Fig. S5.10** in the Supporting Information compares the rate performance of

electrodes processed using these two solvents. The electrodes showed almost identical performance, which indicates that DMSO can be used as effectively as NMP with the method presented in this paper. Being able to replace more toxic NMP by DMSO for electrode fabrication would be a great improvement in terms of safety and environmental impact.

In conclusion, we presented a simple, potentially low-cost method based on immersion precipitation to fabricate both thick (over 100 micron) and flexible (self-supporting) electrodes without compromising the energy/power density. Owing to the unique porous structures with low tortuosity and high permeability and excellent interconnectivity of active particles facilitated by this immersion method, the thick electrodes still offer excellent electrochemical performance, in particular at rates (0.5-2C) that are required for enabling high power applications. For example, electrodes containing commercial LTO were tested with a high mass-loading of 24 mg cm^{-2}, achieving a capacity of ~4 mAh cm^{-2} at 1C and operate at rates up to 10C. Furthermore flexible full cells (with LTO and LFP) were shown to be fully operational while they were folded at a bending angle ~180°. This method can be extended to many combinations of binders, electrode materials and (non-)solvents for achieving both ultra-thick and flexible electrodes. Our findings point to a new way for developing high performance standard batteries with thick electrodes, and thus improved energy density, as well as highly flexible electrodes without needing special additives.

5.3 Methods

Electrode fabrication by immersion precipitation. First, PVDF (Sigma Aldrich) and either NMP (Sigma Aldrich) or DMSO (sigma Aldrich), were mixed in a planetary ball mill. The mass ratio of PVDF:solvent ranged from 1:10 to 1:20. Then, commercial LTO (particle size ~150 nm, Süd-Chemie) or LFP (carbon coated particles 140 nm, Phostech) or LCO (Sigma Aldrich) powder and carbon black Super P (Timcal) were added and mixed, to obtain a viscous, paste-like, slurry. Subsequently, the slurry was casted on aluminum foil or a glass plate by a doctor blade technique and immersed in a water bath. The Al-foil based electrodes were immersed for a few seconds. The short period of time in contact with water is sufficient to induce the phase inversion but does not cause delamination. The electrodes casted on glass were immersed for a longer period of time (approximately 1 minute) after which they spontaneously released, yielding a flexible self-supporting membrane. **Fig. 5.1c** shows a schematic representation of this procedure. The electrodes were not compressed, unless otherwise stated. The electrochemical measurements in this work were performed on self-supporting electrodes with a mass ratio of 90:5:5, active materials, Super P, PVDF, respectively.

The (apparent) porosity was calculated based on the geometry and weight of the electrodes and the density of the constituents, and ranged from 60-67% for non-calendared electrodes.

Electrode characterization. The morphology of the electrodes was examined with a JEOL JSM-IT100 scanning electron microscope, operating at an acceleration voltage of 5 kV.
Impedance spectroscopy was executed with an Autolab PGSTAT302N, for frequencies ranging from 10^6 to 0.1 Hz, with an AC signal of 10 mV. The DC resistance was obtained through Ohms law, by placing the electrodes between two metal connectors and measuring the current when applying 0.1V.
Tensile strength measurements were performed with a TA Instruments DMA Q800, with a displacement of 100 μm/min.
The porosity was investigated by mercury intrusion porosimetry with a Micrometrics PoroSizer 9320 applying a maximum intrusion pressure of 207MPa. In addition to the pore volume and pore size distribution, the permeability was obtained by using an empirical correlation established by Katz et al.[42, 43] which relates permeability to a critical pore diameter. The critical pore diameter is obtained by identifying the first inflection point on the steeply rising range of the intrusion curve. This point corresponds closely to the pore size at which mercury first finds a path spanning the sample. The samples were coarse powders, scraped off the aluminum current collector or fragmented self-supporting films. The measured inter particle volume (pore sizes > 100 um) was discarded and not shown.

Electrochemical measurements. Prior to measurements, the electrodes were dried at 80°C in a vacuum oven overnight. The employed electrochemical cells were purpose-built prototypes consisting of two stainless steel vacuum flanges, described elsewhere[25]. The cells were assembled inside an Ar filled glovebox with oxygen and water content less than 1 ppm. Lithium foil was used as the counter and reference electrode, combined with a glass fiber (Whatman) separator and the working electrodes to make up the cell. As electrolyte a solution of 1M $LiPF_6$ in ethylene carbonate and dimethyl carbonate (1:1 by volume) was used. To make flexible batteries, pouch cells were used. In brief, the electrodes were placed on a piece of aluminum foil (connected to the lug). After wetting with electrolyte, the electrode adheres to the metal foil, and after evacuating and sealing the cell, the components are compressed due to the pressure difference. The galvanostatic cycling experiments were performed with a programmable Maccor 4000 series

galvanostat. The cells were discharged to 1 V and charged to 2.5 V vs. Li^+/Li^0 at various C-rates (1C = 175 mA g^{-1}).

References

1. Mulder, F.M. Implications of diurnal and seasonal variations in renewable energy generation for large scale energy storage. *Journal of Renewable and Sustainable Energy* 6, 033105 (2014).
2. Patry, G., Romagny, A., Martinet, S. & Froelich, D. Cost modeling of lithium-ion battery cells for automotive applications. *Energy Science & Engineering* 3, 71-82 (2015).
3. Wood, D.L., III, Li, J. & Daniel, C. Prospects for reducing the processing cost of lithium ion batteries. *Journal of Power Sources* 275, 234-242 (2015).
4. Kraytsberg, A. & Ein-Eli, Y. Conveying Advanced Li-ion Battery Materials into Practice The Impact of Electrode Slurry Preparation Skills. *Adv. Energy Mater.* 6, 1600655 (2016).
5. Vlad, A., Singh, N., Galande, C. & Ajayan, P.M. Design Considerations for Unconventional Electrochemical Energy Storage Architectures. *Adv. Energy Mater.* 5, 1402115 (2015).
6. Singh, M., Kaiser, J. & Hahn, H. Thick Electrodes for High Energy Lithium Ion Batteries. *Journal of the Electrochemical Society* 162, A1196-A1201 (2015).
7. Liu, W., Song, M.S., Kong, B. & Cui, Y. Flexible and Stretchable Energy Storage: Recent Advances and Future Perspectives. *Adv. Mater.* 29, 1603436 (2017).
8. Ahmad, S., Copic, D., George, C. & De Volder, M. Hierarchical Assemblies of Carbon Nanotubes for Ultraflexible Li-Ion Batteries. *Advanced Materials* 28, 6705-+ (2016).
9. Bae, C.J., Erdonmez, C.K., Halloran, J.W. & Chiang, Y.M. Design of Battery Electrodes with Dual-Scale Porosity to Minimize Tortuosity and Maximize Performance. *Adv. Mater.* 25, 1254-1258 (2013).
10. Gallagher, K.G. et al. Optimizing Areal Capacities through Understanding the Limitations of Lithium-Ion Electrodes. *Journal of the Electrochemical Society* 163, A138-A149 (2016).
11. Du, Z., Wood, D.L., Daniel, C., Kalnaus, S. & Li, J. Understanding limiting factors in thick electrode performance as applied to high energy density Li-ion batteries. *Journal of Applied Electrochemistry* 47, 405-415 (2017).
12. Sander, J.S., Erb, R.M., Li, L., Gurijala, A. & Chiang, Y.M. High-performance battery electrodes via magnetic templating. *Nature Energy* 1 (2016).
13. Singh, D.P., Mulder, F.M., Abdelkader, A.M. & Wagemaker, M. Facile Micro Templating LiFePO4 Electrodes for High Performance Li-Ion Batteries. *Adv Energy Mater* 3, 572-578 (2013).
14. Singh, D.P., Mulder, F.M. & Wagemaker, M. Templated spinel Li4Ti5O12 Li-ion battery electrodes combining high rates with high energy density. *Electrochemistry Communications* 35, 124-127 (2013).
15. Elango, R., Demortière, A., De Andrade, V., Morcrette, M. & Seznec, V.C. Thick Binder-Free Electrodes for Li–Ion Battery Fabricated Using Templating Approach and Spark Plasma Sintering Reveals High Areal Capacity. *Adv. Energy Mater.*, 1703031 (2018).

16. Wei, T.S., Ahn, B.Y., Grotto, J. & Lewis, J.A. 3D Printing of Customized Li-Ion Batteries with Thick Electrodes. *Advanced Materials* 30 (2018).
17. Gogotsi, Y. & Simon, P. True Performance Metrics in Electrochemical Energy Storage. *Science* 334, 917-918 (2011).
18. Nitta, N. & Yushin, G. High-Capacity Anode Materials for Lithium- Ion Batteries: Choice of Elements and Structures for Active Particles. *Particle & Particle Systems Characterization* 31, 317-336 (2014).
19. Dillon, S.J. & Sun, K. Microstructural design considerations for Li-ion battery systems. *Current Opinion in Solid State & Materials Science* 16, 153-162 (2012).
20. Guillen, G.R., Pan, Y., Li, M. & Hoek, E.M.V. Preparation and Characterization of Membranes Formed by Nonsolvent Induced Phase Separation: A Review. *Industrial & Engineering Chemistry Research* 50, 3798-3817 (2011).
21. Yang, X. et al. Phase Inversion: A Universal Method to Create High-Performance Porous Electrodes for Nanoparticle-Based Energy Storage Devices. *Adv. Funct. Mater.* 26, 8427-8434 (2016).
22. Zhang, S.S. & Tran, D.T. A proof-of-concept lithium/sulfur liquid battery with exceptionally high capacity density. *Journal of Power Sources* 211, 169-172 (2012).
23. Byrd, I., Chen, H., Webber, T., Li, J.L. & Wu, J. Self-assembled asymmetric membrane containing micron-size germanium for high capacity lithium ion batteries. *Rsc Advances* 5, 92878-92884 (2015).
24. Byrd, I. & Wu, J. Asymmetric Membranes Containing Micron-Size Silicon for High Performance Lithium Ion Battery Anode. *Electrochimica Acta* 213, 46-54 (2016).
25. Harks, P.P.R.M.L., Robledo, C.B., Verhallen, T.W., Notten, P.H.L. & Mulder, F.M. The Significance of Elemental Sulfur Dissolution in Liquid Electrolyte Lithium Sulfur Batteries. *Adv. Energy Mater.* 7, 1601635 (2017).
26. Holda, A.K. & Vankelecom, I.F.J. Understanding and guiding the phase inversion process for synthesis of solvent resistant nanofiltration membranes. *Journal of Applied Polymer Science* 132 (2015).
27. Zhang, W.B. et al. Superhydrophobic and Superoleophilic PVDF Membranes for Effective Separation of Water-in-Oil Emulsions with High Flux. *Advanced Materials* 25, 2071-2076 (2013).
28. Jung, J.T. et al. Understanding the non-solvent induced phase separation (NIPS) effect during the fabrication of microporous PVDF membranes via thermally induced phase separation (TIPS). *Journal of Membrane Science* 514, 250-263 (2016).
29. Wenzel, V., Nirschl, H. & Notzel, D. Challenges in Lithium-Ion-Battery Slurry Preparation and Potential of Modifying Electrode Structures by Different Mixing Processes. *Energy Technology* 3, 692-698 (2015).
30. Su, F.Y. et al. Micro-structure evolution and control of lithium-ion battery electrode laminate. *Journal of Energy Storage* 14, 82-93 (2017).
31. Westphal, B.G. & Kwade, A. Critical electrode properties and drying conditions causing component segregation in graphitic anodes for lithium-ion batteries. *Journal of Energy Storage* 18, 509-517 (2018).
32. Coelho, J. et al. Lithium Titanate/Carbon Nanotubes Composites Processed by Ultrasound Irradiation as Anodes for Lithium Ion Batteries. *Sci Rep* 7 (2017).

33. Yao, Z. et al. Smart Construction of Integrated CNTs/Li4Ti5O12 Core/Shell Arrays with Superior High-Rate Performance for Application in Lithium-Ion Batteries. *Advanced Science*, 1700786 (2018).
34. Jia, X., Lu, Y. & Wei, F. Confined growth of Li4Ti5O12 nanoparticles in nitrogen-doped mesoporous graphene fibers for high-performance lithium-ion battery anodes. *Nano Res.* 9, 230-239 (2016).
35. Xie, J., Harks, P., Li, D.J., Raijmakers, L.H.J. & Notten, P.H.L. Planar and 3D deposition of Li4Ti5O12 thin film electrodes by MOCVD. *Solid State Ion.* 287, 83-88 (2016).
36. Zheng, H.H., Li, J., Song, X.Y., Liu, G. & Battaglia, V.S. A comprehensive understanding of electrode thickness effects on the electrochemical performances of Li-ion battery cathodes. *Electrochimica Acta* 71, 258-265 (2012).
37. Fongy, C., Gaillot, A.C., Jouanneau, S., Guyomard, D. & Lestriez, B. Ionic vs Electronic Power Limitations and Analysis of the Fraction of Wired Grains in LiFePO4 Composite Electrodes. *Journal of the Electrochemical Society* 157, A885-A891 (2010).
38. Orikasa, Y. et al. Ionic Conduction in Lithium Ion Battery Composite Electrode Governs Cross-sectional Reaction Distribution. *Sci Rep* 6 (2016).
39. Vu, A., Qian, Y.Q. & Stein, A. Porous Electrode Materials for Lithium-Ion Batteries - How to Prepare Them and What Makes Them Special. *Adv. Energy Mater.* 2, 1056-1085 (2012).
40. Sun, X.C. et al. Structure and Electrochemical Properties of Spinel Li4Ti5O12 Nanocomposites as Anode for Lithium-Ion Battery. *International Journal of Electrochemical Science* 9, 1583-1596 (2014).
41. Giesche, H. Mercury porosimetry: A general (practical) overview. *Particle & Particle Systems Characterization* 23, 9-19 (2006).
42. Katz, A.J. & Thompson, A.H. QUANTITATIVE PREDICTION OF PERMEABILITY IN POROUS ROCK. *Physical Review B* 34, 8179-8181 (1986).
43. Katz, A.J. & Thompson, A.H. PREDICTION OF ROCK ELECTRICAL-CONDUCTIVITY FROM MERCURY INJECTION MEASUREMENTS. *Journal of Geophysical Research-Solid Earth and Planets* 92, 599-607 (1987).

Chapter 5 Supplementary information

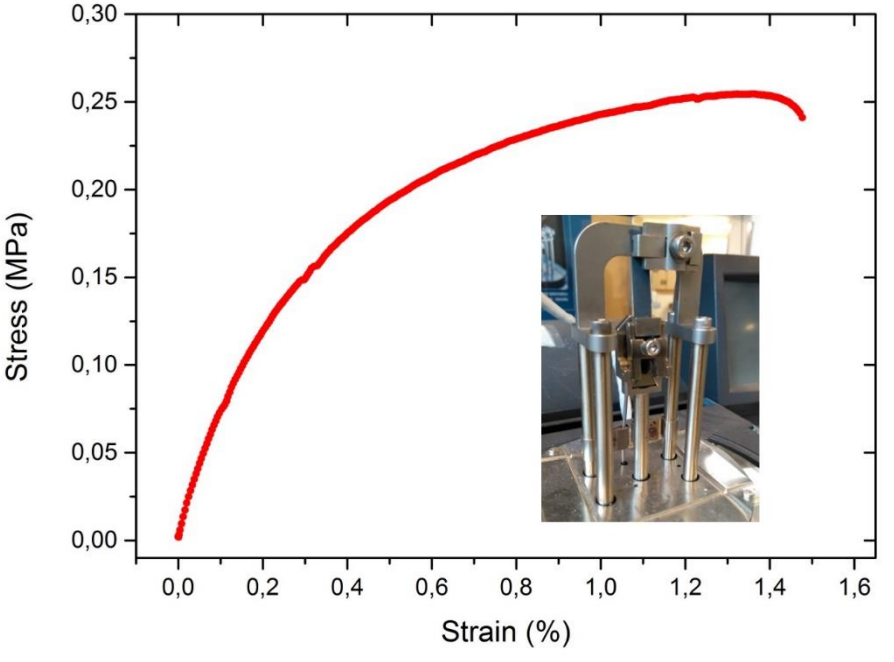

Fig. S5.1 Stress strain curve of a 90% LTO, 5% carbon black and 5% PVDF electrode. The inset shows the self-supporting electrode during tensile testing.

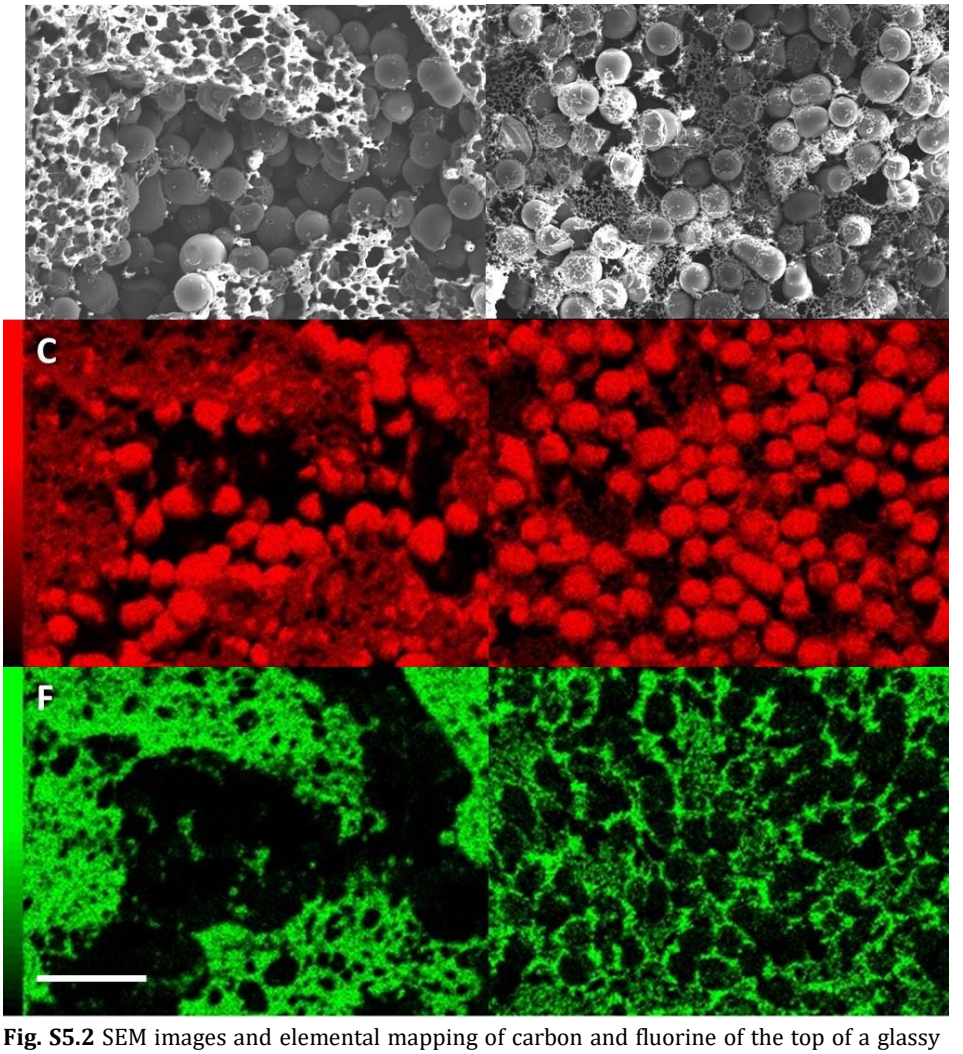

Fig. S5.2 SEM images and elemental mapping of carbon and fluorine of the top of a glassy carbon membrane made by the conventional method (left column), and immersion precipitation (right column). Note the finer PVDF distribution in the F image of the immersion precipitation membrane. The scale bar represents 30 μm.

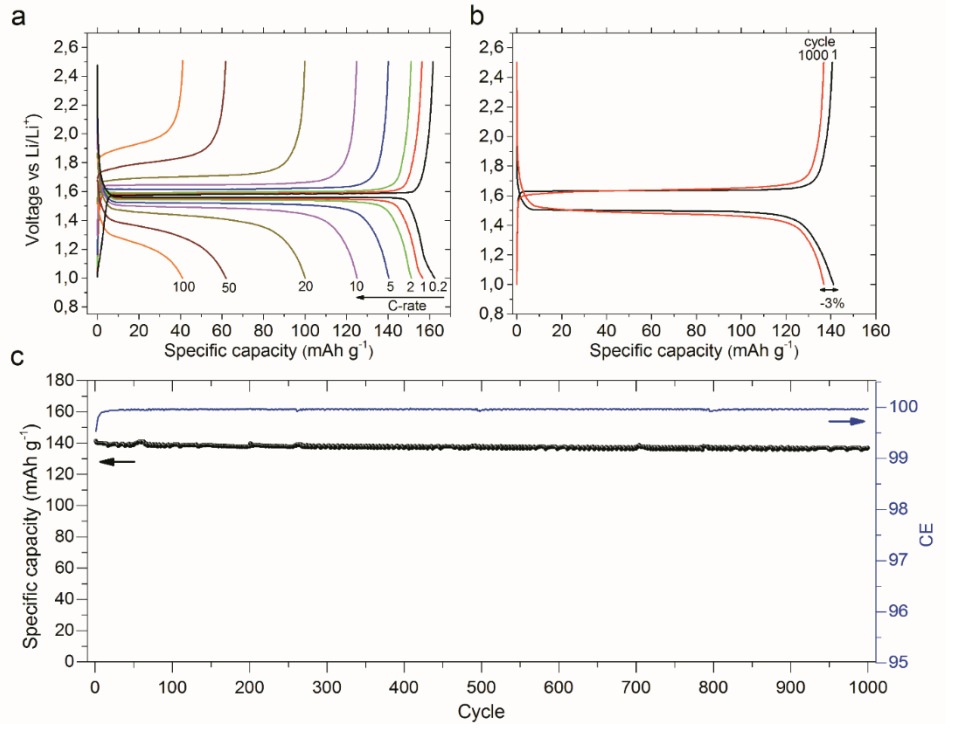

Fig. S5.3 Electrochemical testing of low mass-loading (0.25mAh cm^{-2}) LTO electrodes. a) Voltage profiles and specific capacity for various C-rates, b) long term cycle performance at 5C with the voltage profile of cycle 1 and 1000, and c) the specific capacity and coulombic efficiency as a function of cycle number. (1C = 175 mA g^{-1})

Influence of the Li anode

Fig. S5.4 shows the cycle performance at 1C of a high mass-loading LTO battery. After approximately 120 cycles an obvious decline in performance is observed. After 200 cycles the C-rate was changed to C/5 which results in achieving a much higher capacity. This indicates that the active material was not lost during cycling, but points to a kinetic reason for the capacity decline. To investigate the role of the electrolyte and the Li anode, the cell was opened and the electrolyte was replaced. Cycling the cell at 1C shows similar capacity output as before. However after opening the cell again, this time replacing the Li metal anode, a significant rise in capacity was observed. This clearly shows the enormous influence of the standard reference/counter electrode on the overall performance of the cell; the high mass loading immersion precipitation electrode itself will follow the dotted line.

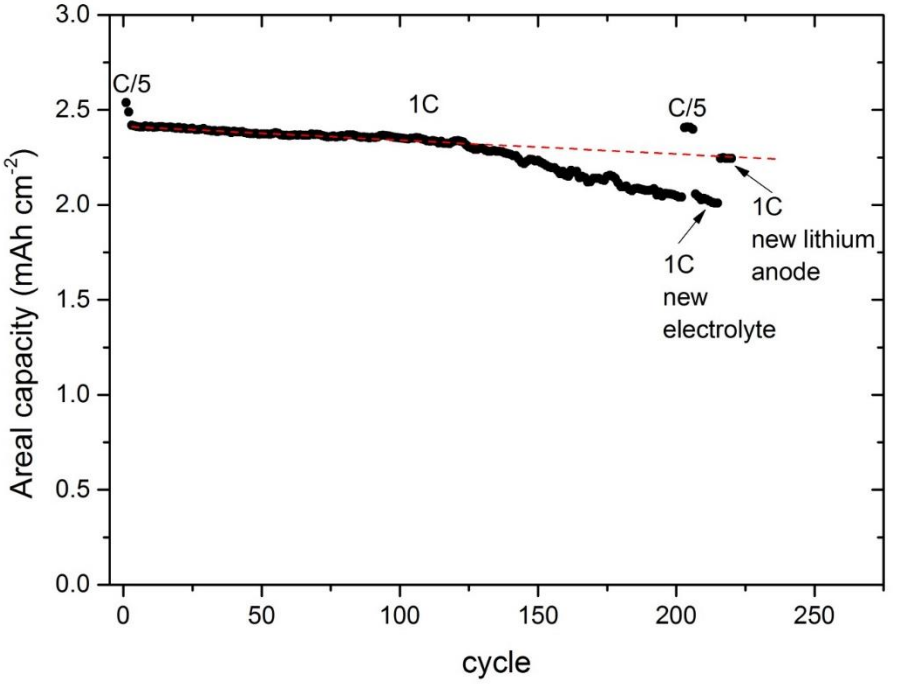

Fig. S5.4 Cycle performance at a rate of 1C of an LTO electrode with a mass-loading of 15 mg cm^{-2}. Note that the high mass loading of the LTO leads to capacity instability problems at the Li metal counter electrode that is applied. This is illustrated by the recovery of the capacity when replacing the Li metal counter electrode.

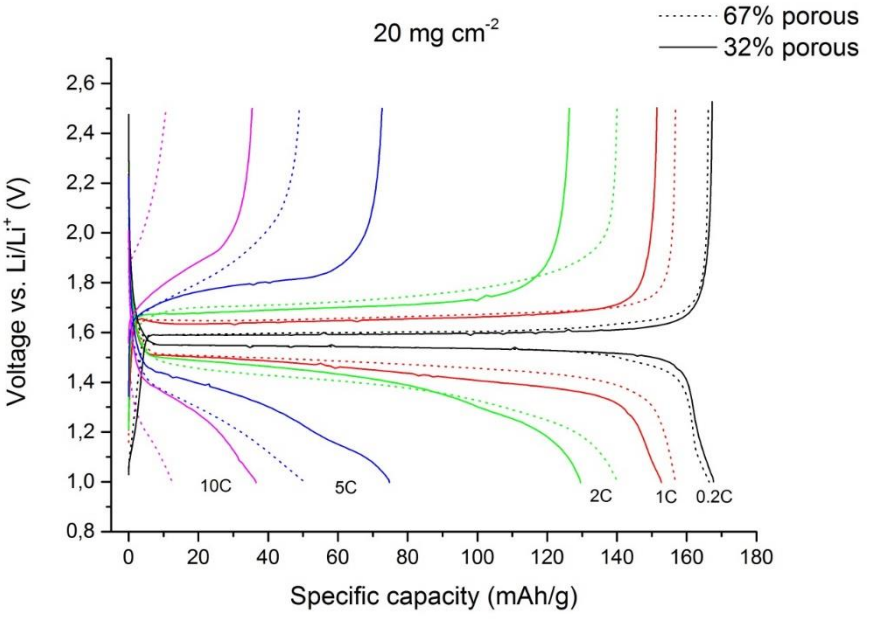

Fig. S5.5 Comparison of the voltage output as a function of specific capacity of a 67% porous LTO electrode (dotted lines) and a 32% porous calendared one, for different C-rates. The (active) mass loading of the electrodes is approximately 20 mg cm^{-2}. (1C = 175 mA g^{-1}). At practical C-rates up to 2C similar behavior is observed while at the highest charge rates the less porous electrode reaches the highest capacities.

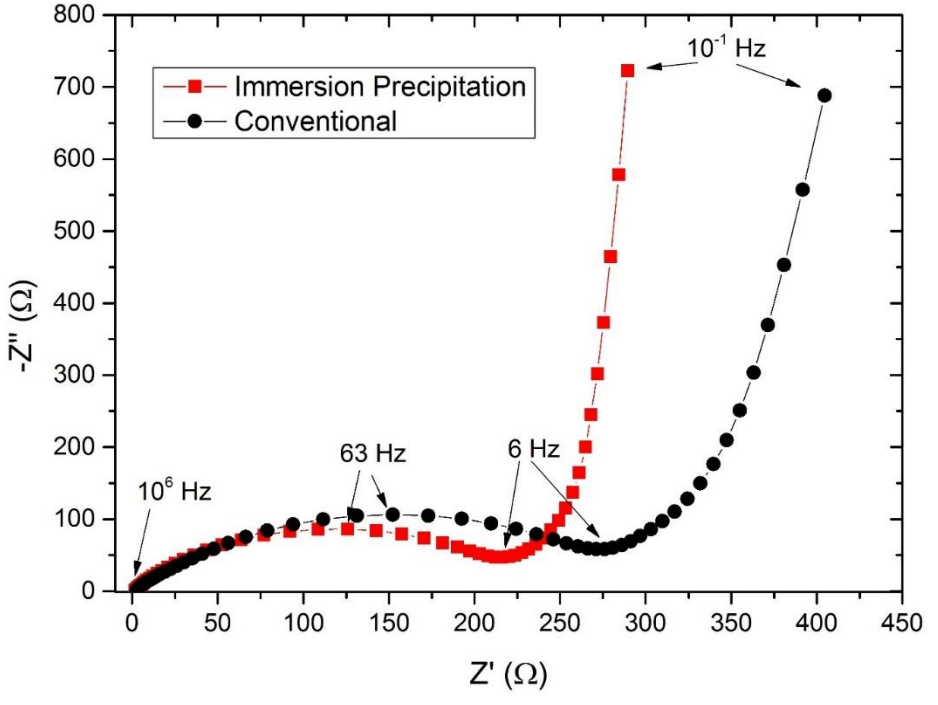

Fig. S5.6 Electrochemical impedance spectroscopy of two LTO electrodes of equal mass loading made by immersion precipitation and conventional drying.

Table S5.1

LTO electrode (method)	Resistance (Ω cm^{-2})
Drying	5.4
Immersion precipitation	3.4

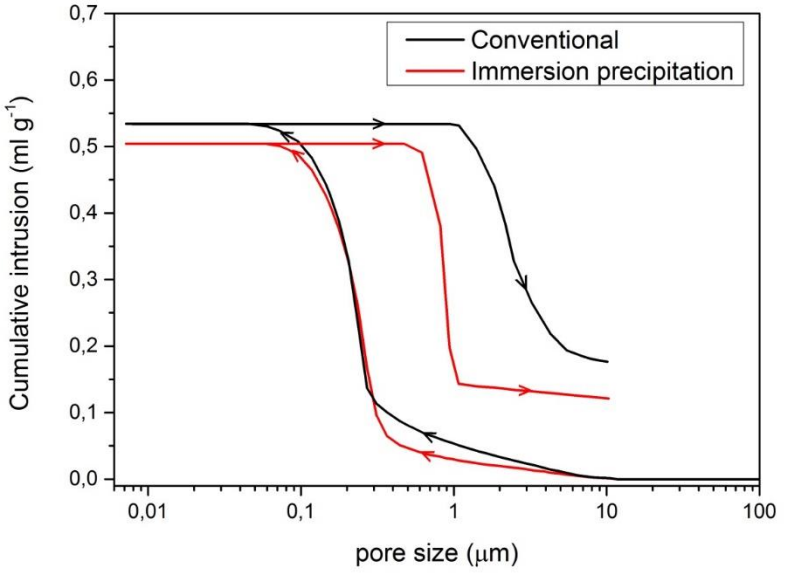

Fig. S5.7 Cumulative mercury in- and extrusion as a function of pore size for an LTO electrode made by both conventional and immersion methods.

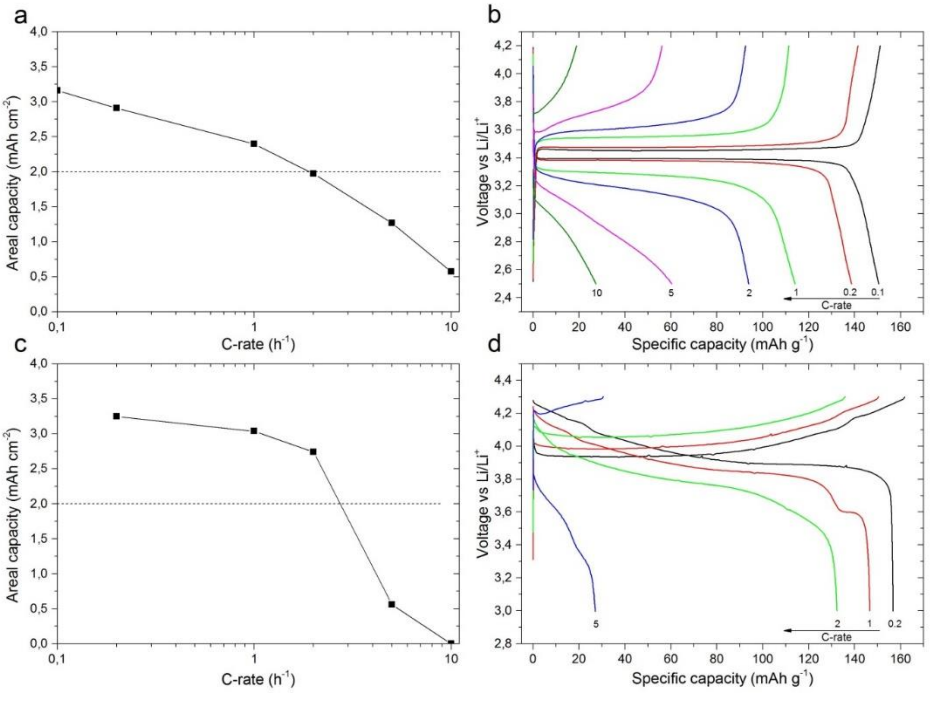

Fig. S5.8 Galvanostatic testing of a 21 mg cm^{-2} LFP (a,b) and LCO (c,d) electrodes with the areal capacity as a function of C-rate and the corresponding voltage profiles as a function of specific capacity. (1C = 160 mA g^{-1})

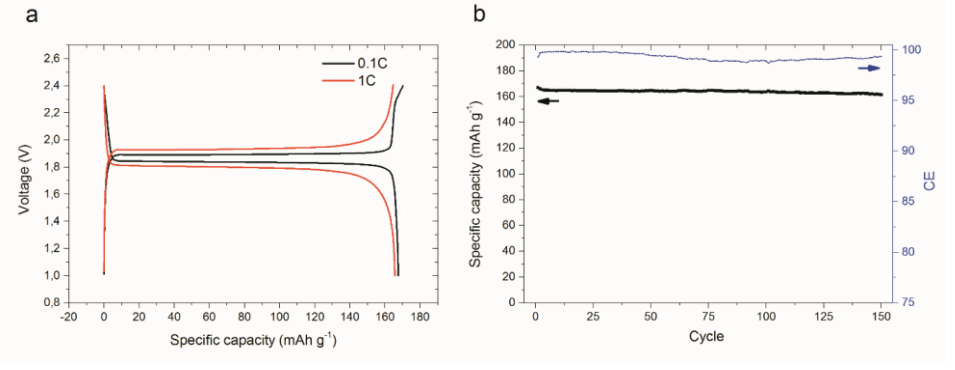

Fig. S5.9 Galvanostatic testing of a LTO-LFP full cell. a) Typical (dis)charge curves at 0.1 (black) and 1C (red) as a function of specific capacity (based on the LTO electrode) and b) cycling performance and coulombic efficiency at 1C. The battery was anode (LTO) limited.

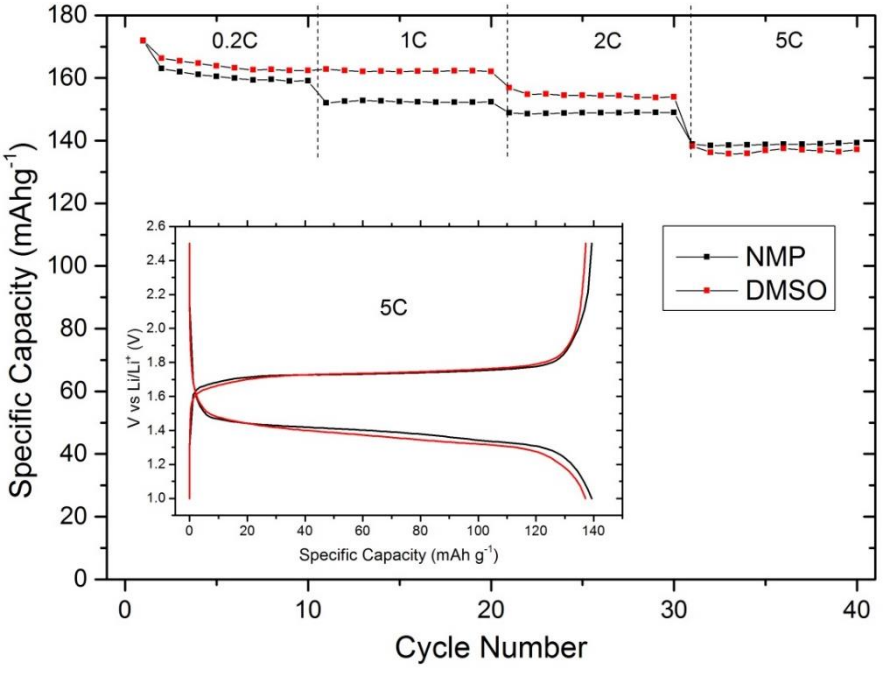

Fig. S5.10 Cycle performance for varying C-rates of 8 mg cm^{-2} LTO electrodes made through immersion precipitation, using a NMP- and DMSO-based slurry. The inset shows the voltage curves as a function of specific capacity, cycling at 5C.

Estimation of heat generation during battery charging

Assuming a charge rate of 2C to 80% of an 80kWh battery and an over-potential of 0.11V at a cell potential of 3.5V the heat losses would amount to 2x0.8x80kWx0.11/3.5 = 4.02 kWh.

Estimation of volumetric/gravimetric energy density increase

For the estimation it was assumed that the battery consists of a double sided electrode coating with a graphite anode and a metal oxide cathode, it does not account for packaging. Furthermore, no adjustments in porosity of the electrode are presumed to balance the possible decline in power density when applying thicker electrodes. The unit cells used for the calculation have equal length (in plane) and are indicated in **Fig. S5.11**, along with the component thicknesses. The density of the components can be found in Table S2.

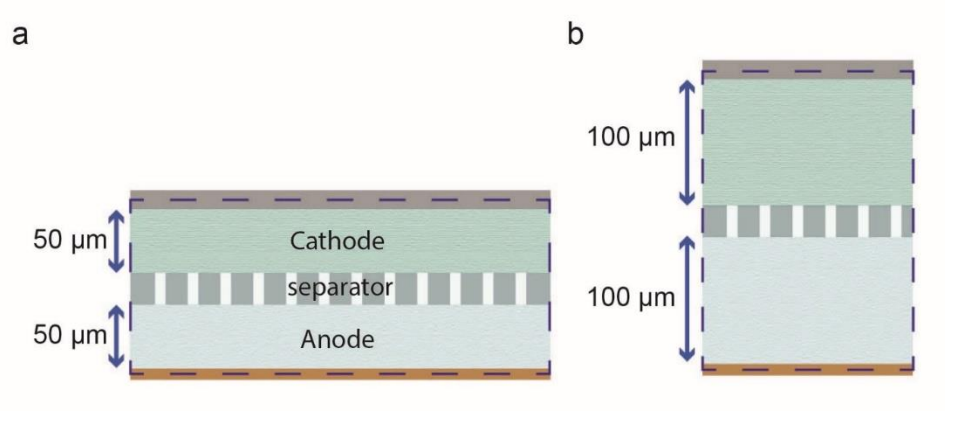

Fig. S5.11 Electrode based on a) thin and b) thick electrodes. The area used for the calculation is indicated by the dashed line. The thickness of the copper foil, separator and aluminum foil is 9, 25, 15 µm, respectively.

Table S5.2

Component	Density ρ (g cm^{-3})
Anode	1.2[a]
Cathode	2.1[a]
Aluminum current collector	2.7
Copper current collector	8.96
Separator	0.55[a]

[a] taken from ref. [1]

The fraction with which the energy density increases volumetrically and gravimetrically respectively, is given by:

$$\frac{V_{thin}}{V_{thick}} - 1 = \frac{2 \cdot (0.5 \cdot d_{copper} + d_{anode\_thin} + d_{sep} + d_{cathode\_thin} + 0.5 \cdot d_{aluminum})}{0.5 \cdot d_{copper} + d_{anode\_thick} + d_{sep} + d_{cathode\_thick} + 0.5 \cdot d_{aluminum}} - 1$$

$$\frac{m_{thin}}{m_{thick}} - 1 = \frac{2 \cdot (0.5 \cdot d_{copper} \cdot \rho_{copper} + d_{anode\_thin} \cdot \rho_{anode} + d_{sep} \cdot \rho_{sep} + d_{cathode\_thin} \cdot \rho_{cathode} + 0.5 \cdot d_{aluminum} \cdot \rho_{aluminum})}{0.5 \cdot d_{copper} \cdot \rho_{copper} + d_{anode\_thick} \cdot \rho_{anode} + d_{sep} \cdot \rho_{sep} + d_{cathode\_thick} \cdot \rho_{cathode} + 0.5 \cdot d_{aluminum} \cdot \rho_{aluminum}} - 1$$

With the component thickness *d* and density *ρ*.

References

[1] D. L. Wood, III, J. Li and C. Daniel, Journal of Power Sources, 2015, 275, 234-242.

Summary

Due to the electricity storage facilities required for a future powered on renewable energy, and due to the high performance batteries necessary for electric vehicles and mobile electronics, battery research and development is more urgent than ever. In this thesis battery technology was investigated both on the material-, as on the electrode-level. This research was carried out to elucidate working principles of new battery materials and to develop new fabrication methods as to contribute to improving Li-ion batteries.

Lithium-sulfur batteries are considered a promising new battery technology, receiving significant research attention. Sulfur is low in cost, benign and abundant, and in its reaction with lithium can store a lot of energy. However, it is an electronic insulator. Moderate to high electronic conductivity is seen as a prerequisite for electrode materials. This bears the question why the lithium-sulfur can deliver a relatively high power. Chapter 2 studies the apparent discrepancy between its low electronic conductivity and relatively high performance, which had not been addressed in scientific studies previously. Simple in design, but very effective experiments were conducted that give decisive answers on the matter. In the cells that are tested the active material (sulfur) is physically (and electronically) separated from the electrode/current collector. The cells performed as usual, proving that the lithiation mechanism of sulfur involves sulfur as a molecular dissolved species, and provides a reason why the incredibly poor conductivity of sulfur doesn't play a big role; reactions take place on a molecular level, without solid state conduction of electrons. In simpler words; the active material finds its way to the electrode/electrons, where normally the electrons diffuse through the (bulk) active material.

In situ study of batteries forms an essential part of battery research. It is done without disassembling the cell and can also be conducted on a working cell (operando). This as opposed to post-mortem research, where the battery is affected and non-functional at the time of measurement. However, in order to conduct in situ measurements, the cell should be compatible with the method, which in most cases means the standard cell needs to be modified. In chapter 3 a comprehensive overview of in situ techniques and cell designs is given, with a focus on recent results and developments. Technique limitations and the impact of the cell adjustments are critically discussed. From the overview it is apparent that many in situ methods have similar requirements with respect to cell design, which allows to apply different in situ techniques in series to obtain more information. The most notable recent development is the rise of in situ transmission electron microscopy, which opens up a new area of investigating batteries on a nanoscale (during use).

However, the obtained results, valuable as they are, should be critically interpreted due to the special requirement imposed by the electron microscope, which only allows the use of vacuum proof nano-batteries,

The accumulated knowledge on lithium-sulfur technology and operando measurements is combined in chapter 4. Neutron depth profiling was chosen based on its ability to measure the lithium concentration in both the electrode and the electrolyte, which is a major advantage for a system where the active material is not confined to the electrode area only. The measurements obtained during battery discharge directly showed the polysulfide diffusion in and out of the electrode and polysulfide adsorption on metal oxide particles within the battery. The observation experimentally confirmed the current theory on the lithiation mechanism of lithium-sulfur cells and gave direct evidence behind the optimization techniques currently employed based on chemical adsorption of active material.

In the chapter 5 a different approach was taken to increase the energy density of batteries. Instead of having a focus on electrode materials, it concentrates on electrode manufacturing process; a kind of electrochemical engineering. The energy density on cell level can be increased by increasing the electrode thickness, as this increases the ratio of active and inactive materials in the battery, The thickness is currently limited by the mechanical integrity of the electrode, as well as the limited through-electrode ionic conductivity. To this end a method was presented based on a process called polymer phase inversion. It relies on mature polymer membrane technology and is very similar to the current wet processing techniques. However, the small adaptation of the conventional method by using a non-solvent to solidify the polymer binder, instead of drying, has large positive effects in terms of electrode flexibility and electrochemical performance. The good performance of the thick electrodes was shown to be an effect of the highly interconnected porosity, improving the ionic conductivity in the electrode, and the homogenous distribution of the polymer binder, which gives the electrodes their flexibility but also increases the electronic conductivity due to the enhanced physical contact of electrode material throughout the layer.

Samenvatting

Door de benodigde energie opslag faciliteiten voor een toekomst gebaseerd op duurzame energie, en door de hoogwaardige batterijen die nodig zijn voor elektrische voertuigen en mobiele elektronica, is batterij-onderzoek en -ontwikkeling urgenter dan ooit. In dit proefschrift wordt batterij technologie onderzocht, zowel op materiaal- als op electrode-niveau. Dit onderzoek is gedaan om inzicht te krijgen in de werking van nieuwe batterij materialen en het ontwikkelen van nieuwe fabricatie methoden om daarmee bij te dragen aan de verbetering van Li-ion batterijen.

Lithium-zwavel batterijen worden beschouwd als een veelbelovende nieuwe batterij-technologie en ontvangen veel aandacht van onderzoekers. Zwavel is goedkoop, goedaardig en overvloedig op aarde aanwezig en kan in reactie met lithium veel energie opslaan. Het is echter een elektronische isolator. Matige tot hoge elektronische geleiding wordt gezien als een vereiste voor elektrodematerialen. Dit roept de vraag op waarom de lithium-zwavel batterij een relatief hoog vermogen kan leveren. In hoofdstuk 2 wordt de schijnbare discrepantie tussen de lage elektronische geleiding en relatief hoge prestaties bestudeerd, iets dat nog niet in eerdere wetenschappelijke studies was gedaan. Eenvoudig in ontwerp, maar zeer effectieve experimenten zijn uitgevoerd die duidelijke antwoorden over de kwestie geven. In de cellen die zijn getest, werd het actieve materiaal (zwavel) fysiek (en elektronisch) gescheiden van de elektrode/stroomcollector. De cellen werkten zoals gewoonlijk, waaruit blijkt dat het bij het lithiëring mechanisme van zwavel, zwavel als opgelost molecuul deelneemt, dit geeft een reden waarom de ongelooflijk slechte geleiding van zwavel geen grote rol speelt; reacties vinden plaats op moleculair niveau, zonder elektron geleiding door de vaste stof. In eenvoudigere woorden; het actieve materiaal vindt zijn weg naar de elektrode/elektronen, waar normaal de elektronen diffunderen door het actieve materiaal.

In situ onderzoek van batterijen vormt een essentieel onderdeel van batterijonderzoek. Het wordt gedaan zonder de cel te demonteren en kan ook worden uitgevoerd op een werkende cel (operando). Dit in tegenstelling tot post-mortem onderzoek, waarbij de batterij wordt aangetast en niet functioneert op het moment van meten. Om in situ metingen uit te voeren, moet de cel echter compatibel zijn met de methode, wat in de meeste gevallen betekent dat de standaardcel moet worden aangepast. In hoofdstuk 3 wordt een uitgebreid overzicht gegeven van in situ technieken en cel-ontwerpen, met de focus op recente resultaten en ontwikkelingen. De beperkingen die de technieken hebben en de impact van de cel aanpassingen worden kritisch besproken. Uit het overzicht blijkt

dat veel in situ methoden vergelijkbare eisen stellen aan het cel-ontwerp, waardoor verschillende technieken in serie kunnen worden toegepast om meer informatie te verkrijgen. De meest opvallende recente ontwikkeling is de opkomst van in situ transmissie elektronen-microscopie, wat een nieuw onderzoeksgebied opent voor het onderzoeken van (werkende) batterijen op nanoschaal. De verkregen resultaten, hoe waardevol ze ook zijn, moeten echter kritisch worden geïnterpreteerd vanwege de speciale eisen bij het toepassen van een elektronenmicroscoop, die alleen het gebruik van vacuümbestendige nanobatterijen toestaat.

De opgebouwde kennis over lithium-zwavel technologie en operando-metingen is gecombineerd in hoofdstuk 4. Neutronen diepte-profilering is gekozen op basis van het vermogen om de lithiumconcentratie in zowel de elektrode als de elektrolyt te meten, wat een groot voordeel is voor een systeem waarbij de actieve materiaal zich niet alleen beperkt tot het elektrodegebied. De metingen tijdens batterij-ontlading lieten expliciet de polysulfide-diffusie in en uit de elektrode zien, en de polysulfide adsorptie op metaaloxidedeeltjes in de batterij. De observatie bevestigde experimenteel de huidige theorie over het lithiërings mechanisme van lithium-zwavel cellen en gaf direct bewijs voor de tegenwoordig toegepaste optimalisatie-technieken op basis van chemische adsorptie van actief materiaal.

In hoofdstuk 5 is een andere benadering gekozen om de energiedichtheid van batterijen te verhogen. In plaats van het concentreren op elektrodematerialen, richt het onderzoek zich op het productieproces van elektroden; een soort elektrochemische engineering. De energiedichtheid op cel-niveau kan worden verhoogd door de elektrode-dikte te vergroten, omdat dit de verhouding van actieve en inactieve materialen in de batterij verhoogt. De dikte wordt momenteel beperkt door de mechanische integriteit van de elektrode, evenals de beperkte ionische geleiding door de elektrode. Daarom werd een methode gepresenteerd op basis van een proces dat polymeer fase-inversie wordt genoemd. Het gebruikt ver ontwikkelde polymeer-membraan technologie en is zeer vergelijkbaar met de huidige natte verwerkingstechnieken. De kleine aanpassing op de conventionele methode door het gebruik van een anti-oplosmiddel om het polymeer bindmiddel te laten stollen, in plaats van drogen, heeft echter grote positieve effecten op het gebied van elektrode flexibiliteit en elektrochemische prestaties. De goede prestaties van de dikke elektroden bleken een effect te zijn van de sterk onderling verbonden porositeit, dat de ionische geleiding in de elektrode verbetert, en de homogene verdeling van het polymere bindmiddel, dat de elektroden hun flexibiliteit geeft maar ook de elektronische geleidbaarheid verhoogt vanwege het verbeterde fysieke contact van het elektrodemateriaal door de gehele laag.

Dankwoord

Because of the great people, the nice environment and the fun group activities, the past years working at the TU Delft have been marvelous. The ski trip to France and the conference in Kyoto I will never forget. I want to thank everyone of the batterygroup, no need to sum up names, we know who we are..

However I would like to address several people personally. Thank you Yaolin for always helping and assisting others, including me, whether you were busy yourself or not. Chandra your contributions to my manuscripts are invaluable. Your enthusiasm for our work is inspiring, good luck with your battery solarcell hybrid, you will need it. Thank you Viola for offering me a place to stay in Delft after I moved to Utrecht, and hanging out with me and Carla after work so much. I love sports so it was great to have the pingpong crew; Thang, Chandra and Alexandros, and my tennis partners Martijn and Michi. Michi, you are the adopted son of the batterygroup, however we will never let you become an official member, you and I will stay in touch though.

Ik ben ooit begonnen in Eindhoven omdat jij, Peter, mij daar de PhD plek gunde, dit heeft me de batterijwereld ingestuurd, dank daarvoor, net als voor je bijdrage aan de papers. In Delft is echt een batterij groep ontstaan, wat vooral aan jou, Marnix, te danken is, bedankt voor het 'toestaan' van de ski reis, de uitjes en bbq's. Frans, jij bent altijd vrolijk en jouw praktische en theoretische batterij kennis is van onschatbare waarde voor de groep, dank voor al je hulp. Niek het was fijn om naast je te zitten en leuk dat ik je bruiloft heb mogen meemaken. Fijn, Remco, dat je me geregeld in beschonken toestand afzette bij een station en dat ik, via je vrouw, de Surinaamse keuken heb leren kennen. Het voelt alweer als heel lang geleden, Carla, dat jij mijn collega was, gelukkig zien we elkaar nog vaak en ik hoop dat je nog lang in Nederland blijft. Tomas ik wil jou bedanken voor je inzet voor de groep en het erdoorheen trekken van ons NDP paper toen ik de wetenschappelijke wereld al een beetje achter me had gelaten. Fokko, dank je voor je uitstekende begeleiding, het altijd willen meedenken en voor de vrijheid je me gaf, wat heeft geleid tot deze thesis met een breed scala aan onderwerpen.

Curriculum Vitae

Peter-Paul Harks was born 19 april 1984 in Leiderdorp, The Netherlands. He studied physics at the Utrecht University, where he graduated in 2012. During his master he studied the synthesis of metal(oxide) nanostructures.

In 2012 Peter-Paul got a PhD position on solid state micro-batteries at the Eindhoven University of Technology, under the supervision of Prof. P.H.L. Notten. In 2014 he transitioned to the Delft University of Technology to start a new PhD project supervised by Prof. Fokko M. Mulder. In the Materials for Energy Conversion and Storage group he investigated high energy-density materials for Li-ion batteries. More than 4 years of research resulted in several peer reviewed articles and the thesis 'Characterization and development of high energy density Li-ion batteries'.

List of publications

Related to his thesis:

PPRML Harks, FM Mulder, PHL Notten, *In situ methods for Li-ion battery research: A review of recent developments*, Journal of power sources 288, 92-105 (2015)

PPRML Harks, CB Robledo, TW Verhallen, PHL Notten, FM Mulder, *The significance of elemental sulfur dissolution in liquid electrolyte lithium sulfur batteries*, Advanced Energy Materials 7 (3), 1601635 (2017)

PPRML Harks, TW Verhallen, C George, JK van den Biesen, Q Liu, M Wagemaker FM Mulder, *Spatio-temporal Quantification of lithium both in Electrode and in Electrolyte with atomic precision via Operando Neutron Absorption*, Journal American Chemical Society 141 (36), 14280-14287 (2019)

PPRML Harks, CB. Robledo, C George, C Wang, T van Dijk, L Sturkenboom, HDW Roesink, FM Mulder, *Immersion Precipitation Route Towards High Performance Thick and Flexible Electrodes For Li-ion Batteries*, Journal of Power Sources, 10. 1016/j.jpowsour.2019.227200

Not related to this thesis:

J Xie, JFM Oudenhoven, **PPRML Harks**, D Li, PHL Notten, *Chemical vapor deposition of lithium phosphate thin-films for 3D all-solid-state Li-ion batteries*, Journal of the Electrochemical Society 162 (3), A249-A254 (2015)

J Xie, **PPRML Harks**, D Li, LHJ Raijmakers, PHL Notten, *Planar and 3D deposition of Li4Ti5O12 thin film electrodes by MOCVD*, Solid State Ionics 287, 83-88 (2016)

Y Xu, E Swaans, S Chen, S Basak, **PPRML Harks**, B Peng, HW Zandbergen, DM Borsa, FM Mulder , *A high-performance Li-ion anode from direct deposition of Si nanoparticles*, Nano Energy 38, 477-485 (2017)

C Chen, D Li, L Gao, **PPRML Harks**, RA Eichel, PHL Notten, *Carbon-coated core–shell Li_2S@C nanocomposites as high performance cathode materials for lithium–sulfur batteries*, Journal of Materials Chemistry A 5 (4), 1428-1433 (2017)

Y Xu, AS Menon, **PPRML** Harks, DC Hermes, LA Haverkate, S Unnikrishnan, FM Mulder, *Honeycomb-like porous 3D nickel electrodeposition for stable Li and Na metal anodes*, Energy Storage Materials 12, 69-78 (2018)

A Vasileiadis, NJJ de Klerk, RB Smith, S Ganapathy, **PPRML Harks**, MZ Bazant, M Wagemaker, *Toward Optimal Performance and In-Depth Understanding of Spinel $Li_4Ti_5O_{12}$ Electrodes through Phase Field Modeling*, Advanced Functional Materials 28 (16), 1705992 (2018)

MC Paulus, MF Graf, **PPRML Harks**, A Paulus, PPM Schleker, PHL Notten, RA Eichel, J Granwehr, *Investigation of the Li-ion conduction behavior in the $Li_{10}GeP_2S_{12}$ solid electrolyte by two-dimensional T1-spin alignment echo correlation NMR*, Journal of Magnetic Resonance 294, 133-142 (2018)